Transient Behavior of Granular Material

Thesis by
Han-Hsin Lin

In Partial Fulfillment of the Requirements for the
Degree of
Doctor of Philosophy

CALIFORNIA INSTITUTE OF TECHNOLOGY
Pasadena, California

2023
Defended Defended March 15, 2023

Han-Hsin Lin
ORCID: 0009-0003-8640-470X

ACKNOWLEDGEMENTS

I would like to express my profound gratitude to my Ph.D. advisor, Melany Hunt, whose invaluable guidance and mentorship have been instrumental in shaping my Ph.D. journey. Melany's unwavering support, academic expertise, and perceptive feedback have been essential in refining my research ideas and methodologies. I am incredibly grateful to have an advisor who provided not only academic, research, and career advice but also generously shared credit, promoted my work, and offered encouragement. Whenever I needed counsel or suggestions, Melany was always willing to discuss and guide me with her rigorous approach to academia. Her dedication to excellence and steadfast commitment to her students have been genuinely inspiring. I consider myself exceedingly fortunate to have Melany as my advisor and mentor, and her exemplary leadership will continue to guide me in my future endeavors.

I am also immensely grateful to my thesis committee members, Professor John Brady, Professor Xiaojing Fu, and Professor Kenneth Libbrecht, for their constructive feedback, invaluable suggestions, and dedication to my academic progress. Their collective wisdom has significantly contributed to the development and completion of this research. I am especially grateful to Professor John Brady for allowing me to use his rheometer to conduct experiments, which would not have been possible without his help.

My heartfelt appreciation goes to my colleagues and group members at Caltech, who provided intellectual stimulation, camaraderie, and much-needed levity during this journey. Special thanks to Yichuan Song for his presentation suggestions. I also thank the undergraduate students, Ernst Olivia, Ellen Chuan, and Arthur Young, with whom I worked previously. Additionally, I would like to extend my gratitude to the many MCE staff members who assisted me during my Ph.D. study, including our research group assistants, formerly Holly Golcher and currently Mikaela Laite, and the MCE department administrator, Lynn Seymour.

I acknowledge the financial support provided by the National Science Foundation under Grant No. 1706166, which has been crucial in facilitating my research endeavors.

I would like to extend my gratitude to my friends for their unwavering friendship and support. Their camaraderie and laughter have been invaluable during some of the most challenging times of my Ph.D. journey, and I cherish the memories of the time spent with them. Please forgive me for not listing all the names here, as there are simply too many to mention individually.

My most thanks go to my parents and sisters for their understanding and unconditional support throughout my life.

Finally, I extend my appreciation to all individuals and organizations that have directly or indirectly contributed to the success of this research. Your support has made this accomplishment possible.

ABSTRACT

This PhD thesis focuses on the flows on granular materials, such as sand, glass beads, and powders, which are sheared at low speeds with gravity perpendicular to the flow direction. The study is conducted using a combination of experiments, simulations, and theory, with the goal of developing a unifying theory of granular materials that can be described by continuum models. The main objective is to understand how microscale physics propagate to macroscale phenomena and to address issues related to setting boundary conditions and predicting timescales from unsteady to steady states. This research primarily aims to investigate stress variations in granular materials as a function of shear rate, encompassing both steady and unsteady states. Additionally, the thesis examines the phenomena of wall force anomalies and vortex flows. In Couette cell experiments and vertical plane shear simulations, granular material demonstrates a downward flow near the vertical shearing wall and an upward flow adjacent to another static vertical wall. Interestingly, this vortex flow causes a change in the direction of vertical shear stress when wall shearing commences, contradicting the prevalent assumption that particles consistently apply a downward force on the vertical wall.

The study concludes with key findings, including the observation that normal and shear stresses on the shearing wall increase slowly after the initiation of shearing, and that steady-state values for these stresses are independent of the shearing speed within a certain range. The study also found that the height of particles near the shearing wall decreases gradually with the presence of vortex flow, and that the shear rate near the moving wall is initially high and decreases slowly to reach a steady state. Additionally, we used a non-local constitutive model and Boussinesq approximation to predict the downward flow that is driven by gravity and variations in the solid fraction near the shearing surface, as well as the decay profile of velocity in an infinitely wide box for the steady state.

Overall, this thesis contributes to our understanding of granular materials in the

slow flow regime, providing insights into their behavior under shear. The non-local model accurately predicts the downward flow and velocity decay profile, indicating its potential as a valuable tool for future research.

TABLE OF CONTENTS

Acknowledgements . . . iii
Abstract . . . v
Table of Contents . . . vii
List of Illustrations . . . ix
List of Tables . . . xiv
Chapter I: Introduction . . . 1
1.1 Background and motivation . . . 2
1.2 Constitutive model . . . 2
1.3 Transient/unsteady flow . . . 7
1.4 Anisotropy, wall force anomaly, vortex flow . . . 7
1.5 Discrete element modeling . . . 8
1.6 Objective . . . 8
Chapter II: Experimental . . . 13
2.1 Experimental background . . . 14
2.2 Setup . . . 14
2.3 Torque control . . . 16
2.4 Steady time . . . 16
2.5 Non-monotonic relation of stress-velocity . . . 17
2.6 Vortex . . . 17
2.7 Conclusions . . . 18
Chapter III: Simulation Preparation . . . 29
3.1 Setup . . . 30
3.2 Simulation Time Step and Comparison of different sample frequencies of variables output . . . 34
3.3 Comparison of Hertz and Hooke Model . . . 35
Chapter IV: Simulation Result . . . 38
4.1 Introduction . . . 39
4.2 Transient Velocity and Solid Fraction . . . 39
4.3 Vortex flow . . . 39
4.4 Wall stress anomaly . . . 40
4.5 μ-I . . . 41
4.6 Initial transition vs later time . . . 42
4.7 Results of different wall velocity . . . 43
4.8 Results of different box sizes . . . 43
4.9 Conclusions . . . 44
Chapter V: Theoretical Model . . . 73
5.1 Theoretical Model . . . 74
Chapter VI: Conclusion and Future Outlook . . . 86
6.1 Conclusion . . . 87

6.2 Compare to other models 88
6.3 Future direction 88

LIST OF ILLUSTRATIONS

Number *Page*

1.1 The steel beads flow down on a slope show different phases of granular material appear at the same time. (Forterre and Pouliquen, 2008) . . 11

1.2 Illustration of the typical deformation time scale, T_γ, and the confinement time scale, T_p, depicting their physical significance. (MiDi, 2004) 12

1.3 Two-dimensional plane shear simulation: (a) quasistatic regime ($I = 10^{-2}$); (b) collisional regime ($I = 0.2$). Black grains constitute the rough walls. The linewidths are proportional to the intensity of the normal force between grains. (Cruz et al., 2005) 12

2.1 The rheometer used in the experiments 19

2.2 Different types of rotating bobs. 20

2.3 The rotating bob and the container. 20

2.4 Size of the bob and the container. 21

2.5 Memory elimination using an upward flow of air with glass beads diameter $d = 25\mu m$. Rough cylinder. Shear rate is 5.8/s. $D = 2.6cm$. $h = 1.0cm$. The normalized stress is $\tau/r_i A$, where τ is the torque and A is the area of the side wall that contact with particles. 21

2.6 Constant torque experiments. Rotation stops for torques below the critical value. Rough bob. 25 μm glass bead. 22

2.7 Experiments using a blade to shear the glass beads with different constant torque. (preparation by using constant shear rate $50s^{-1}$ during 10 s, no rest) from Da Cruz et al. (2002) 22

2.8 Transition of wall stress in different rotational speeds for the rough cylinder. $h = 2.0cm$, $D + L = 3.8cm$. $25\mu m$ glass bead. For a rotation speed of 1 rev/s, the corresponding inertia number and shear rate are $I = 8.8 \times 10^{-4}$ and $\dot{\gamma} = 8.2/s$. 23
2.9 Transition of wall stress in different rotational speeds for the smooth cylinder. $h = 2.0cm$, $D + L = 3.9cm$. $25\mu m$ glass bead. 24
2.10 Transition time of wall stress is longer for the smooth cylinder than the rough cylinder. The data are from figs. 2.8 and 2.9 for 0.01 rev/s. 24
2.11 Kamala Jyotsna Gutam, Vishwajeet Mehandia, and Prabhu R. Nott (2013) 25
2.12 Non-monotonic stress-speed relation. The depth is $D + L$, and the particles are $25\mu m$. 26
2.13 Using smooth bob. $100\mu m$ glass bead. $h = 1.0cm$, $D + L = 4.25cm$. 26
2.14 Using smooth bob. $100\mu m$ glass bead. $h = 2.0cm$, $D + L = 3.0cm$. 27
2.15 Surface flow. The velocity of particles in the red frame in (a) is slow enough to use the visualization method to calculate the velocity field by comparing snapshots of the recording video. The average value of radial velocity in the red frame on the top surface $V_r r/r_i \approx 5.6 \times 10^{-4} \times V_{wall}$ 28
3.1 image when shearing 36
3.2 Normal force on shearing plane for Hooke and Hertz Model 37
4.1 Depth-averaged of azimuthal velocity at different strain 44
4.2 Surface velocity in steady state ($\gamma = 7.376$) in both linear and log (inset) scale 45
4.3 Solid fraction at $\gamma = 0$ 45
4.4 Solid fraction at steady state ($\gamma = 7.38$) 46
4.5 Solid fraction averaged from bottom to 22 d_p height 46
4.6 Vortex flow when $\gamma = 0.246$ (a), 2.46 (b), 7.38 (c). The magnitude of velocity is scaled by the wall velocity. 47

4.7 Free surface when $\gamma = 0$ (a), 0.98 (b), 14.75 (c). The color-coded dots in the figure represent density, with navy blue indicating the lowest values and light yellow indicating the highest. 48
4.8 Surface velocity toward the shearing wall at the top of the bed at different values of γ. The magnitude of velocity is scaled by the wall velocity. 49
4.9 Velocity toward the shearing wall at the height 3 d_p under the surface at different values of γ. The magnitude of velocity is scaled by the wall velocity. 49
4.10 The velocities in the normal and vertical directions as a function of y at different heights for $\gamma = 0.98$. 50
4.11 Wall stresses σ_{yy} (a), and σ_{yz} (b) on the shearing wall. $H = 60d_p$ . . 51
4.12 Wall stresses σ_{yy} (a), and σ_{yz} (b) on the static wall. $H = 60d_p$ 52
4.13 Inertia number in steady state at different locations for $\gamma = 15.98$ . . . 53
4.14 Inertia Number average over a large region in the middle of the box . 53
4.15 Stress ratio average over a large region in the middle of the box 54
4.16 μ-I at different location. Each color represents the data in the same height z for different values of y from $2d_p$ to $12d_p$. Blue dots are height $z = 1.5d_p$. Orange dots are height $z = 7.5d_p$. Green dots are height $z = 13.5d_p$. Red dots are height $z = 19.5d_p$. Purple dots are height $z = 25.5d_p$. Brown dots are height $z = 31.5d_p$. Pink dots are height $z = 37.5d_p$. Grey dots are height $z = 43.5d_p$. 54
4.17 Inertia Number near the shearing wall 55
4.18 Stress ratio near the shearing wall 55
4.19 Inertia Number in the middle of the box 56
4.20 Stress ratio in the middle of the box 56
4.21 Inertia Number near the static wall 57
4.22 Stress ratio near the static wall 57
4.23 σ_{11}/P at middle of the box. 58
4.24 σ_{22}/P at middle of the box. 58

4.25 σ_{33}/P at middle of the box. 59
4.26 Shearing wall stress for $Sa = 2 \times 10^{-5}$ 59
4.27 Shearing wall stress for $Sa = 2 \times 10^{-6}$ 60
4.28 Shearing wall stress for $Sa = 2 \times 10^{-7}$ 60
4.29 Shearing wall stress for $Sa = 2 \times 10^{-6}$ with double width. 61
4.30 Average velocity at different strain for $Sa = 2 \times 10^{-5}$ 61
4.31 Average velocity at different strain for $Sa = 2 \times 10^{-6}$ 62
4.32 Average velocity at different strain for $Sa = 2 \times 10^{-7}$ 62
4.33 Average velocity at different strain for $Sa = 2 \times 10^{-6}$ for double width box. 63
4.34 Average velocity at different strain for $Sa = 2 \times 10^{-5}$ 63
4.35 Average velocity at different strain for $Sa = 2 \times 10^{-6}$ 64
4.36 Average velocity at different strain for $Sa = 2 \times 10^{-7}$ 64
4.37 Velocity averaged over full depth of the bed at different strain for $H = 30d_p$ 65
4.38 Velocity averaged over full depth of the bed at different strain for $H = 60d_p$ 65
4.39 Velocity averaged over full depth of the bed at different strain for $H = 90d_p$ 66
4.40 Velocity averaged over full depth of the bed at different strain for $H = 120d_p$ 66
4.41 Shearing wall stress for $H = 30d_p$ 67
4.42 Shearing wall stress for $H = 60d_p$ 67
4.43 Shearing wall stress for $H = 90d_p$ 68
4.44 Shearing wall stress for $H = 120d_p$ 68
4.45 Shearing wall stress ratio for $H = 30d_p$ 69
4.46 Shearing wall stress ratio for $H = 60d_p$ 69
4.47 Shearing wall stress ratio for $H = 90d_p$ 70
4.48 Shearing wall stress ratio for $H = 120d_p$ 70
4.49 Static wall stress ratio for $H = 30d_p$ 71

4.50 Static wall stress ratio for $H = 60d_p$ 71
4.51 Static wall stress ratio for $H = 90d_p$ 72
4.52 Static wall stress ratio for $H = 120d_p$ 72
5.1 Vertical velocity u_z for two different values of p_c. 81
5.2 Vertical velocity u_z as the term $l^2\Pi\partial_{yyy}u_x$ is included for $l = 10d_p$ and $p_c = 0.7 \times 17\rho_p g d_p$ 82
5.3 Vertical velocity u_z as the term $l^2\Pi\partial_{yyy}u_x$ is included for $l = 1d_p$ and $p_c = 0.7 \times 17\rho_p g d_p$ 82
5.4 Vertical velocity u_z as the term $l^2\Pi\partial_{yyy}u_x$ is included for $l = 10d_p$, $\frac{du_z(0)}{dy} = -0.1u_z(0)/d_p$ and $p_c = 0.7 \times 17\rho_p g d_p$ 83
5.5 Vertical velocity in simulation for box size $50d_p \times 16d_p \times 120d_p$. . . 83
5.6 The dots comes from simulation for box size $50d_p \times 16d_p \times 120d_p$ at the height $17d_p$ under its surface. The orange line is the model ignoring the non-local term. The red, purple, and green lines come from the model including the non-local term with the same vertical velocity $V_z(0)/V_w = -0.07$ on the shearing wall but different non-local length l and gradient of velocity on the shearing wall. For the green line we set $l = 10d_p$, $V_z(0)/V_w = -0.07$, $\frac{dV_z(0)}{dy} = -0.6V_z(0)/d_p$. For the red line we set $l = 10d_p$, $V_z(0)/V_w = -0.052$, $\frac{dV_z(0)}{dy} = -0.1V_z(0)/d_p$. For the purple line we set $l = 1d_p$, $V_z(0)/V_w = -0.08$, $\frac{dV_z(0)}{dy} = -0.99V_z(0)/d_p$. 84
5.7 Profile of the stress σ_{yz}. We set $l = 10d_p$, $V_z(0)/V_w = -0.07$, $\frac{dV_z(0)}{dy} = -0.6V_z(0)/d_p$. The direction of σ_{yz} is different as in the simulation and its order of magnitude is much larger. 84
5.8 Profiles of the stress σ_{yz}. We set $l = 10d_p$, $V_z(0)/V_w = -0.052$, $\frac{dV_z(0)}{dy} = -0.1V_z(0)/d_p$ (red line) and $l = 1d_p$, $V_z(0)/V_w = -0.08$, $\frac{dV_z(0)}{dy} = -0.99V_z(0)/d_p$ (purple line). The direction of σ_{yz} and its order of magnitude are the same as in the simulation. 85
5.9 Wall stress ratio σ_{yy}/σ_{yz} for the shearing wall in the simulation ($H = 60d_p$). 85

LIST OF TABLES

Number *Page*

3.1 For all models, the particle density, ρ_p, is 2500, and the Savage number S_a is 2×10^{-6}. 32

Chapter 1

INTRODUCTION

1.1 Background and motivation

A granular material is a large collection of solid particles. The individual particles that make up a granular material are of sufficient size to not be affected by fluctuations in thermal motion. Examples of granular materials include sand, glass beads, and powders. Unlike a single phase of matter, granular materials exhibit properties akin to solids, liquids, or gases, depending on their density and velocity (MiDi, 2004; Goldhirsch, 2003). It is possible for different phases to coexist simultaneously, as demonstrated in figure 1.1.

A unifying theory of granular material that can be described by continuum models has been a goal of researchers in the past few decades. Many theoretical studies have been done in the past (Pouliquen, Cassar, et al., 2006; Cruz et al., 2005; MiDi, 2004; Jop, 2008; Sun and Sundaresan, 2011a; Bocquet, Colin, and Ajdari, 2009). These theoretical studies are mostly for steady state conditions and homogeneous systems (Kamrin and Koval, 2012) with the assumption of constant volume fraction. The following sections summarize some of these models.

Although numerous phenomena remain unexplained by existing models, our research concentrates on the enigmatic behavior of wall force anomalies and vortex flows. In Couette cell experiments and vertical plane shear simulations, granular material exhibits a downward flow in proximity to the vertical shearing wall and an upward flow adjacent to another static vertical wall. Intriguingly, this vortex flow provokes a change in the direction of vertical shear stress upon the initiation of wall shearing, challenging the widely held assumption that particles persistently exert a downward force on the vertical wall (Krishnaraj and Nott, 2016).

1.2 Constitutive model

$\mu - I$ rheology

To investigate stress in granular materials, consider a granular material composed of beads characterized by density (ρ_p) and diameter (d), subjected to normal stress (P) and sheared at a constant shear rate ($\dot{\gamma}$). The friction coefficient can be determined by dividing the shear stress (τ) by the normal stress (P), yielding $\mu = \tau/P$. The friction

coefficient (μ) and the volume fraction (ϕ) both rely on a single dimensionless parameter known as the inertial number, represented by I. This parameter is defined as the ratio of the microscopic time scale associated with particle rearrangement ($d/\sqrt{P/\rho_p}$) to the macroscopic time scale for deformation ($1/\dot{\gamma}$), given by $I = \dot{\gamma}d/\sqrt{P/\rho_p}$ (Jop, Forterre, and Pouliquen, 2005; Cruz et al., 2005; MiDi, 2004). The physical depictions of T_γ and T_p can be found in Figure 1.2. Cruz et al. (2005) characterizes various regimes of granular materials. The transition between the quasistatic regime and the dense flow regime corresponds to the shift from intermittent to continuous flow, occurring at $I = 10^{-3}$. The transition from the dense flow regime to the fully collisional flow regime takes place at $I = 10^{-1}$. Figure 1.3 displays the force chain in a two-dimensional simulation for the quasi-static and collisional regimes.

To achieve constant stress shearing of granular materials, the applied stress from the wall must exceed a critical value, denoted as $\tau > \tau_y$, where τ_y represents the yield stress (Da Cruz et al., 2002; Coussot, Nguyen, et al., 2002; Coussot, Raynaud, et al., 2002; MiDi, 2004; Cruz et al., 2005). The relationships $\mu - I$ and $\phi - I$, which incorporate the yield stress, effectively describe steady uniform flows within the dense-inertial ($10^{-3} < I < 10^{-1}$) regime, as suggested by Jop, Forterre, and Pouliquen (2005), Cruz et al. (2005), and MiDi (2004).

For flow in the dense-inertia regime, $\mu - I$ is linear (Cruz et al., 2005).

$$\mu(I) = \mu_{min} + bI \tag{1.1}$$

where μ_{min} is the stress ratio to initiate a non-zero shear rate. With $\mu_{min} \approx 0.25$, and $b \approx 1.1$, and saturates for $I \geq 0.2$. The constant b is related to material properties such as friction coefficient, Young's modulus, and grain size.

Pouliquen proposed a more precise local law in the dense-inertia regime (Pouliquen, Cassar, et al., 2006).

$$\mu(I) = \mu_s + \frac{\mu_2 - \mu_s}{I_0/I + 1} \tag{1.2}$$

Typical values for glass beads in three dimensions are $\mu_s = \tan 21°$, $\mu_2 = \tan 33°$, and $I_0 = 0.3$. For the solid fraction,

$$\phi = \phi_{\max} - (\phi_{\max} - \phi_{\min})\, I, \tag{1.3}$$

with typical values $\phi_{max} = 0.6$ and $\phi_{min} = 0.5$.

Prior studies have shown that the local model, as given by equation (1.2), fails for the quasistatic regime ($I < 10^{-3}$). It can not capture the finite width shear band and the nonzero shear rate when the stress is below the yield stress for several inhomogeneous geometries (Pouliquen, Cassar, et al., 2006; Kamrin and Koval, 2012; Bouzid et al., 2013).

The local model under consideration exhibits ill-posed behavior at both low and high values of I (Barker et al., 2015). Ill-posed problems, such as this one, are characterized by an unbounded increase in short-wavelength perturbations, which often leads to numerically convergent and physical results that are dependent on the grid being used. However, in real physical systems, noise and initial conditions inevitably introduce variability, making this model unrealistic for describing the quasi-static and collision regimes.

Shear-band in local rheology

The width of the shear band predicted by local models is strongly dependent on the velocity of the moving wall. In the quasi-static limit, this width reduces to zero. This phenomenon can be observed in plane-shearing with gravity or in a Couette flow (Pouliquen, Cassar, et al., 2006). The stress distribution becomes non-uniform across the cell, with the ratio of shear stress to pressure decreasing as one moves away from the moving wall.

As a result, there exists a critical distance at which the ratio τ/P reaches the critical value μ_s and the inertial number I becomes zero. However, experiments have shown that a shear band with a thickness of 5-10 particle diameters persists at low velocities, contrary to what is predicted by the local model.

Nonlocal $\mu - I$ rheology

In recent years, alternative non-local models such as the non-local granular fluidity (NGF) model (Kamrin and Koval, 2012) and an integral equation incorporating a shear-induced self-activation process (Pouliquen and Forterre, 2009). These non-local models account for the fact that the shear stress at a given point is not only dependent on the local shear rate and pressure, but also on the shear rate at other points.

The non-local granular fluidity (NGF) model is an extension of the local rheology model that takes into account the properties of granular materials composed of spherical, quasi-monodisperse, and stiff grains, where the wave speed is much greater than the deformation speed. The NGF model introduces a dimensionless parameter, A, known as the nonlocal amplitude, which characterizes the cooperativity of flow in addition to the material parameters of the local rheology model (μ_s and b). This model has been successfully applied to steady two-dimensional (Kamrin and Koval, 2012) and three-dimensional (Henann and Kamrin, 2013) flows, and it has been shown to accurately predict the width of the shear band, even in the quasi-static regime (Henann and Kamrin, 2013).

In the NGF model, an order-parameter-like scalar field called the granular fluidity, denoted g, is introduced. The granular fluidity field g ranges from zero to infinity and enters the flow rule through the equation $\dot{\gamma} = g\mu$. Therefore, the granular fluidity may be interpreted as a pressure-weighted inverse viscosity field. In steady flow, the fluidity field is assumed to obey

$$\xi^2 \nabla^2 g = g - g_{\mathrm{loc}}(P, \mu), \tag{1.4}$$

where $g_{\mathrm{loc}} = \dot{\gamma}_{\mathrm{loc}}(P, \mu)/\mu$ is the local granular fluidity, with $\dot{\gamma}_{\mathrm{loc}}(P, \mu)$ given by the local law. The parameter, ξ,

$$\xi(\mu) = \frac{A}{\sqrt{|\mu - \mu_{\mathrm{s}}|}} d, \tag{1.5}$$

is the cooperativity length for plastic rearrangement and it is proportional to the grain size d, which imposes a characteristic length scale on the flow. In the NGF model, the

fluidity at a point is composed of both a local contribution represented by g_{loc} and a non-local contribution represented by "disturbances" from the neighboring material ($\xi^2\nabla^2 g$). It is crucial to note when the flow is uniform, the NGF model reduces to the local rheology model since the term $\nabla^2 g$ is zero. The differential equation (1.4) becomes linear and its solutions can be scaled by a constant, as $g_{loc} = 0$, resulting in the rate-independent behavior observed in slow flows. The inclusion of the Laplacian term in the equation leads to a natural spread of the flow near μ_s, with a decay determined by ξ, rather than a sudden cutoff in flow. However, the NGF model is not able to capture the behavior of dilatancy and shear-softening/hardening (Krishnaraj and Nott, 2016; Li and Henann, 2019).

In order to capture dilatancy. Dsouza and Nott (2020) proposed a constitutive model for slow flow by adding non-local terms to the critical state plasticity theory. The terms $\nabla^2\phi$ and $\nabla^2\nabla\cdot u$ added in the pressure couple the volume fraction and velocity fields such that the model incorporates dilatancy. The dominant constitute relation as mentioned in Dsouza and Nott (2020) is

$$\begin{aligned} \sigma &= -p\delta + \frac{2\mu}{\dot{\gamma}}\left(p_c \boldsymbol{D}' - \ell^2\Pi\nabla^2\boldsymbol{D}'\right), \\ p_c &= \Pi - \ell^2\frac{\mathrm{d}\Pi}{\mathrm{d}\phi}\nabla^2\phi, \\ p &= p_c\left(1 - \frac{\mu_b}{\dot{\gamma}}\nabla\cdot\boldsymbol{u}\right) + \ell^2\Pi\frac{\mu_b}{\dot{\gamma}}\nabla^2\nabla\cdot\boldsymbol{u}, \end{aligned} \tag{1.6}$$

where l is the length of the effective radius of the averaging volume as a measurement of non-locality. $\mu_b \equiv (n-1)/(n\mu)$ is the bulk plastic modulus, where n is a parameter corresponding to the material property and typically slightly greater than unity. μ is the friction coefficient of the material. p_c is the pressure at the critical state in the local model. The function Π is the pressure function at the critical state in the local model of critical state plasticity (Rao, Nott, and Sundaresan, 2008). It is equal to p_c when there is no gradient of volume fraction everywhere. For slow flow, its form was proposed as

$$\Pi = \alpha\frac{(\phi-\phi_{\min})^2}{(\phi_{\max}-\phi)^5} \quad \phi \geqslant \phi_{\min}, \quad \Pi = 0 \quad \phi < \phi_{\min}. \tag{1.7}$$

These equations, together with the conservation of momentum and mass, are of order four in velocity and three in volume fraction at steady state. Hence we need four boundary conditions for velocity and three boundary conditions for volume fraction. The model captures shear localization and dilatancy in the case of plane-shearing with and without gravity.

1.3 Transient/unsteady flow

The local model proposed by Pouliquen, Cassar, et al. (2006) was verified for 3D transient flows using simulations of the collapse of a cylindrical column of particles (Lacaze and Kerswell, 2009). It suggests that a viscoplastic theory local model is more generally applicable to transient, multidirectional, dense flows. However, experiments in which polystyrene beads and glass beads are sheared in a rheometer show a hysteresis effect as the shear rate is increased and decreased. In these experiments, the stress when stress is increasing is larger than when the stress is decreasing and cannot be explained by local model (Da Cruz et al., 2002). Their experiments also show a minimum torque τ_y is required for shearing the beads continuously. For $\tau < \tau_y$ the beads move initially and stop after a while (Da Cruz et al., 2002). A fixed $\mu - I$ relation for the accelerating phase was verified with DEM simulation in a rotating drum (Lin, Jiang, and Yang, 2020). An improved continuum model for predicting the coupled evolution of the effective friction coefficient and the fabric tensor during transient processes in granular simple shearing was presented in Rojas Parra and Kamrin (2019). This model provides predictions for the transient strength of granular media in the quasi-static regime, based on the kinematics and structure of the media. However, the transient form of the NGF model (Henann and Kamrin, 2014) has not yet been verified through simulation or experiments. Moreover, these models do not account for particle rotation.

1.4 Anisotropy, wall force anomaly, vortex flow

Slow vortex flow has been observed in simulations and experiments involving a cylindrical Couette cell (Krishnaraj and Nott, 2016). The anisotropic microstruc-

ture of the granular material (Sun and Sundaresan, 2011b; Magnanimo and Luding, 2011) can cause anomalous stress behaviors, such as the vertical shear stress changing sign upon shearing and the magnitudes of all components of the stress increasing roughly exponentially with depth (Krishnaraj and Nott, 2016). The slow vortex flow, which is much slower than the shearing speed, may provide insights into the transient behavior of granular materials. The experiments and simulations also suggest that dilation plays a significant role in vortex flow and that the volume fraction needs to be coupled with velocity, not as is often assumed in local models.

1.5 Discrete element modeling

Discrete element method (DEM) is a powerful tool for modeling the behavior of granular materials. It is a numerical technique that uses the principles of mechanics to simulate the interactions between individual particles in a granular system. In this thesis, we will be using DEM simulation to understand how granular materials behave. Essentially, it breaks down the big picture of how these materials behave and allows us to predict the macroscopic behavior of granular materials, such as their mechanical properties and response to external forces, from how they interact with one another microscopically. The particles are represented as discrete, three-dimensional objects, and their interactions are modeled using contact mechanics. By using DEM simulation, we can make predictions about the overall behavior of granular materials and what factors may affect them. So, in this thesis, we will be digging deep into granular materials using an open-source DEM simulation program LAMMPS (Large-scale Atomic/Molecular Massively Parallel Simulator) (Thompson et al., 2022) to gain a better understanding of their behavior.

1.6 Objective

Capturing the propagation of microscale physics to macroscale phenomena is an important problem for granular materials. Several problems have not been solved:

- Setting the boundary conditions.

- Predicting the timescale from unsteady state to steady state.

The main focus of this thesis is the examination of the two issues listed above for the slow flow of granular materials using experiments, simulation, and theory. The study employs a Couette cell in which glass beads and sand are subjected to shear by a rotating cylinder at varying speeds. The torque is concurrently measured during the experiment. Additionally, DEM simulations utilizing a plane-shear geometry and gravity are conducted to investigate the velocity profile between the shearing and static walls, with measurements taken of the forces exerted on both walls. The second last chapter uses continuum models to look at the secondary flow that is generated in the shearing experiments and simulations.

References

Barker, T et al. (2015). "Well-posed and ill-posed behaviour of the $\mu(I)$ -rheology for granular flow". In: *J. Fluid Mech.* 779, pp. 794–818.

Bocquet, Lydéric, Annie Colin, and Armand Ajdari (July 2009). "Kinetic theory of plastic flow in soft glassy materials". en. In: *Phys. Rev. Lett.* 103.3, p. 036001.

Bouzid, Mehdi et al. (Dec. 2013). "Nonlocal rheology of granular flows across yield conditions". en. In: *Phys. Rev. Lett.* 111.23, p. 238301.

Coussot, P, J S Raynaud, et al. (May 2002). "Coexistence of liquid and solid phases in flowing soft-glassy materials". en. In: *Phys. Rev. Lett.* 88.21, p. 218301.

Coussot, Philippe, Q D Nguyen, et al. (Apr. 2002). "Avalanche behavior in yield stress fluids". en. In: *Phys. Rev. Lett.* 88.17, p. 175501.

Cruz, Frédéric da et al. (Aug. 2005). "Rheophysics of dense granular materials: discrete simulation of plane shear flows". en. In: *Phys. Rev. E Stat. Nonlin. Soft Matter Phys.* 72.2 Pt 1, p. 021309.

Da Cruz, F et al. (Nov. 2002). "Viscosity bifurcation in granular materials, foams, and emulsions". en. In: *Phys. Rev. E Stat. Nonlin. Soft Matter Phys.* 66.5 Pt 1, p. 051305.

Dsouza, Peter Varun and Prabhu R Nott (Apr. 2020). "A non-local constitutive model for slow granular flow that incorporates dilatancy". In: *J. Fluid Mech.* 888.

Forterre, Yoël and Olivier Pouliquen (Jan. 2008). "Flows of Dense Granular Media". In: *Annu. Rev. Fluid Mech.* 40.1, pp. 1–24.

Goldhirsch, Isaac (Jan. 2003). "RAPID GRANULAR FLOWS". In: *Annu. Rev. Fluid Mech.* 35.1, pp. 267–293.

Henann, David L and Ken Kamrin (Apr. 2013). “A predictive, size-dependent continuum model for dense granular flows”. en. In: *Proc. Natl. Acad. Sci. U. S. A.* 110.17, pp. 6730–6735.

– (Sept. 2014). “Continuum thermomechanics of the nonlocal granular rheology”. In: *Int. J. Plast.* 60, pp. 145–162.

Jop, Pierre (Mar. 2008). “Hydrodynamic modeling of granular flows in a modified Couette cell”. en. In: *Phys. Rev. E Stat. Nonlin. Soft Matter Phys.* 77.3 Pt 1, p. 032301.

Jop, Pierre, Yoël Forterre, and Olivier Pouliquen (Oct. 2005). “Crucial role of sidewalls in granular surface flows: consequences for the rheology”. In: *J. Fluid Mech.* 541, pp. 167–192.

Kamrin, Ken and Georg Koval (Apr. 2012). “Nonlocal constitutive relation for steady granular flow”. en. In: *Phys. Rev. Lett.* 108.17, p. 178301.

Krishnaraj, K P and Prabhu R Nott (Feb. 2016). “A dilation-driven vortex flow in sheared granular materials explains a rheometric anomaly”. en. In: *Nat. Commun.* 7, p. 10630.

Lacaze, Laurent and Rich R Kerswell (Mar. 2009). “Axisymmetric Granular Collapse: A Transient 3D Flow Test of Viscoplasticity”. In: *Phys. Rev. Lett.* 102.10, p. 108305.

Li, Shihong and David L Henann (July 2019). “Material stability and instability in non-local continuum models for dense granular materials”. In: *J. Fluid Mech.* 871, pp. 799–830.

Lin, C-C, M-Z Jiang, and F-L Yang (Oct. 2020). “Developing A Rheological Relation for Transient Dense Granular Flows Via Discrete Element Simulation in A Rotating Drum”. In: *J. Mech.* 36.5, pp. 707–719.

Magnanimo, V and S Luding (June 2011). “A local constitutive model with anisotropy for ratcheting under 2D axial-symmetric isobaric deformation”. In: *Granular Matter* 13.3, pp. 225–232.

MiDi, Gdr (Aug. 2004). “On dense granular flows”. en. In: *Eur. Phys. J. E* 14.4, pp. 341–365.

Pouliquen, O, C Cassar, et al. (July 2006). “Flow of dense granular material: towards simple constitutive laws”. en. In: *J. Stat. Mech.* 2006.07, P07020.

Pouliquen, Olivier and Yoel Forterre (Dec. 2009). “A non-local rheology for dense granular flows”. en. In: *Philos. Trans. A Math. Phys. Eng. Sci.* 367.1909, pp. 5091–5107.

Rao, K K, P R Nott, and S Sundaresan (2008). “An introduction to granular flow”. In:

Rojas Parra, Eduardo and Ken Kamrin (Aug. 2019). “Capturing transient granular rheology with extended fabric tensor relations”. In: *Granular Matter* 21.4, p. 89.

Sun, Jin and Sankaran Sundaresan (Sept. 2011a). “A constitutive model with microstructure evolution for flow of rate-independent granular materials”. In: *J. Fluid Mech.* 682, pp. 590–616.

– (Sept. 2011b). “A constitutive model with microstructure evolution for flow of rate-independent granular materials”. In: *J. Fluid Mech.* 682, pp. 590–616.

Thompson, A. P. et al. (2022). “LAMMPS - a flexible simulation tool for particle-based materials modeling at the atomic, meso, and continuum scales”. In: *Comp. Phys. Comm.* 271, p. 108171. DOI: 10.1016/j.cpc.2021.108171.

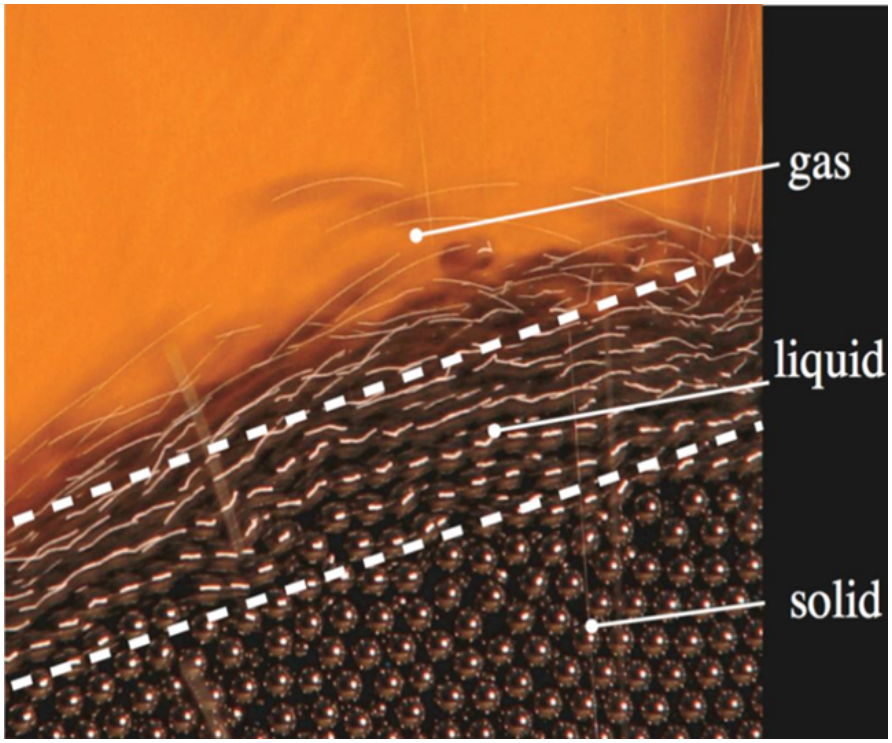

Figure 1.1: The steel beads flow down on a slope show different phases of granular material appear at the same time. (Forterre and Pouliquen, 2008)

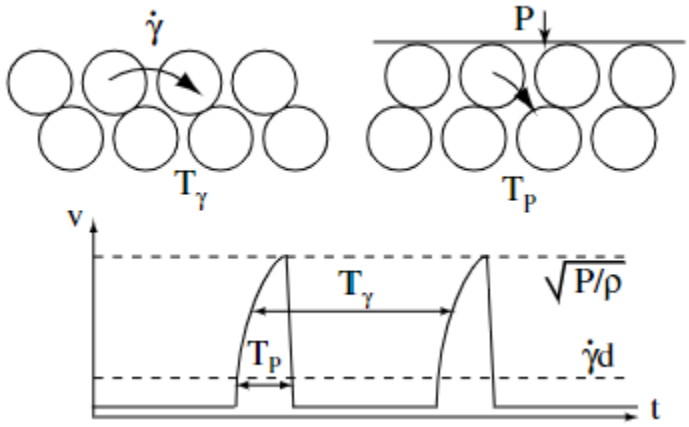

Figure 1.2: Illustration of the typical deformation time scale, T_γ, and the confinement time scale, T_p, depicting their physical significance. (MiDi, 2004)

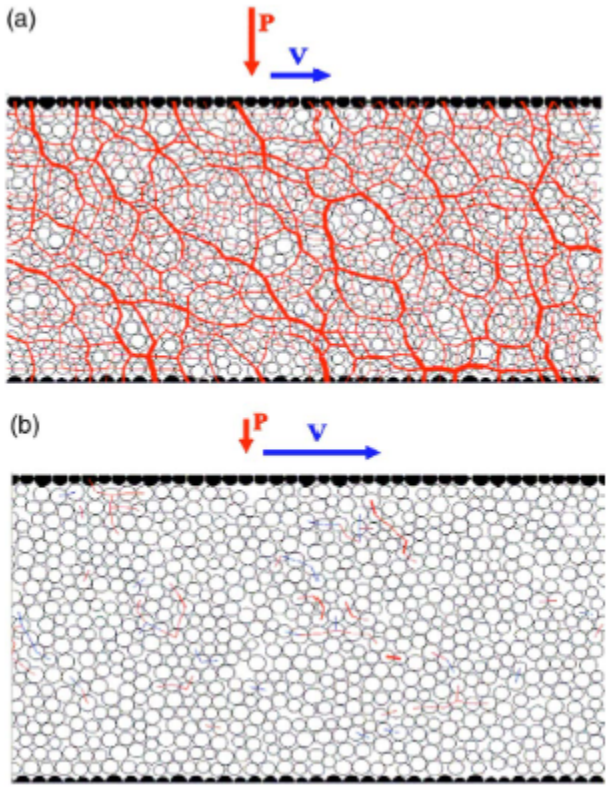

Figure 1.3: Two-dimensional plane shear simulation: (a) quasistatic regime ($I = 10^{-2}$); (b) collisional regime ($I = 0.2$). Black grains constitute the rough walls. The linewidths are proportional to the intensity of the normal force between grains. (Cruz et al., 2005)

Chapter 2

EXPERIMENTAL

2.1 Experimental background

Although there have been numerous experimental studies exploring the non-monotonic stress-velocity relationship in the quasistatic regime where $I \leq 10^{-3}$(Pouliquen et al., 2006; Cruz et al., 2005; MiDi, 2004; Fall et al., 2015; Tardos, McNamara, and Talu, 2003), there have been comparatively few investigations into the behavior of granular shear flows in the transient/unsteady state (Fall et al., 2015; Toiya, Stambaugh, and Losert, 2004).

In this experimental chapter, we present the results of our study on the unsteady/transient state, non-monotonically increasing stress-velocity behavior, and the presence of vortex flow. The aim of the research is to investigate the dynamic behavior of the granular flow in a given system and the effect of changing flow conditions on the stress-velocity relationship.

To conduct this study, we used a series of experiments with different shear rates, which were designed to induce transient flow behavior and produce non-monotonic stress-velocity relationships. We used a specialized powder rheometer to measure the transient stress behavior and to visualize the presence of vortex flow.

2.2 Setup

The rheometer (Anton Paar MCR-302, see figure 2.1) used in the experiments has a concentric cylinder in which different inner bobs (see fig. 2.2) can be used to shear the material (see figures 2.3 and 2.4). As found in fig. 2.4, the radius of rotating cylinder is r_i = 1.21 cm. The radius of the outer cylinder is r_o = 2.50 cm. The length of the inner cylinder L is 3.57 cm. The gap between the inner cylinder and the bottom of the column h ranges from 1.00 to 3.00 cm. The distance between the top surface of the filling sample and the top of the inner cylinder D ranges from 0 to 2.40 cm.

In most cases, the smooth cylinder or profiled cylinder was used to shear the samples. The rotational velocity or the torque can be controlled for the inner cylinder. In order to get precise data for the torque, the rheometer was calibrated for residual friction

and rotational inertia without a sample inside the cylinder. The rotational velocity ranges from 0.001 rpm to 1200 rpm. The torque applied to the sample by the shearing bob ranges from 2×10^{-8} to 200 $N \cdot m$.

With the rheometer, we can control the rotational speed, torque, height, and vertical force. An important feature is that air can be blown from the bottom through a porous plate to remove the memory of the sample. The air flow can be applied with rotation at the same time.

We used monodispersed glass beads in the experiments. The mean diameters are 25 μm and 100 μm. The density ρ is 2500 kg/m^3.

Previous experimental studies show some arbitrary residual stress of granular material may be present. The "memory" need to be erased before the tests (Da Cruz et al., 2002). The initiation of the flow is highly sensitive to the initial preparation of the sample and depends on the previous deformation history (Forterre and Pouliquen, 2008; Daerr and Douady, 1999). It's important to make the initial condition consistent before applying a force to the granular material. A useful method is to apply an upward flow of air to remove the memory. Figure 2.5 shows what happens when an upward flow is applied during experiments. Before 0 seconds, we put the sample material into the rheometer and then apply an upward air flow of 2 l/min for one minute. At 0 seconds, the inner cylinder started to rotate for 60 seconds. The initial normalized stress is around 0.26, where the normalized stress is defined as $T/r_i\rho g(D + 1/2L)A$. T is the torque measured by the rheometer. ρ is the bulk density. A is the side area contacting the material. At a fixed rotation speed, different air flow rates were applied from 60 seconds to 80 seconds. As shown in fig 2.5, with the upward air flow, the stress decreases suddenly. For air flows greater than 2 l/min, the normalized stress returned to the same initial value at 0 seconds. For lower flow rates, the stress at 80 seconds is higher. This demonstration shows that the upward flow is very effective for removing the history effect of samples. As a result, we applied an upward flow at 2 liter/min before every experiment. The air flow was applied before we inserted the shearing bob into the sample. Then

the memory can be eliminated and the sample is not compressed by the bob. After shearing begins, the collected data include the rotation speed, the torque, the height, and the vertical force at a fixed time step.

2.3 Torque control

We measured the rotation speed as a function of time by applying different levels of constant torque to the system. Figure 2.6 shows the rotation speed for 5 different values of imposed torque. For the torques at 10 $mN \cdot m$ and below, the bob rotated in the beginning but the rotation stopped because the torque applied is too small. This agrees well with a similar experiment by Da Cruz et al. (2002), where the experiments used a flat blade; in these experiments, the samples were prepared by shearing the sample but not by applying the air flow [fig. 2.7]. Our later experiments were conducted with constant rotational speed.

2.4 Steady time

Fig. 2.8 presents the normalized stress on the rough cylinder for gap $h = 2.0$ cm and diameter of glass bead $d = 25\mu m$ for rotational speeds from 10^{-3} to 10 rev/sec. For all rotational speeds, the initial normalized stress is 0.24 ± 0.02. The stress increases to values from 0.65 for 1 rev/sec to 0.8 for 10^{-3} rev/sec. The data are presented in terms of deflection angle ωt rather than time. The figure shows that independent of rotational speed, the stress reaches a maximum after approximately 20 revolutions. After reaching a maximum value, there is a modest decrease in stress.

Fig. 2.9 shows similar results using the smooth cylinder. The normalized stress rises to a value of 1.7 for the rotational speed from 10^{-3} to 0.1 rev/sec. For higher rotational speed from 1 to 10 rev/sec, the value of stress is lower and similar to the rough cylinder. Furthermore, as we compare the smooth cylinder to the rough cylinder for the same rotational speed of 0.01 rev/s, the stress is larger at the steady state for the smooth cylinder and reaches a maximum of around 100 revolutions for the smooth cylinder, which is longer than the rough cylinder [fig. 2.10]. The effect of the surface roughness differs from what was observed by Gutam, Mehandia, and

Nott (2013), in their experiment the rough cylinder is not profiled but a layer of particles is attached to the surface. Their results show that steady state is reached in 300 strain for the shear stress in vertical direction [fig. 2.11].

2.5 Non-monotonic relation of stress-velocity

Figure 2.12 shows the steady value of stress for different rotation speeds for both the smooth and rough cylinders for two different values of $D + L$. The steady values are from the experiments as shown in figs. 2.8 and 2.9 for $D + L = 3.8cm$. After the stress oscillation is below 5 %, we calculate the mean value of stress to find the steady value. As shown in fig. 2.12, the steady value of stress is larger at low speeds below 0.1 rev/sec. The stress starts to decrease when the rotation speed increases beyond 0.1 rev/sec. This effect is more significant for the smooth cylinder. We also inserted the cylinder deeper to see how the stress changed. However, the normalized stress differs with $D + L$ for both the smooth and the rough cylinders. We think there is a fundamental structural difference for the glass bead near the boundary of the shearing surface that causes stress to be larger and the steady time to be longer for the smooth cylinder than for the rough cylinder.

Figures 2.13 and 2.14 show the normalized stress for the smooth cylinder with larger glass bead $d = 100\mu m$. Compared with smaller glass beads $d = 25\mu m$, the normalized stress is larger for larger glass beads. Furthermore, an increase in depth $D + H$ results in an increase in the normalized stress, indicating a higher order rate of stress increase with depth than linear.

2.6 Vortex

As the cylinder began to rotate, the height of the top surface initially dropped slightly near the shearing cylinder but remained unchanged thereafter. The particles on the top surface migrated from the wall towards the center. Due to the difficulty in visualizing the movement of glass beads, we used sand to track the flow of the top surface [see Fig. 2.15]. We employed the open-source software OpenPIV (Liberzon et al., 2020) to visualize the velocity of the sand. The radial velocity of the sand

towards the center of the top surface was approximately $5.6 \times 10^{-4} \times V_{wall}$, which is significantly smaller than the shearing velocity of the smooth bob. This finding provides an explanation for the slow increase in wall stress that is independent of wall velocity. We believe that the variation of the solid fraction near the shearing surface plays an important role in the appearance of vortex flow and the slow increase in stress. However, since the solid fraction is hard to measure in the experiments, we will investigate its variation by conducting simulations in the following chapters.

2.7 Conclusions

In conclusion, we conducted a series of experiments to study granular flow in the transient/unsteady state and the effect of changing the shear rate on the stress-velocity relationship. Our experiments show blowing upward air flow eliminates the memory of granular material. The procedure produces a consistent initial state before the bob rotates. Our results show that the steady state of the smooth cylinder is reached after approximately 20 revolutions, which corresponds to around 160 strains, and that the stress reaches a maximum value that is independent of rotational speed in the quasi-static regime. We also observed a non-monotonic relationship between stress and velocity, where the stress does not increase with increasing rotational speed. Additionally, we visualized the movement of particles on the top surface and found that the radial velocity of the sand towards the center of the top surface is significantly smaller than the shearing velocity of the smooth bob. We also found that using larger glass beads results in a higher order increase of stress with depth than linear. Further investigation will be done in the following chapters by conducting simulations to better understand the variation of the solid fraction.

References

Cruz, Frédéric da et al. (Aug. 2005). “Rheophysics of dense granular materials: discrete simulation of plane shear flows”. en. In: *Phys. Rev. E Stat. Nonlin. Soft Matter Phys.* 72.2 Pt 1, p. 021309.

Da Cruz, F et al. (Nov. 2002). “Viscosity bifurcation in granular materials, foams, and emulsions”. en. In: *Phys. Rev. E Stat. Nonlin. Soft Matter Phys.* 66.5 Pt 1, p. 051305.

Daerr, Adrian and Stéphane Douady (May 1999). “Two types of avalanche behaviour in granular media”. en. In: *Nature* 399.6733, pp. 241–243.

Fall, Abdoulaye et al. (2015). “Dry granular flows: Rheological measurements of the μ (I)-rheology”. In: *J. Rheol.* 59.4, pp. 1065–1080.

Forterre, Yoël and Olivier Pouliquen (Jan. 2008). “Flows of Dense Granular Media”. In: *Annu. Rev. Fluid Mech.* 40.1, pp. 1–24.

Gutam, Kamala Jyotsna, Vishwajeet Mehandia, and Prabhu R Nott (July 2013). “Rheometry of granular materials in cylindrical Couette cells: Anomalous stress caused by gravity and shear”. In: *Phys. Fluids* 25.7, p. 070602.

Liberzon, Alex et al. (July 2020). *OpenPIV/openpiv-python: OpenPIV - Python (v0.22.2) with a new extended search PIV grid option*.

MiDi, Gdr (Aug. 2004). “On dense granular flows”. en. In: *Eur. Phys. J. E* 14.4, pp. 341–365.

Pouliquen, O et al. (July 2006). “Flow of dense granular material: towards simple constitutive laws”. en. In: *J. Stat. Mech.* 2006.07, P07020.

Tardos, Gabriel I, Sean McNamara, and Ilkay Talu (Mar. 2003). “Slow and intermediate flow of a frictional bulk powder in the Couette geometry”. In: *Powder Technol.* 131.1, pp. 23–39.

Toiya, Masahiro, Justin Stambaugh, and Wolfgang Losert (Aug. 2004). “Transient and oscillatory granular shear flow”. en. In: *Phys. Rev. Lett.* 93.8, p. 088001.

Figure 2.1: The rheometer used in the experiments

Figure 2.2: Different types of rotating bobs.

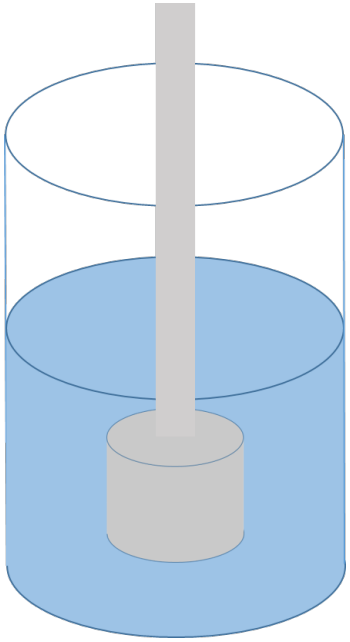

Figure 2.3: The rotating bob and the container.

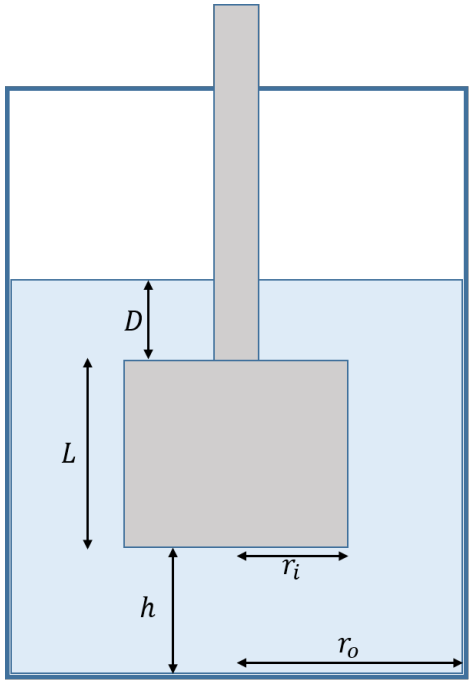

Figure 2.4: Size of the bob and the container.

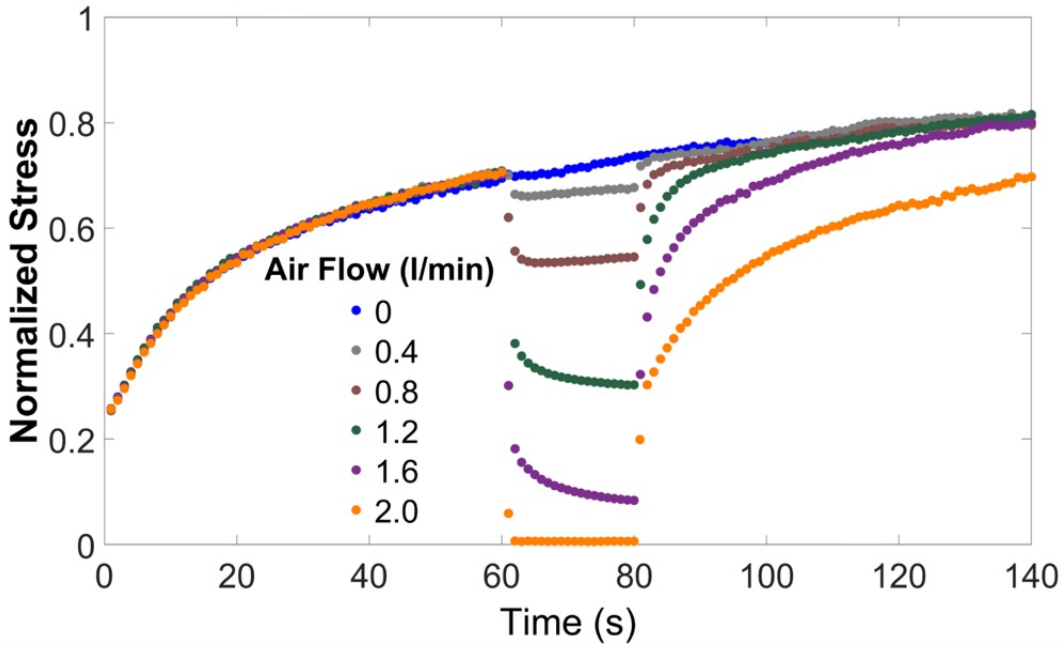

Figure 2.5: Memory elimination using an upward flow of air with glass beads diameter $d = 25\mu m$. Rough cylinder. Shear rate is 5.8/s. $D = 2.6cm$. $h = 1.0cm$. The normalized stress is $\tau/r_i A$, where τ is the torque and A is the area of the side wall that contact with particles.

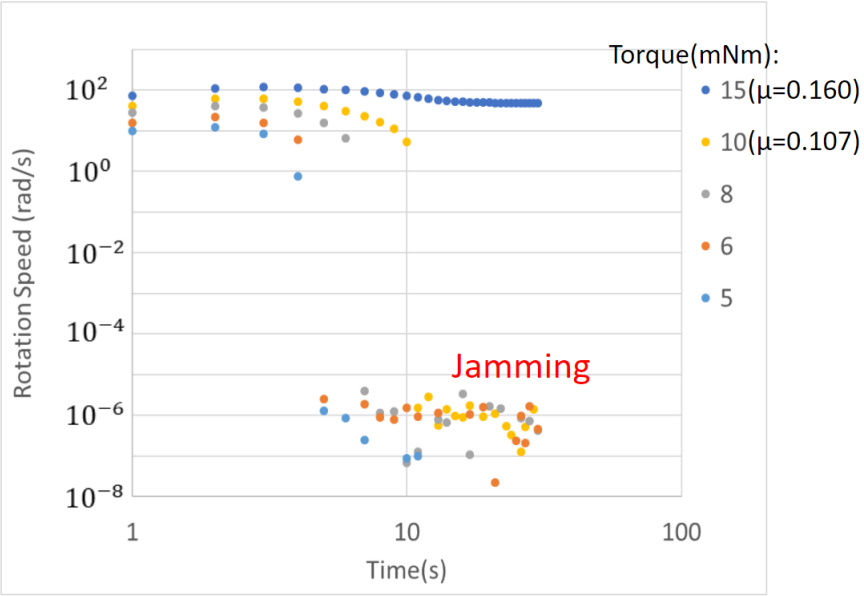

Figure 2.6: Constant torque experiments. Rotation stops for torques below the critical value. Rough bob. 25 μm glass bead.

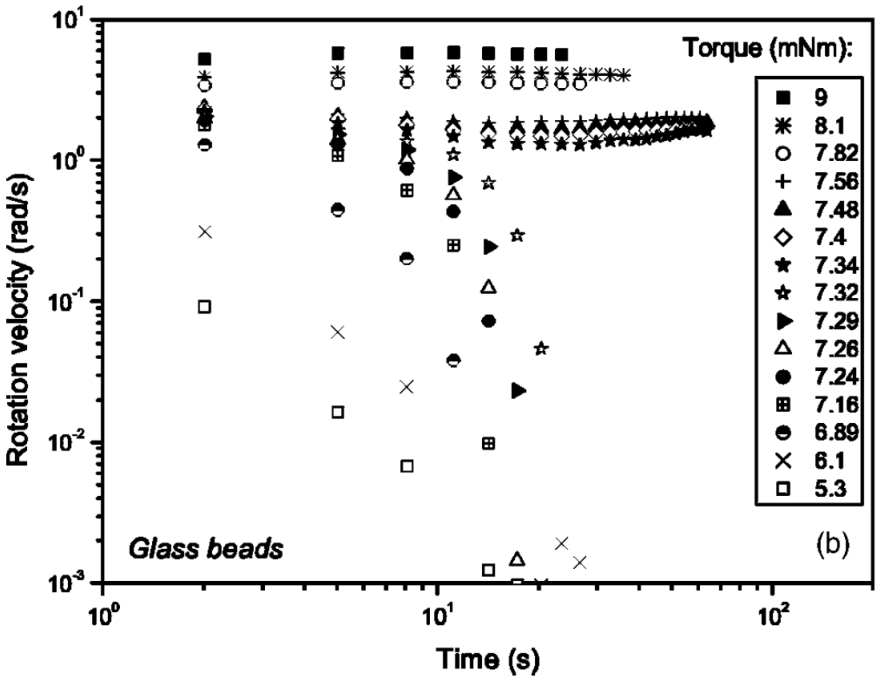

Figure 2.7: Experiments using a blade to shear the glass beads with different constant torque. (preparation by using constant shear rate $50s^{-1}$ during 10 s, no rest) from Da Cruz et al. (2002)

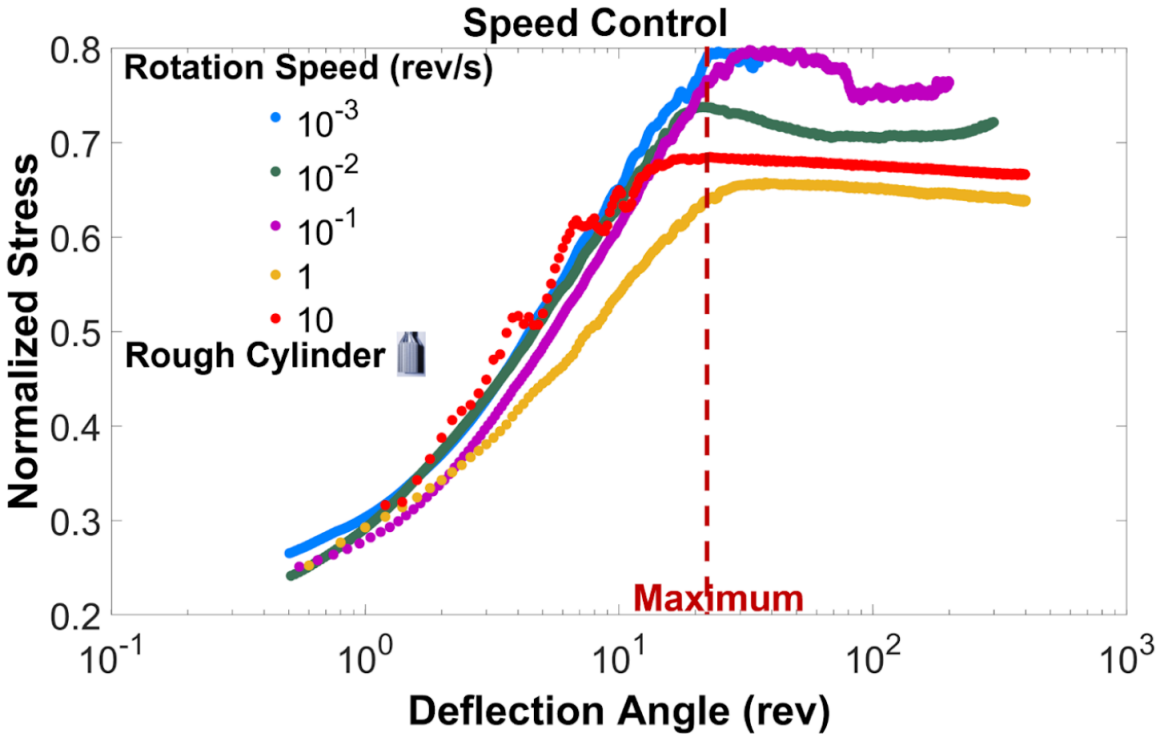

Figure 2.8: Transition of wall stress in different rotational speeds for the rough cylinder. $h = 2.0cm$, $D + L = 3.8cm$. $25\mu m$ glass bead. For a rotation speed of 1 rev/s, the corresponding inertia number and shear rate are $I = 8.8 \times 10^{-4}$ and $\dot{\gamma} = 8.2/s$.

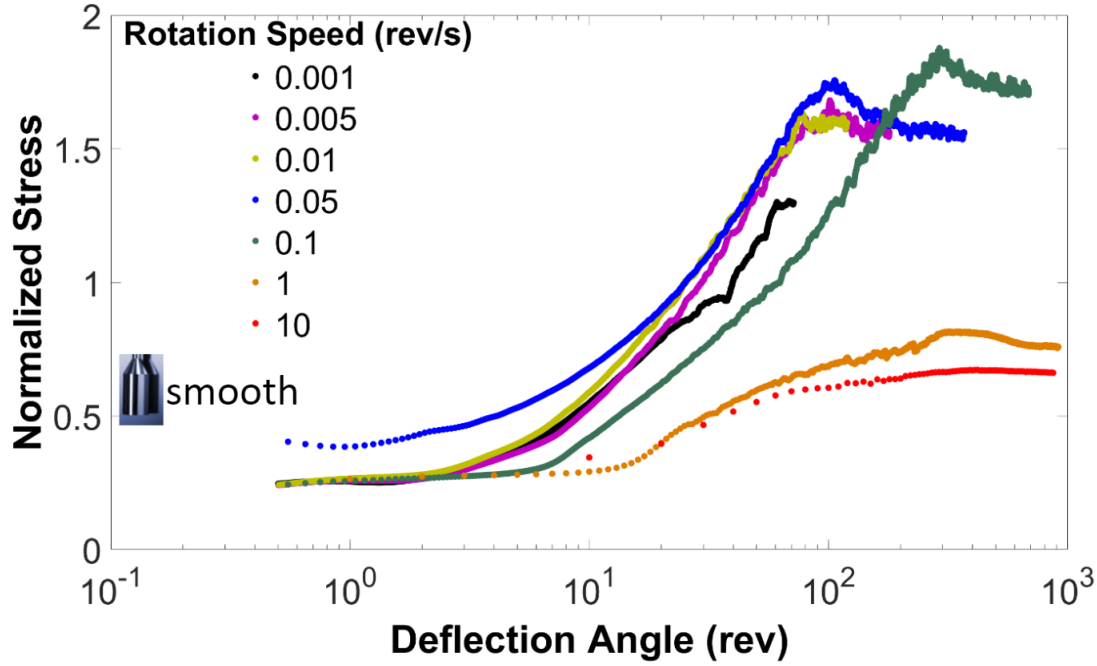

Figure 2.9: Transition of wall stress in different rotational speeds for the smooth cylinder. $h = 2.0cm$, $D + L = 3.9cm$. $25\mu m$ glass bead.

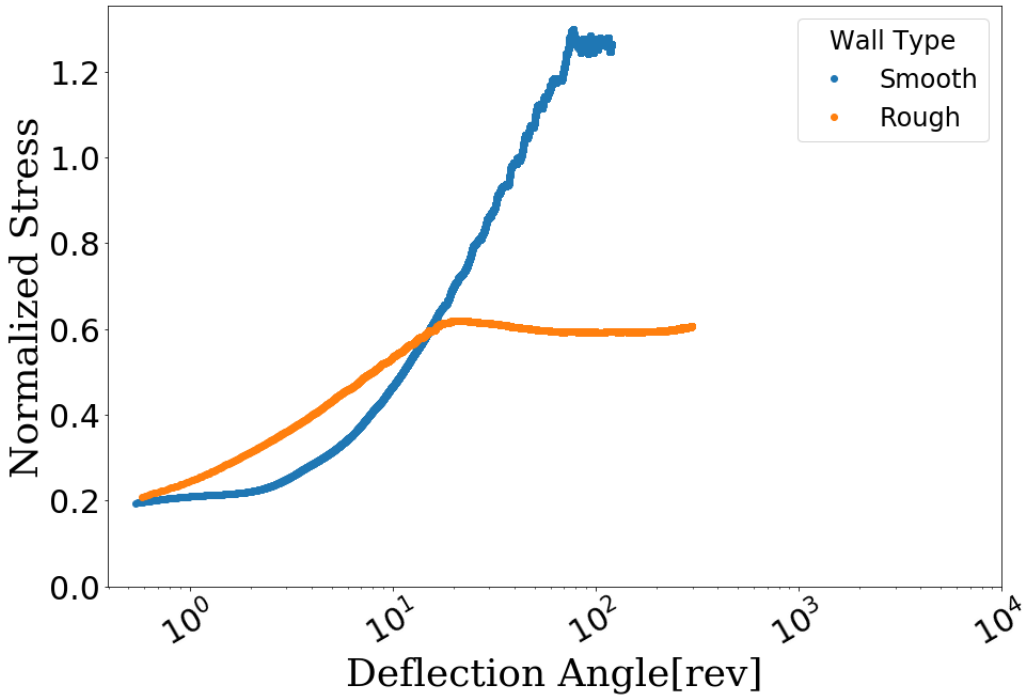

Figure 2.10: Transition time of wall stress is longer for the smooth cylinder than the rough cylinder. The data are from figs. 2.8 and 2.9 for 0.01 rev/s.

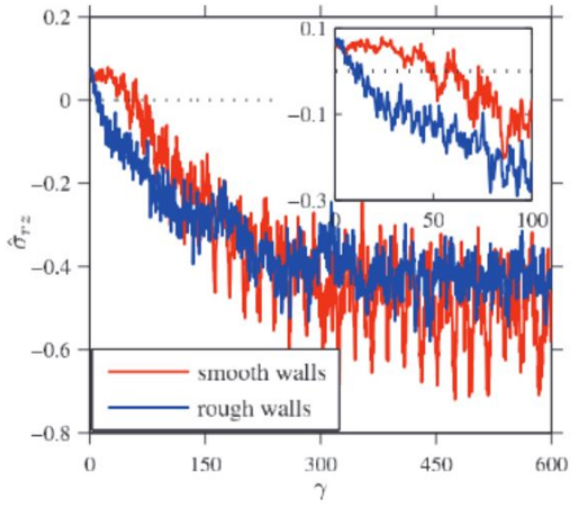

(a)

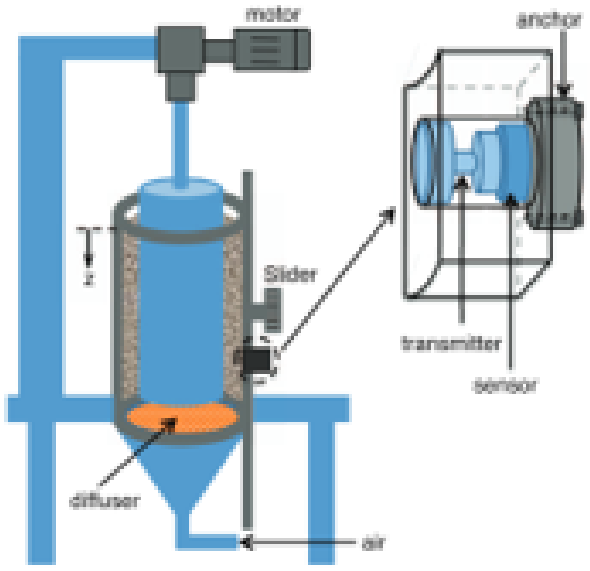

(b)

Figure 2.11: Kamala Jyotsna Gutam, Vishwajeet Mehandia, and Prabhu R. Nott (2013)

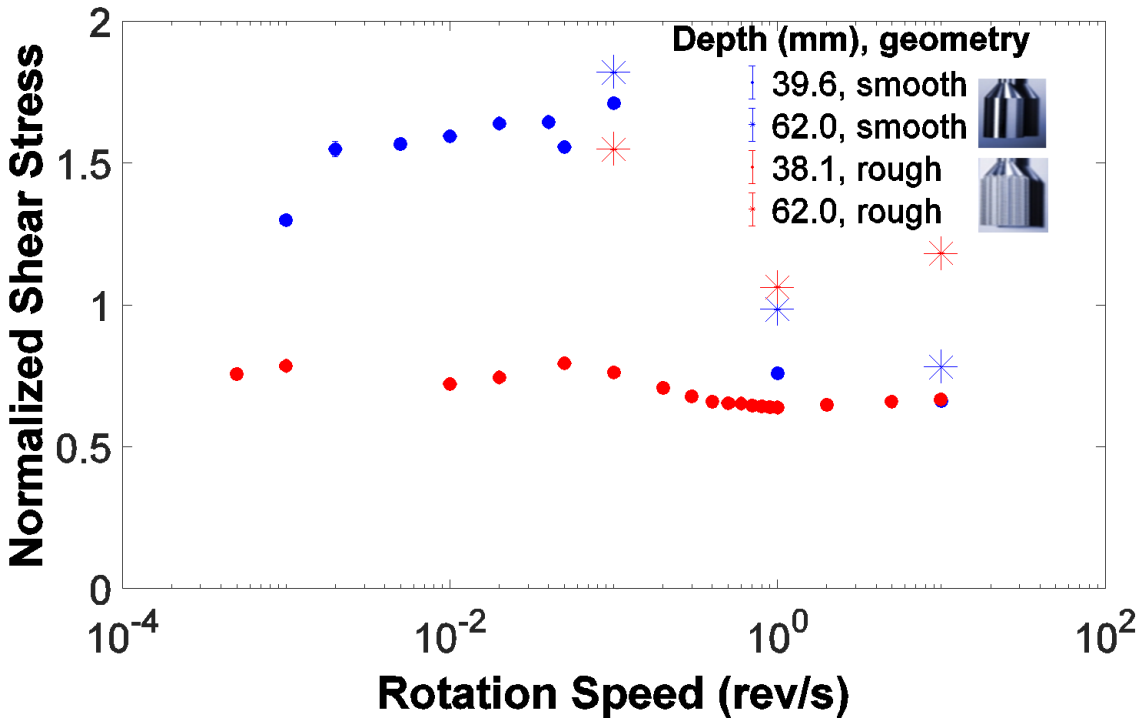

Figure 2.12: Non-monotonic stress-speed relation. The depth is $D + L$, and the particles are $25\mu m$.

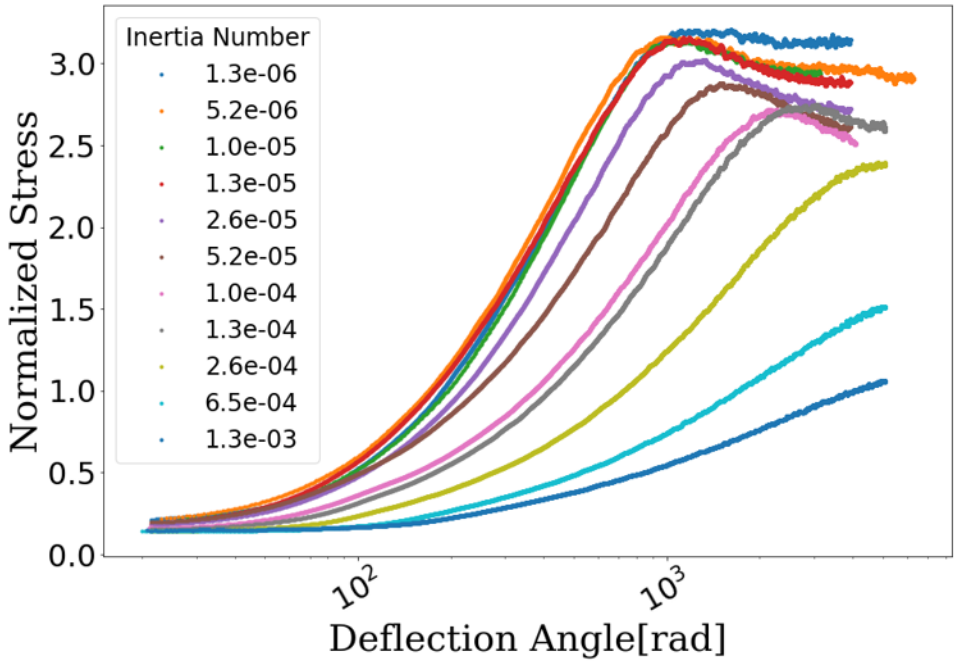

Figure 2.13: Using smooth bob. $100\mu m$ glass bead. $h = 1.0cm$, $D + L = 4.25cm$

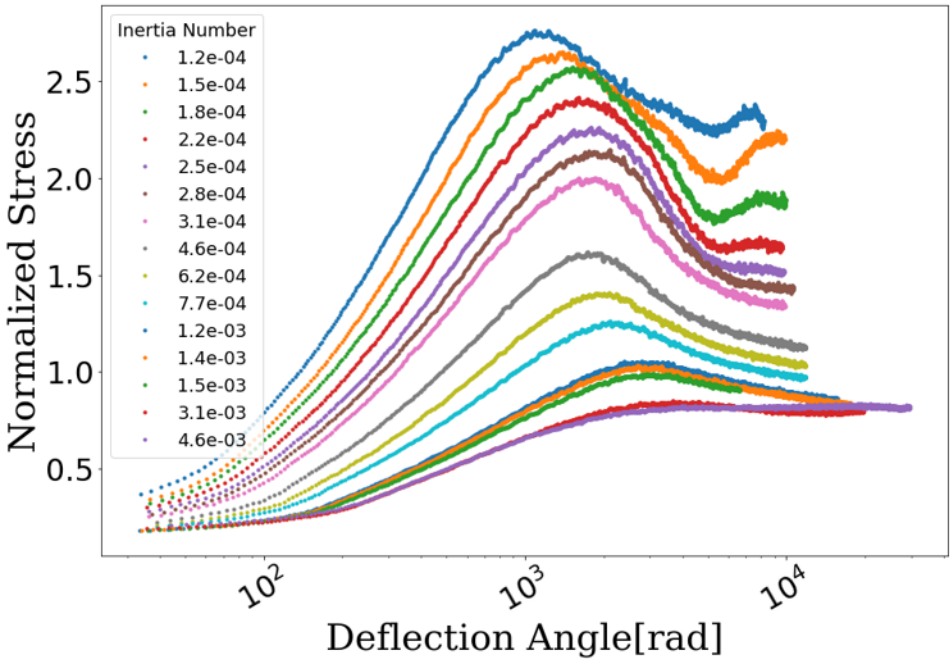

Figure 2.14: Using smooth bob. $100\mu m$ glass bead. $h = 2.0cm$, $D + L = 3.0cm$

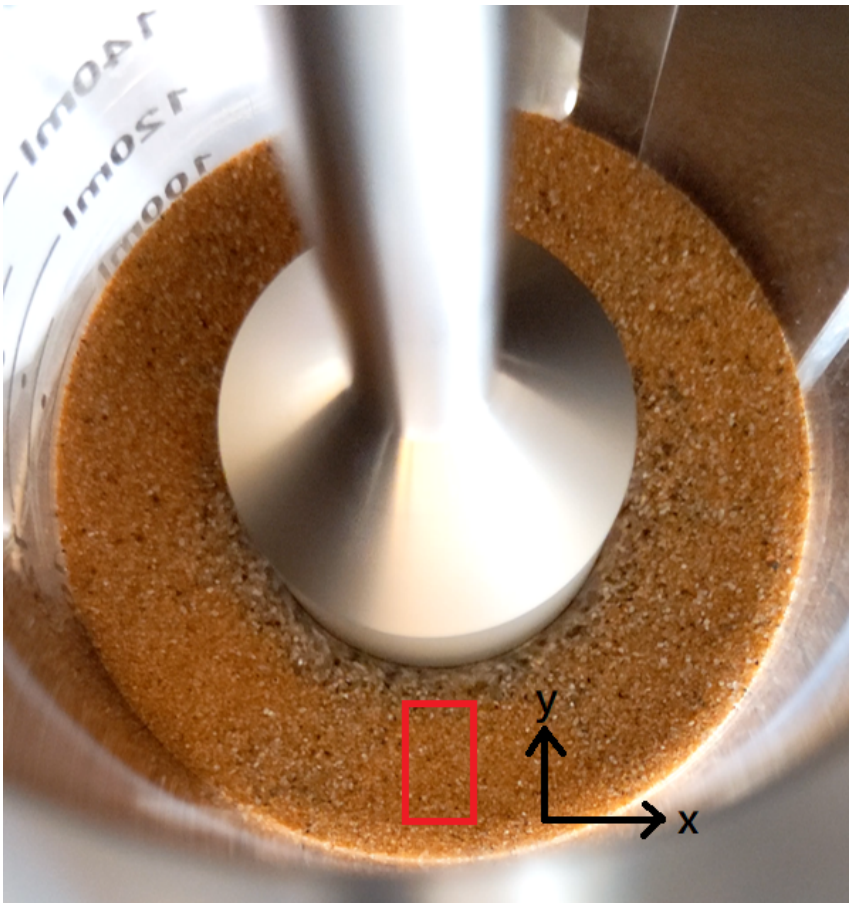

(a)

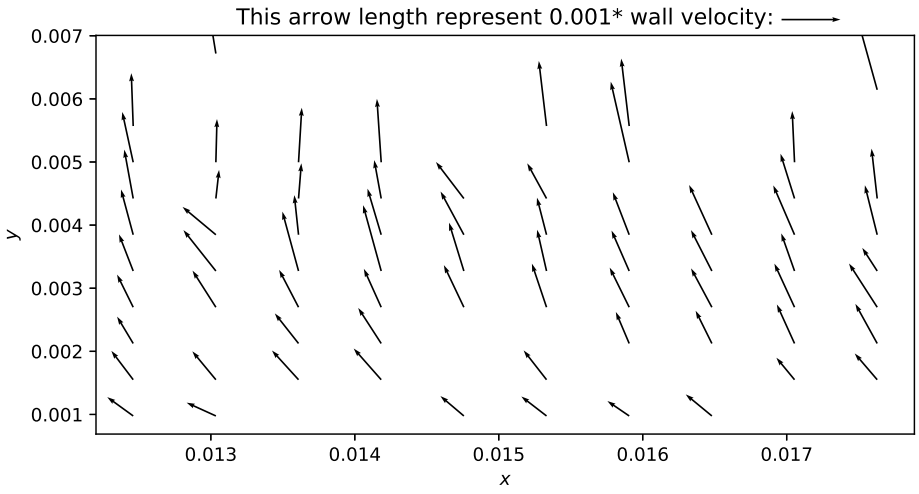

(b)

Figure 2.15: Surface flow. The velocity of particles in the red frame in (a) is slow enough to use the visualization method to calculate the velocity field by comparing snapshots of the recording video. The average value of radial velocity in the red frame on the top surface $V_r r/r_i \approx 5.6 \times 10^{-4} \times V_{wall}$

.

Chapter 3

SIMULATION PREPARATION

3.1 Setup

In our research, we employ the discrete element method (DEM) to simulate the movement of particles. DEM is a widely used computational tool in granular mechanics, which tracks the positions and interactions of multiple small particles in time using contact models. Specifically, we utilize a soft-particle contact model, as described in previous studies by Cundall and Strack (1979) and Walton and Braun (1986). In this model, the grains are treated as deformable spheres and are allowed to overlap, rather than calculate their deformation in detail. The motion of each particle is calculated by integrating Newton's second law, taking into account pairwise interaction forces. To perform these computationally intensive simulations, involving the tracking of approximately 100,000 particles, we use the open-source program LAMMPS (Large-scale Atomic/Molecular Massively Parallel Simulator) package (Plimpton, 1995; Thompson et al., 2022).

Contact model

The most common contact models in DEM simulations for granular materials are the Hookean style contact model and the Hertzian style contact model, as described in Brilliantov et al. (1996), Silbert et al. (2001), and Zhang and Makse (2005). The contact forces are calculated when the distance r between two particles of radii R_i and R_j is less than their contact distance $d = R_i + R_j$. There is no force between the particles when $r > d$.

The Hookean model uses the expression below to determine the force acting between the particles:

$$F_{hk} = \left(k_n \delta \mathbf{n}_{ij} - m_{eff}\gamma_n \mathbf{v}_n\right) - \left(k_t \Delta \mathbf{s}_t + m_{eff}\gamma_t \mathbf{v}_t\right) \tag{3.1}$$

The Hertzian model uses the following expression to determine the force acting

between the particles:

$$\begin{aligned} F_{hz} &= \sqrt{\delta}\sqrt{\frac{R_i R_j}{R_i + R_j}} F_{hk} \\ &= \sqrt{\delta}\sqrt{\frac{R_i R_j}{R_i + R_j}} \left[\left(k_n \delta \mathbf{n}_{ij} - m_{eff} \gamma_n \mathbf{v}_n \right) - \left(k_t \Delta \mathbf{s}_t + m_{eff} \gamma_t \mathbf{v}_t \right) \right] \end{aligned} \tag{3.2}$$

In the proposed model, the interaction between particles is described by normal and tangential forces, each consisting of two components: an elastic force and a damping force. The normal elastic force represents the restorative force between particles, while the tangential elastic force captures the history effect, accounting for the accumulated tangential displacement during particle contact. Both damping forces represent energy dissipation within the system. Additionally, the model takes into consideration particle rotation.

The other quantities in the equations are as follows:

- δ = d − r = overlap distance of 2 particles
- K_n = elastic constant for normal contact
- K_t = elastic constant for tangential contact
- γ_n = viscoelastic damping constant for normal contact
- γ_t = viscoelastic damping constant for tangential contact
- $m_{eff} = M_i M_j / \left(M_i + M_j \right)$ = effective mass of 2 particles of mass M_i and M_j
- Δs_t = tangential displacement vector between 2 particles which is truncated to satisfy a frictional yield criterion
- n_{ij} = unit vector along the line connecting the centers of the 2 particles
- V_n = normal component of the relative velocity of the 2 particles
- V_t = tangential component of the relative velocity of the 2 particles

The K_n, K_t, γ_n, and γ_t coefficients are specified as parameters. The parameters K_n and K_t can be set to values that correspond to the properties of the material being modeled. Specifically, $K_n = 4G/(3(1-\nu))$, where ν = the Poisson ratio, G = shear modulus = $E/(2(1+\nu))$, and E = Young's modulus in the Hertzian case. Another parameter is $K_t = 4G/(2-\nu)$, which is used in the Hertzian case (Zhang and Makse, 2005).

Model	k_n	k_t	γ_n	γ_t	μ	d_p
Hooke 1	$10^6 m_{\mathrm{p}} g/d_{\mathrm{p}}$	$2/7k_n$	$317g/d_{\mathrm{p}}$	$1/2\gamma_n$	0.5	8.3×10^{-4}
Hooke 2	$10^6 m_{\mathrm{p}} g/d_{\mathrm{p}}$	$2/7k_n$	$317g/d_{\mathrm{p}}$	$1/2\gamma_n$	0.5	10^{-4}
Hertz 2	5.857×10^{10}	5.133×10^{10}	2.946×10^{-6}	2.582×10^{-6}	0.5	10^{-4}

Table 3.1: For all models, the particle density, ρ_p, is 2500, and the Savage number S_a is 2×10^{-6}.

After establishing the contact model, we numerically integrate Newton's equations of motion for a system of interacting particles. Both translational and rotational motion are taken into account, where the translational motion is described by the equation:

$$m_i \frac{\partial \boldsymbol{v_i}}{\partial t} = \sum_j \boldsymbol{F_{ij}} \tag{3.3}$$

and the rotational motion is described by the equation:

$$I_i \frac{\partial \boldsymbol{\omega_i}}{\partial t} = \sum_j \boldsymbol{\tau_{ij}}, \tag{3.4}$$

where $\boldsymbol{v_i}$ is the translational velocity of particle i, m_i is the mass of particle i, $\boldsymbol{F_{ij}}$ is the force acting on particle i from particle j, $\boldsymbol{\omega_i}$ is the angular velocity of particle i, I_i is the moment of inertia of particle i, and $\boldsymbol{\tau_{ij}}$ is the torque acting on particle i from particle j. By solving these equations, we can accurately simulate the dynamics of the system and study its behavior.

DEM algorithm

In order to solve the equations of motion in our simulations, we use a finite difference approach and integrate them over time using a molecular dynamics algorithm. One commonly used algorithm for this purpose is the Verlet algorithm (Swope et al., 1982). This algorithm is based on a Taylor expansion of the positions, $x(t)$, and velocities, $v(t)$, around the current time, t. It provides a step-by-step solution to the equations of motion and allows us to track the movement of particles over time. The first time step in the Verlet algorithm is

$$\begin{aligned} \vec{x}(t+\Delta t) &= \vec{x}(t) + \vec{v}(t)\Delta t + \tfrac{1}{2}\vec{a}(t)\Delta t^2 \\ \vec{v}(t+\Delta t) &= \vec{v}(t) + \tfrac{\vec{a}(t)+\vec{a}(t+\Delta t)}{2}\Delta t \end{aligned} \tag{3.5}$$

The standard implementation scheme of this algorithm is:

1. Calculate $\vec{v}\left(t+\frac{1}{2}\Delta t\right) = \vec{v}(t) + \frac{1}{2}\vec{a}(t)\Delta t$.
2. Calculate $\vec{x}(t+\Delta t) = \vec{x}(t) + \vec{v}\left(t+\frac{1}{2}\Delta t\right)\Delta t$.
3. Derive $\vec{a}(t+\Delta t)$ from the interaction potential using $\vec{x}(t+\Delta t)$.
4. Calculate $\vec{v}(t+\Delta t) = \vec{v}\left(t+\frac{1}{2}\Delta t\right) + \frac{1}{2}\vec{a}(t+\Delta t)\Delta t$.

Initial and Boundary Condition

In the simulation, a three-dimensional box is used. The length of the simulation box is $30d_p$. The width is $16d_p$. The periodic depth is $50d_p$.

Using different wall speeds, we control the flow from the quasi-static regime to the inertial regime. The flow regimes are characterized by the Savage number Sa, defined as the ratio of the stress due to grain inertia and the total stress,

$$Sa \equiv \frac{\rho d_{\mathrm{p}}^2 \dot{\gamma}^2}{N} \tag{3.6}$$

where ρ is the bulk density, and N is the Janssen stress scale $\rho g W$. For most situations, the Savage number we used is 2×10^{-6} where the flow is in a quasi-static regime.

We use a mixture of grains of diameter $0.9d_p$, d_p, and $1.1d_p$ (of mass fractions 0.3, 0.4, and 0.3, respectively) to avoid crystalline order. The grains were then randomly

put into a body-centered cubic lattice with an appropriate size that $1.1d_p$ grains are just in contact. The grains are filled up to a fill height of H, in the absence of gravity. After which gravity was turned on, and the grains started to fall. Once settled, the bed had an initial average volume fraction $\langle\phi\rangle = 0.602$. After falling, the wall started to move at a constant speed.

In our simulations, we investigate two different types of wall surfaces: smooth and rough. The rough walls are coated with a rigid, close-packed triangular lattice of grains with a diameter of 0.9 times the diameter of the particles being used. The interactions between the particles and the walls are treated as if the walls have infinite mass, but the same stiffness, damping, and friction constants as the grain-grain interactions. Additionally, we test two different filling methods, one in which particles are placed on a lattice, and another in which they are added layer by layer, like rain. We found that the volume-fraction distributions at the steady state for the two filling methods were almost identical, indicating that the initial preparation of the granular bed has little effect on its properties at the steady state.

3.2 Simulation Time Step and Comparison of different sample frequencies of variables output

For the Hooke model, the collision time t_{col} is given by (Silbert et al., 2001)

$$t_{\text{col}} = \pi \left(2k_n/m - \gamma_n^2/4\right)^{-1/2} \tag{3.7}$$

The spring constant used in the simulation should be chosen with care, as it affects the accuracy of the simulation results. It should be large enough to prevent inter-penetration of the particles but not so large that it requires an excessively small time step, δt. An accurate simulation typically requires $\delta t \sim t_{col}/50$, where t_{col} is the characteristic collision time of the particles (Silbert et al., 2001). Therefore, the spring constant should be chosen such that it allows for a reasonable time step while still preventing interpenetration of the particles.

For the Hertz model, the collision time t_{col} without damping is given by (Antypov

and Elliott, 2011)

$$\tau_{\text{col}} = 2.214 \left(\frac{4\rho}{3k_n} \right)^{2/5} \frac{d}{v_0^{1/5}} \tag{3.8}$$

where v_0 is the relative velocity before two particles collide with each other. The collision time is proportional to $v^{-1/5}$, which results in a long collision time that slows the simulation.

We also checked different sample frequencies to output the average value of variables. We can either calculate the average values and output them every 10,000 or 1,000 time steps.

3.3 Comparison of Hertz and Hooke Model

In order to check if the transient behaviors are different for Herzian model and Hookian model, we ran simple shear simulations to check how the force acting on the wall varied. The value of wall stress and the transition time are approximately the same when using Hertz model and Hooke model as shown in fig 3.2. For both contact models, we saw there are vortex flows in the same direction.

The computing time for Hooke model is shorter than the Hertz model. Thus, we used the Hooke model in the following simulations.

References

Antypov, D and J A Elliott (May 2011). “On an analytical solution for the damped Hertzian spring”. en. In: *EPL* 94.5, p. 50004.

Brilliantov, N V et al. (May 1996). “Model for collisions in granular gases”. en. In: *Phys. Rev. E Stat. Phys. Plasmas Fluids Relat. Interdiscip. Topics* 53.5, pp. 5382–5392.

Cundall, P A and O D L Strack (Mar. 1979). “A discrete numerical model for granular assemblies”. In: *Geotechnique* 29.1, pp. 47–65.

Plimpton, Steve (Mar. 1995). “Fast Parallel Algorithms for Short-Range Molecular Dynamics”. In: *J. Comput. Phys.* 117.1, pp. 1–19.

Silbert, L E et al. (Nov. 2001). “Granular flow down an inclined plane: Bagnold scaling and rheology”. en. In: *Phys. Rev. E Stat. Nonlin. Soft Matter Phys.* 64.5 Pt 1, p. 051302.

Swope, William C et al. (Jan. 1982). “A computer simulation method for the calculation of equilibrium constants for the formation of physical clusters of molecules: Application to small water clusters”. In: *J. Chem. Phys.* 76, p. 637.

Thompson, A. P. et al. (2022). “LAMMPS - a flexible simulation tool for particle-based materials modeling at the atomic, meso, and continuum scales”. In: *Comp. Phys. Comm.* 271, p. 108171. DOI: 10.1016/j.cpc.2021.108171.

Walton, Otis R and Robert L Braun (Oct. 1986). “Viscosity, granular-temperature, and stress calculations for shearing assemblies of inelastic, frictional disks”. In: *J. Rheol.* 30, pp. 949–980.

Zhang, H P and H A Makse (July 2005). “Jamming transition in emulsions and granular materials”. en. In: *Phys. Rev. E Stat. Nonlin. Soft Matter Phys.* 72.1 Pt 1, p. 011301.

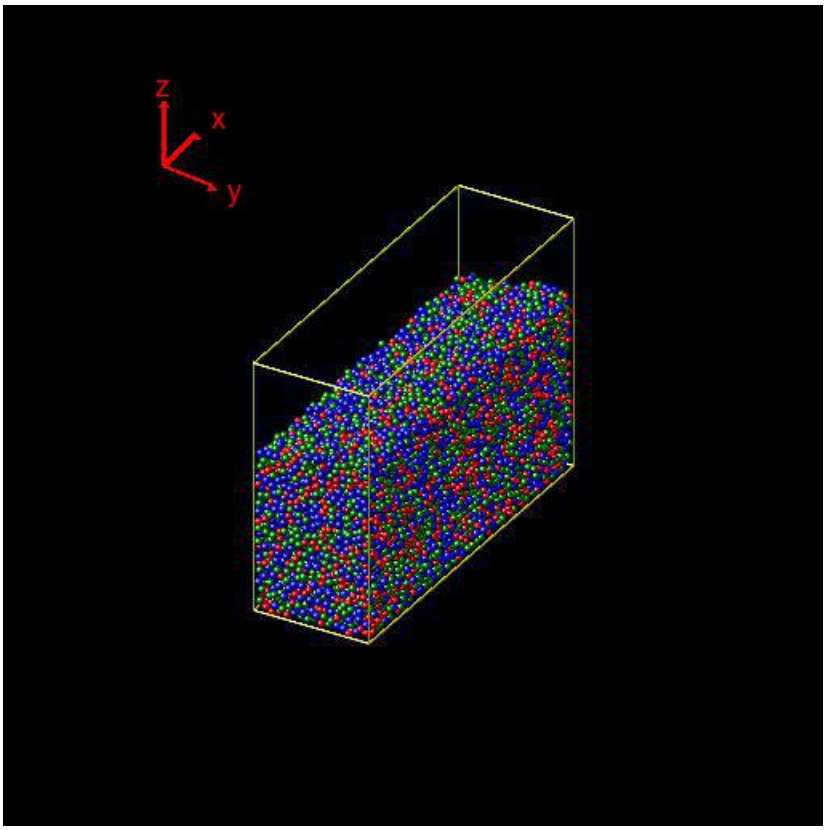

Figure 3.1: image when shearing

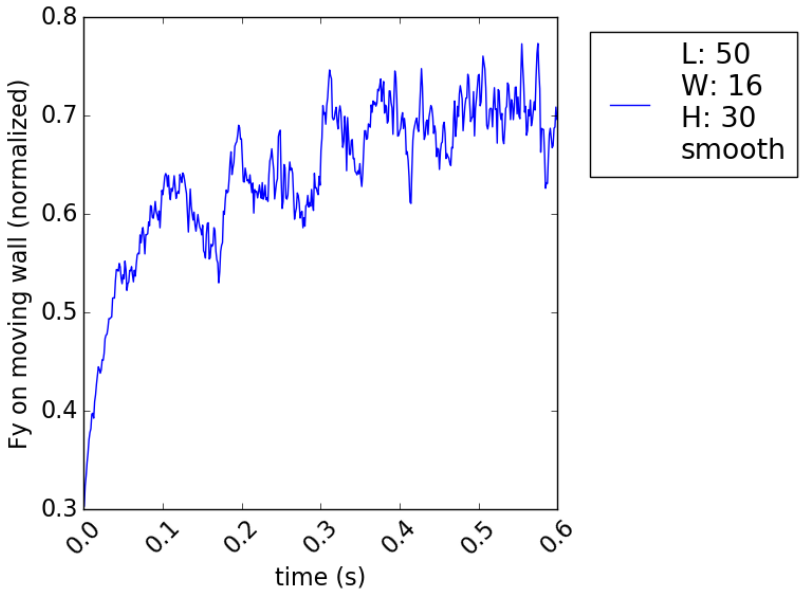

(a) hooke normal force on shearing

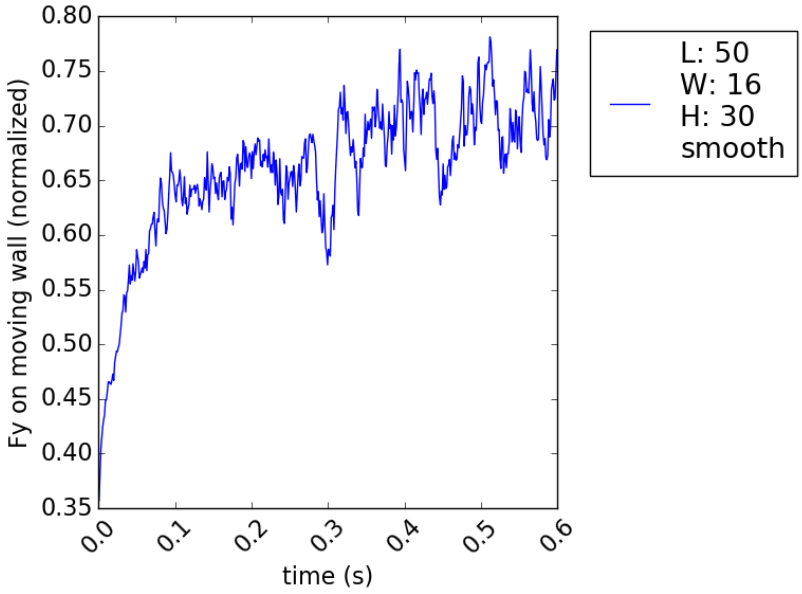

(b) hertz normal force on shearing

Figure 3.2: Normal force on shearing plane for Hooke and Hertz Model

Chapter 4

SIMULATION RESULT

4.1 Introduction

The observed alterations encompass stress, solid fraction, and velocity variations, which are challenging to discern experimentally. Consequently, simulations were employed to investigate these changes beneath the top surface of the bed. Our study presents the findings of stress and velocity alterations in diverse box sizes and various wall velocities.

4.2 Transient Velocity and Solid Fraction

Figure 4.1 presents the depth-averaged of azimuthal velocity as a function of strain rate and lateral position, y. The depth-averaged of azimuthal velocity reaches a maximum at strain, $\gamma = 0.010$. For strain from $\gamma = 0.010$ to $\gamma = 0.246$, the magnitude of the velocity decreases before reaching a steady state. At steady state, the slip velocity is approximately 37% the wall velocity.

As shown in fig 4.2, the azimuthal velocity at the free surface shows an exponential decay from the shearing wall to $y = 7d_p$ from the shearing wall. For $y = 7d_p$ to the static wall, the decay rate is lower.

Figures 4.3 and 4.4 show the solid fraction when the shearing begins and is in a steady state. As found in these figures, within one particle diameter of the moving and stationary wall, the solid fraction is approximately 0.4, increasing to an average of 0.6 in the center. Figure 4.5 show the average solid fraction increases from approximately 0.590 at $\gamma = 0$ to 0.60 at $\gamma = 5$ from the bottom to the height $22d_p$ as a function of strain. The value of the solid fraction increases in most locations in the computational cell but decreases in the region near the shearing wall.

4.3 Vortex flow

Fig. 4.6 displays streamlines illustrating particle motion at three distinct strain rates. Upon the initiation of shearing, the grains near the shearing wall begin to descend, resulting in a secondary flow developing across the y-z plane. The velocity scale of this flow is small compared to the azimuthal flow observed in Fig. 4.1. By the time $\gamma = 2.46$, the streamlines reveal the emergence of a single vortex, with its center

moving progressively closer to the wall.

Fig. 4.7 demonstrates the evolution of the free surface inclination over time. The height of the free surface nearest to the shearing wall decreases, reaching a steady state at approximately $\gamma = 15$. Figs. 4.8 and 4.9 depict the variations in the velocity towards the wall (V_y) on the top surface and at $3d_p$ beneath the top. The value of V_y diminishes from the shearing wall to the static wall. Fig. 4.10 presents V_y and V_z at different heights, revealing that $\partial v_z/\partial y < 0$ at the static wall and $\partial v_z/\partial y > 0$ at the shearing wall (with the z-axis pointing up). Furthermore, no vortex appears when gravity is disabled and a top wall is added to confine the particles, suggesting that gravity and the free surface are key factors in the emergence of vortex flow.

4.4 Wall stress anomaly

Figures 4.11 and 4.12 show the normal and tangential vertical stresses at both the stationary and moving walls as a function of height. The variation is hydrostatic since the depth is not much larger than the distance between the shearing wall and the static wall. After the shearing starts, the vertical shear stress, σ_{yz}, changes sign on both the shearing wall and the static wall. This shear stress variation is similar to the result found by Gutam, Mehandia, and Nott (2013).

We conclude that the vortex flow explains the anomalous stress on the walls. As found in Fig 4.10b, $\partial v_z/\partial y < 0$ at the static wall and $\partial v_z/\partial y > 0$ at the shearing wall. Consider the simplest plasticity model (Srivastava and Sundaresan, 2003; Nott, 2009),

$$\boldsymbol{\sigma} = p_{\mathrm{c}}(\phi)\,(1 - \mu_{\mathrm{b}}\nabla \cdot \mathbf{v}/\dot{\gamma})^{\mathrm{m}}\,\boldsymbol{\delta} - 2\mu_{\mathrm{s}}p_{\mathrm{c}}(\phi)\mathbf{D}/\dot{\gamma} \tag{4.1}$$

where $\mathbf{v}$ is the velocity, $\mathbf{D}$ the deviatoric part of the deformation rate tensor (with scalar norm $\dot{\gamma} \equiv [2\mathbf{D} : \mathbf{D}]^{1/2}$), $\boldsymbol{\delta}$ the identity tensor, and $p_{\mathrm{c}}(\phi)$ is the pressure at the critical state. μ_b and μ_s are the bulk and shear plastic moduli, which may be independent of γ or not.

Consider the yz component for the equation (4.1)

$$\boldsymbol{\sigma_{yz}} = -2\frac{\mu_{\mathrm{s}}p_{\mathrm{c}}(\phi)}{\dot{\gamma}}\frac{\partial v_z}{\partial y}, \tag{4.2}$$

At the static wall where $\partial v_z/\partial y < 0$, we have $\sigma_{yz} > 0$. Since the normal associated with the static wall is negative, the granular material gives it downward traction. Similarly for shearing wall where $\partial v_z/\partial y > 0$, $\sigma_{yz} < 0$. Since the normal of the static wall is positive, the granular material also gives it downward traction.

In examining the steady-state equilibrium for an entire horizontal cross-section, we derive the following equation:

$$\frac{\partial}{\partial z}\int_A \sigma_{zz}\,\mathrm{d}S + \oint_\ell \sigma_{nz} d\ell = \rho g A, \tag{4.3}$$

where n represents the normal of the side wall. By integrating Equation (4.3), we obtain:

$$\frac{\mathrm{d}\left\langle\sigma_{zz}\right\rangle}{\mathrm{d}z} + \frac{L_x}{A}(\hat{\sigma}_{yz,shearing} + \hat{\sigma}_{yz,static}) = \rho g, \tag{4.4}$$

Here, L_x denotes the length along the shearing direction, and $\hat{\sigma}_{yz,shearing}$ and $\hat{\sigma}_{yz,static}$ represent the vertical shear stresses on the shearing and static walls, respectively. According to Janssen's assumption (Cowin, 1977),

$$\sigma_{yy} = K\left\langle\sigma_{zz}\right\rangle, \tag{4.5}$$

where K is the Janssen constant. Combining Equations (4.5) and (4.4) yields:

$$\frac{\mathrm{d}\sigma_{yy}}{\mathrm{d}z} + \frac{KL_x}{A}(\hat{\sigma}_{yz,shearing} + \hat{\sigma}_{yz,static}) = \rho g. \tag{4.6}$$

Consequently, the increase in σ_{yy} with shearing aligns with the sign change of the vertical shear stress $\hat{\sigma}_{yz}$ on both the shearing and static walls.

4.5 μ-I

We define the strain-rate tensor as $\dot{\gamma}_{ij} = \left(\partial v_i/\partial x_j + \partial v_j/\partial x_i\right)/2$, and the strain-rate deviator as $\dot{\gamma}'_{ij} = \dot{\gamma}_{ij} - (1/3)\left(\dot{\gamma}_{kk}\right)\delta_{ij}$, where v_i is the velocity field and x_i is the

spatial coordinate. And we define the stress deviator σ'_{ij} $\dot{\sigma}'_{ij} = \dot{\sigma}_{ij} - (1/3)\,(\dot{\sigma}_{kk})\,\delta_{ij}$. The equivalent shear stress and equivalent shear rate are defined, respectively, by $\tau = \left(\sigma'_{ij}\sigma'_{ij}/2\right)^{1/2}$ and $\dot{\gamma} = \left(2\dot{\gamma}'_{ij}\dot{\gamma}'_{ij}\right)^{1/2}$, and we define pressure $P = -\sigma_{kk}/3$. The stress ratio is defined as $\mu = \tau/P$. The inertia number is defined as $I = \dot{\gamma}\sqrt{d^2\rho_s/P}$. Figure 4.13 shows the value of inertia number at steady-state ($\gamma = 15.98$) as a function of y and z. The inertia number decreases from the shearing wall to the static wall and from the top surface to the bottom. There is a corner near the static wall and near the bottom where the inertia number is small. Figures 4.14 and 4.15 show the value of μ and I in the center of the box at different times. Both μ and I decrease to a minimum quickly and increase slowly. Figure 4.16 shows the stress ratio, μ, is almost independent of the inertia number, I in different locations of the box at the steady state where $\gamma = 15.98$. Figures 4.17, 4.18, 4.19, 4.20, 4.21, and 4.22 show the $\mu - I$ has different trend as the strain increases. The results found in these figures correspond with different locations within the box. The results shown in figures 4.19 and 4.20 are similar to what is shown in figures 4.14 and 4.15. However, the data close to the static wall shows an increase in μ between $1 < \gamma < 7$ while I decreases. The data close to the shearing wall shows a lower value of μ initially than the middle region while I is larger.

4.6 Initial transition vs later time

The stress ratio is initially greater than 0.3 and decreases to a steady state value quickly as found in prior figures. This is due to the stress being highly anisotropic when shearing begins. Figures 4.23, 4.24, and 4.25 show the diagonal component of the deviatoric stress is not zero in the beginning. The normal stress in the vertical direction σ_{33} is larger than the other components σ_{22} and σ_{11}, and the differences become smaller when it reaches a steady state. The diagonal part of the stress tensor reaches a steady value later than the volume fraction. There may be other variables that cause the stresses to change slowly in addition to the volume fraction. In the experiment, we saw similar behavior while the top surface does not change while the torque was increasing slowly.

4.7 Results of different wall velocity

Figures 4.26, 4.27, and 4.28 show the average shear stress on the moving wall at different shearing speeds that characterized by different Savage numbers 2×10^{-5}, 2×10^{-6}, and 2×10^{-7}. The time to steady state for shear stress in different wall speeds is almost the same.

Figures 4.30, 4.31, and 4.32 show the velocity from the moving wall to the static wall as time evolves in three shearing speeds same as mentioned above. Figures 4.34, 4.35, and 4.36 shows the velocity change in the same timesteps. From these figures, we see it takes a longer time for the velocity to a steady state when the wall speed is slower. Although the slip velocities on the moving wall are almost the same when reaching a steady state. The observation shows the timescale for stress change is different than the timescale for velocity change. So there are other variables that need to be taken into account when predicting the stress change.

4.8 Results of different box sizes

Figures 4.37, 4.38, 4.39, and 4.40 show the velocity distribution for different strain rates and for different heights of the bed. The velocity at steady state is similar for different box heights.

Figures 4.41, 4.42, 4.43, and 4.44 show the shearing stress on the shearing wall in different heights of boxes. The shearing stress increases in a short time in the beginning then oscillates with the average value increasing slowly. The results are similar for each of the bed heights.

Figures 4.45, 4.46, 4.47, 4.48, 4.49, 4.50, 4.51, and 4.52 show the stress ratio on the moving wall and the static wall. The stress ratio does not change over time on both walls. The stress ratio is higher on the moving wall than on the static wall. On the moving wall, the stress ratio gets smaller when the box height increases. On the static wall, the stress ratio is larger when the box height increases.

4.9 Conclusions

In our simulations, we observed that the no-slip condition does not apply and that dilatancy plays an important role, causing the wall stress anomaly. The stress is initially anisotropic when the wall starts to shear but approaches isotropy later [Fig. 4.23, 4.24, 4.25]. At steady state, the stress ratio μ is found to be relatively insensitive to the inertia number I at different locations in the box [Fig. 4.16]. We also observed the reversal of vertical shear stress at the wall and the appearance of vortex flow at the onset of shearing, and these phenomena have not been incorporated into existing models.

References

Cowin, S C (Sept. 1977). "The Theory of Static Loads in Bins". In: *J. Appl. Mech.* 44.3, pp. 409–412.

Gutam, Kamala Jyotsna, Vishwajeet Mehandia, and Prabhu R Nott (July 2013). "Rheometry of granular materials in cylindrical Couette cells: Anomalous stress caused by gravity and shear". In: *Phys. Fluids* 25.7, p. 070602.

Nott, Prabhu R (June 2009). "Classical and Cosserat plasticity and viscoplasticity models for slow granular flow". In: *Acta Mech.* 205.1, pp. 151–160.

Srivastava, Anuj and Sankaran Sundaresan (Jan. 2003). "Analysis of a frictional–kinetic model for gas–particle flow". In: *Powder Technol.* 129.1, pp. 72–85.

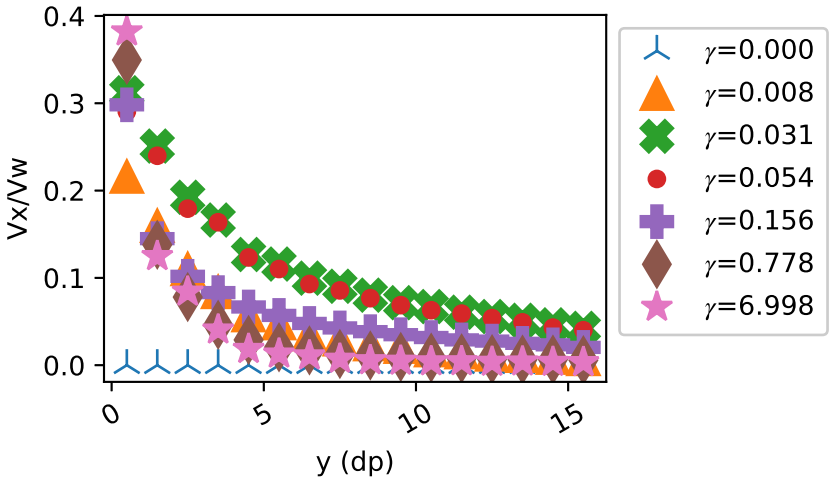

Figure 4.1: Depth-averaged of azimuthal velocity at different strain

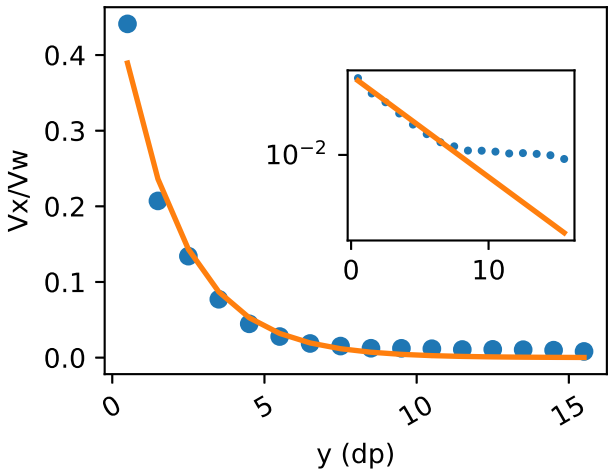

Figure 4.2: Surface velocity in steady state ($\gamma = 7.376$) in both linear and log (inset) scale

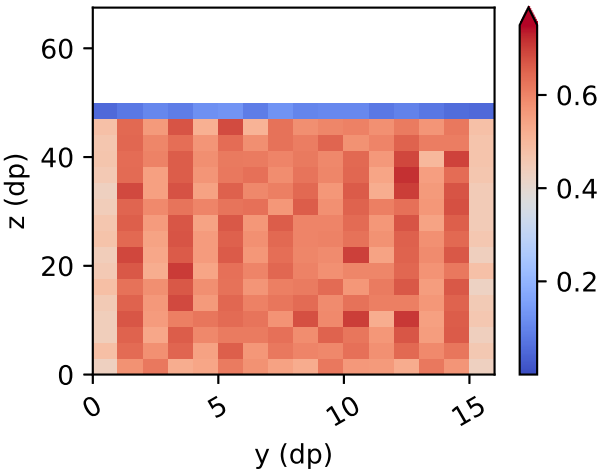

Figure 4.3: Solid fraction at $\gamma = 0$

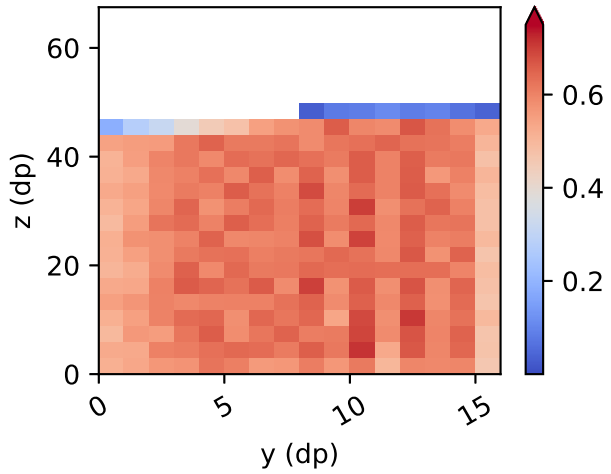

Figure 4.4: Solid fraction at steady state ($\gamma = 7.38$)

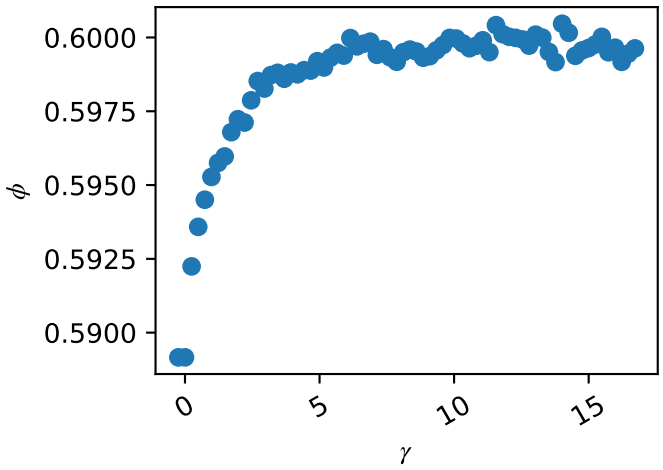

Figure 4.5: Solid fraction averaged from bottom to 22 d_p height

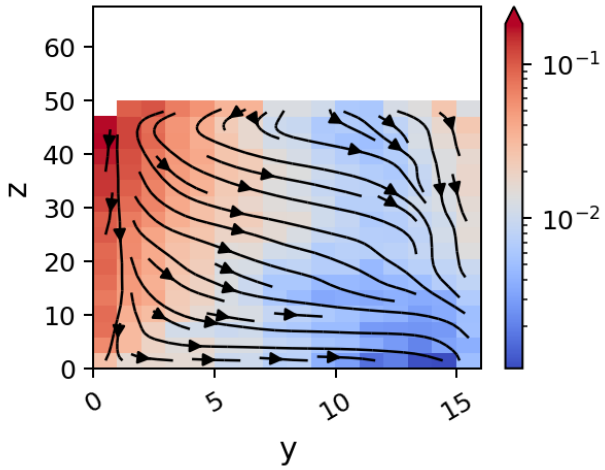

(a)

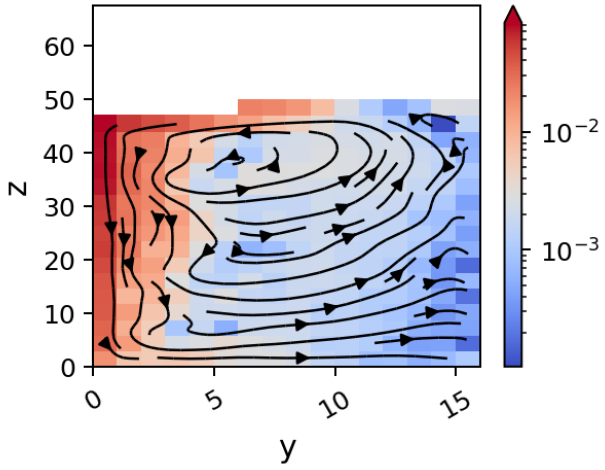

(b)

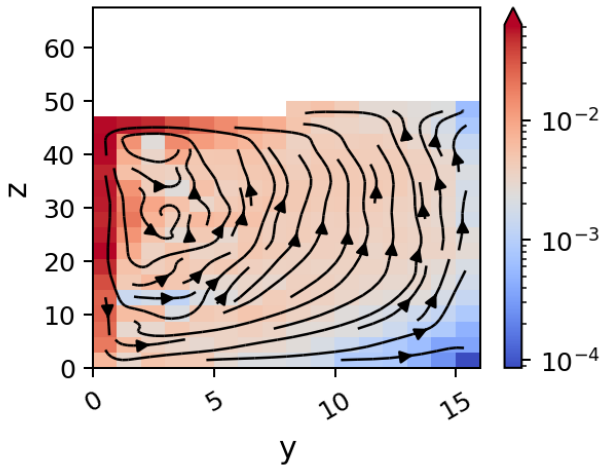

(c)

Figure 4.6: Vortex flow when $\gamma = 0.246$ (a), 2.46 (b), 7.38 (c). The magnitude of velocity is scaled by the wall velocity.

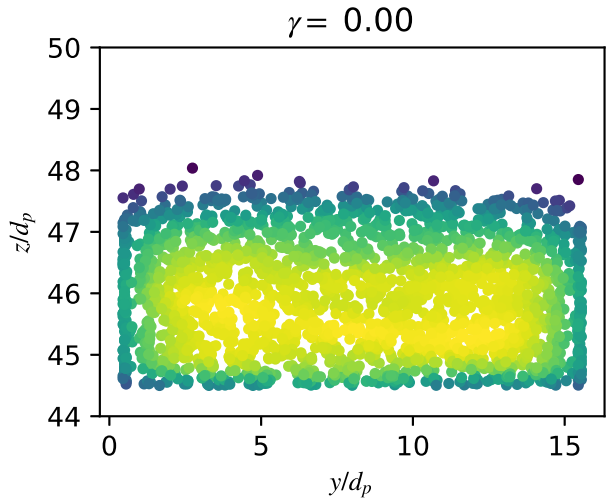

(a)

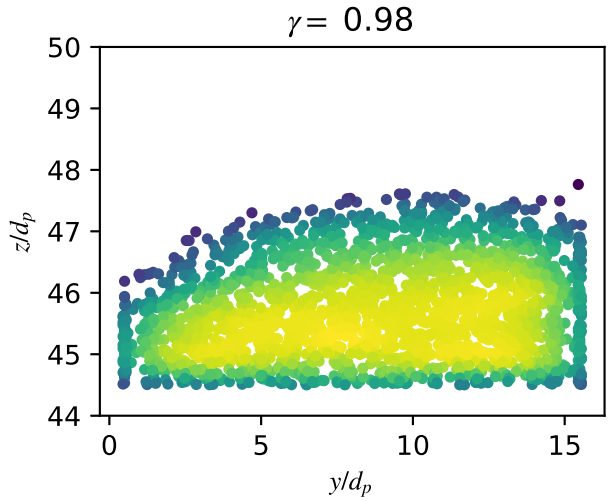

(b)

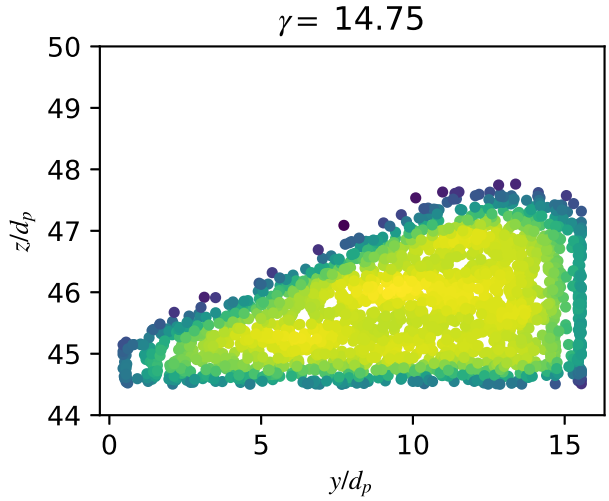

(c)

Figure 4.7: Free surface when γ = 0 (a), 0.98 (b), 14.75 (c). The color-coded dots in the figure represent density, with navy blue indicating the lowest values and light yellow indicating the highest.

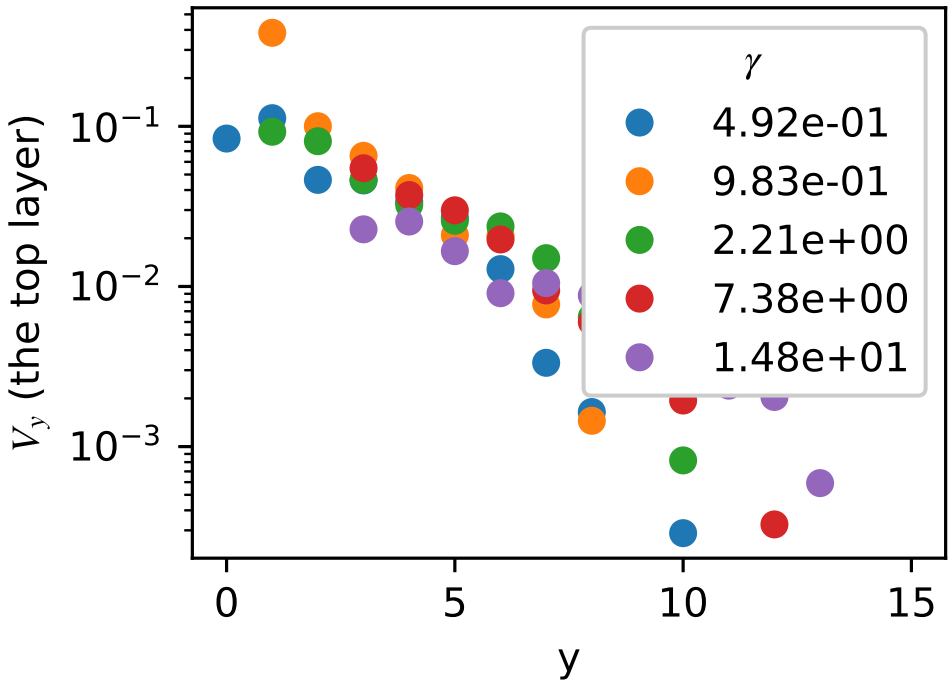

Figure 4.8: Surface velocity toward the shearing wall at the top of the bed at different values of γ. The magnitude of velocity is scaled by the wall velocity.

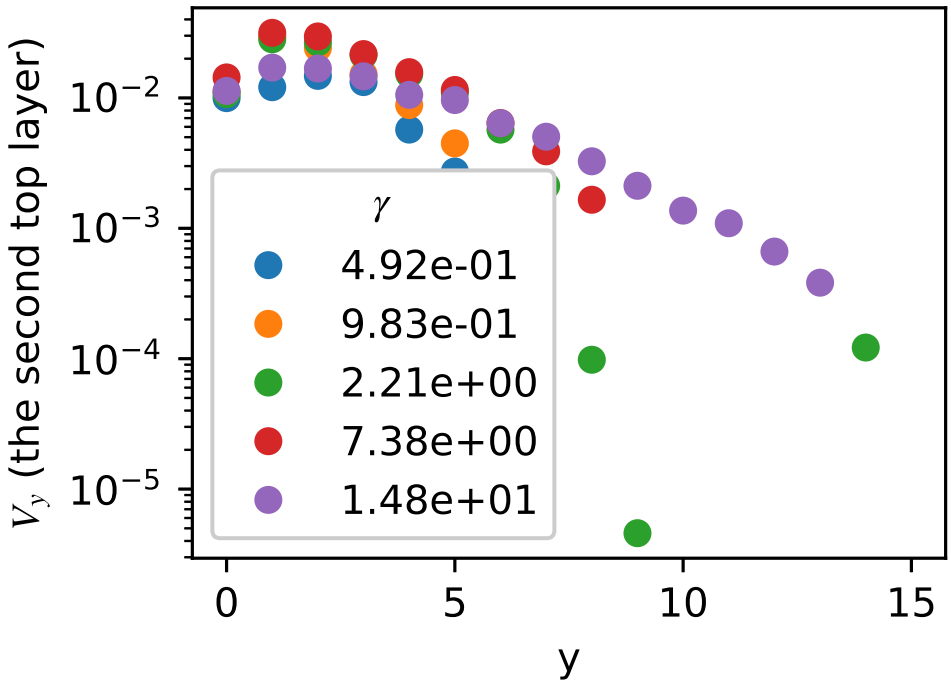

Figure 4.9: Velocity toward the shearing wall at the height 3 d_p under the surface at different values of γ. The magnitude of velocity is scaled by the wall velocity.

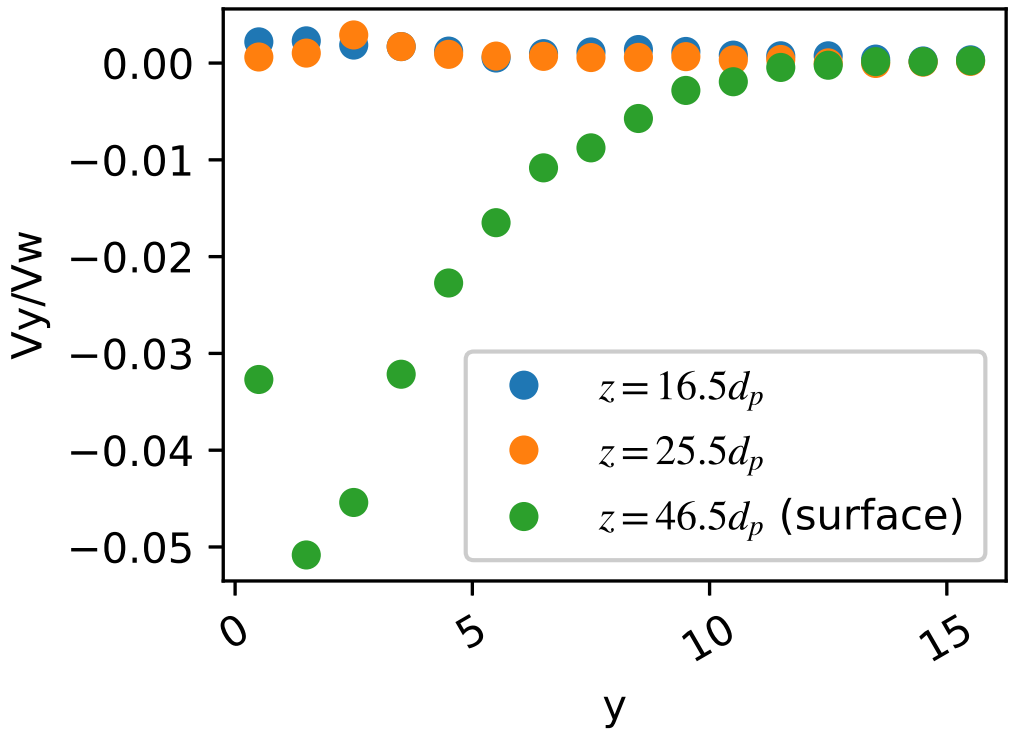

(a)

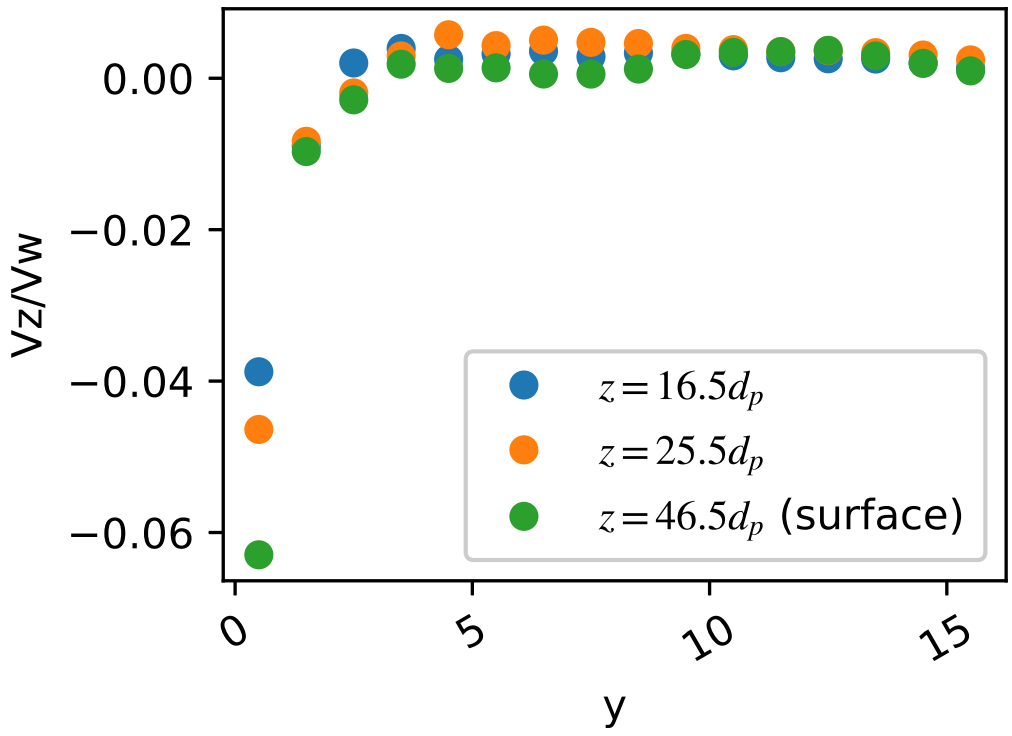

(b)

Figure 4.10: The velocities in the normal and vertical directions as a function of y at different heights for $\gamma = 0.98$.

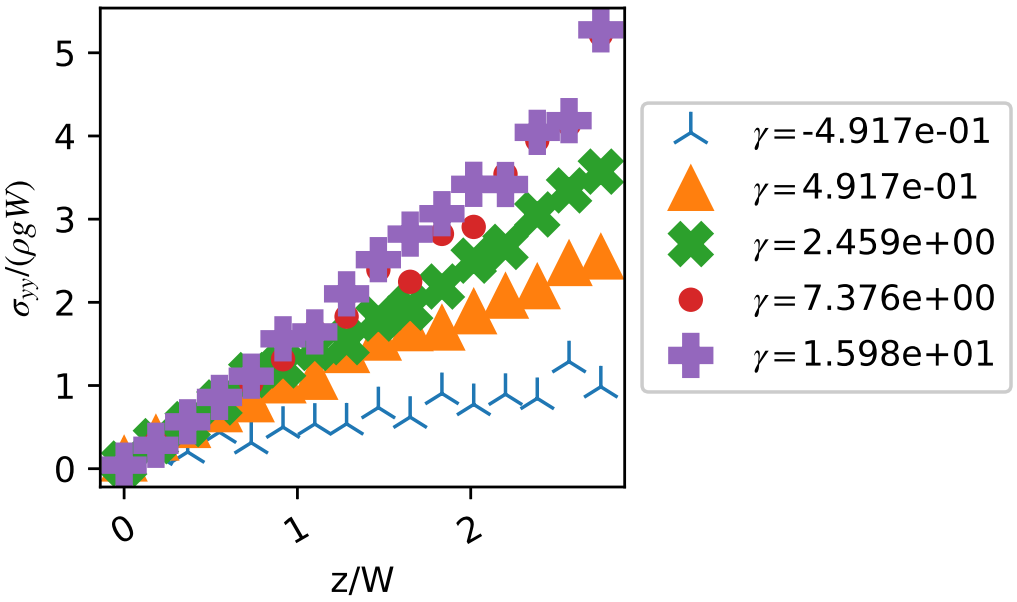

(a)

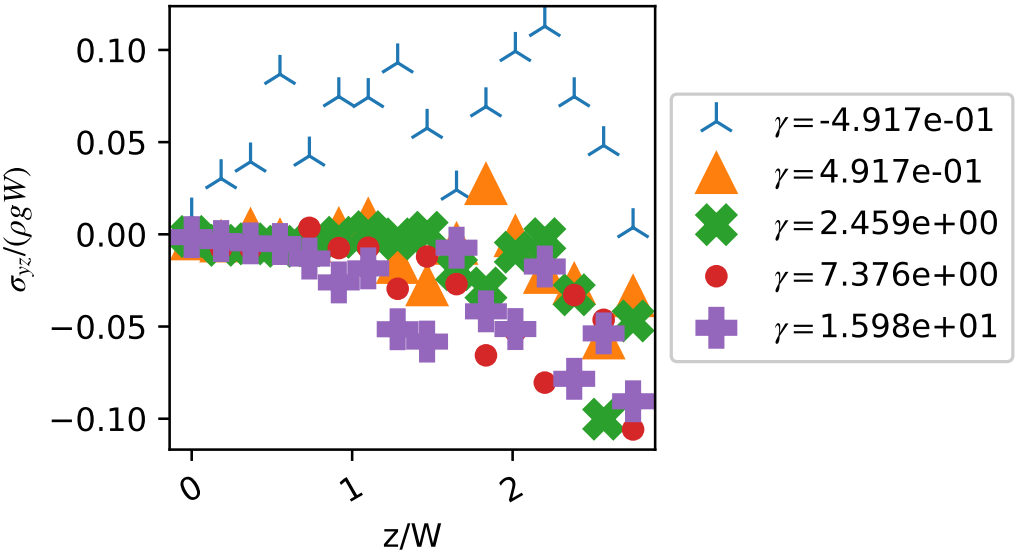

(b)

Figure 4.11: Wall stresses σ_{yy} (a), and σ_{yz} (b) on the shearing wall. $H = 60d_p$

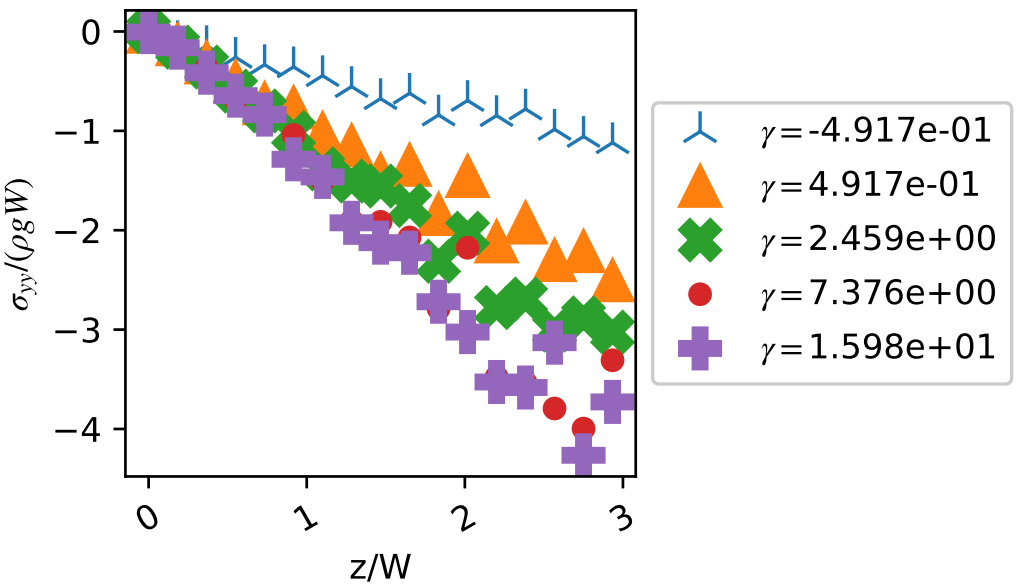

(a)

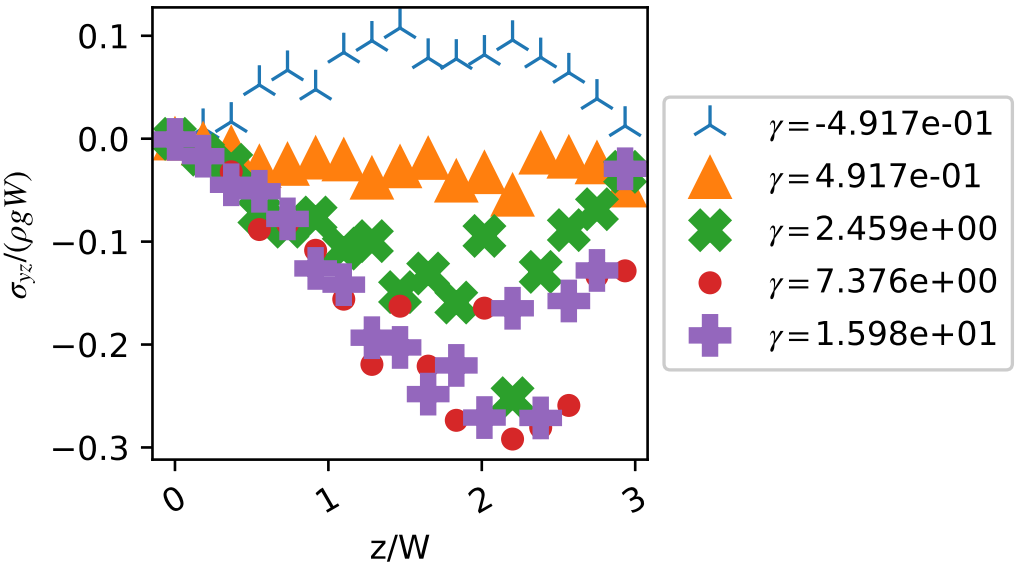

(b)

Figure 4.12: Wall stresses σ_{yy} (a), and σ_{yz} (b) on the static wall. $H = 60d_p$

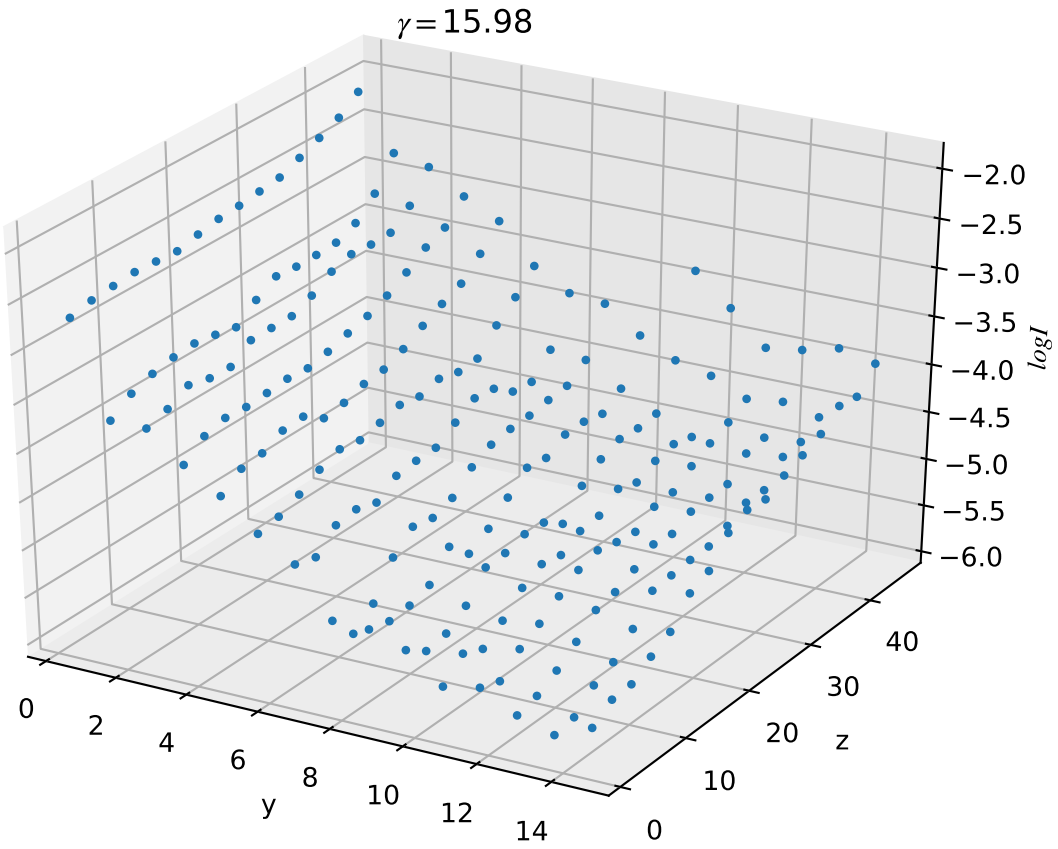

Figure 4.13: Inertia number in steady state at different locations for γ = 15.98

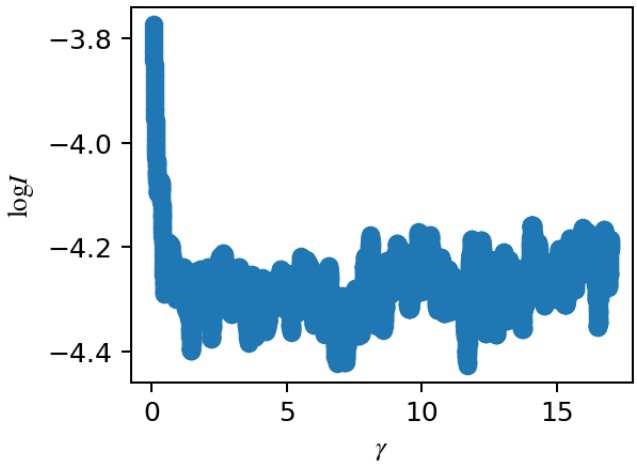

Figure 4.14: Inertia Number average over a large region in the middle of the box

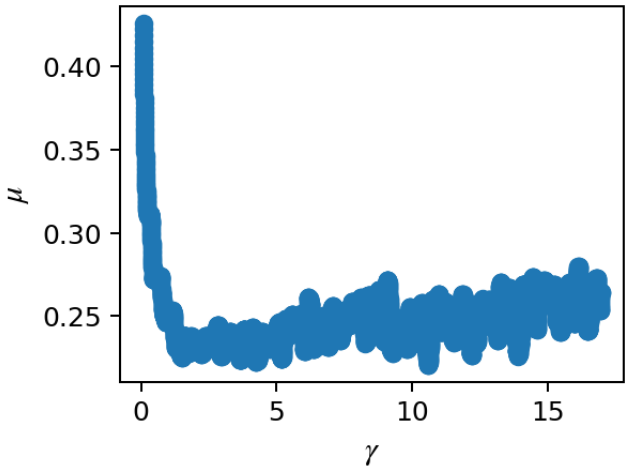

Figure 4.15: Stress ratio average over a large region in the middle of the box

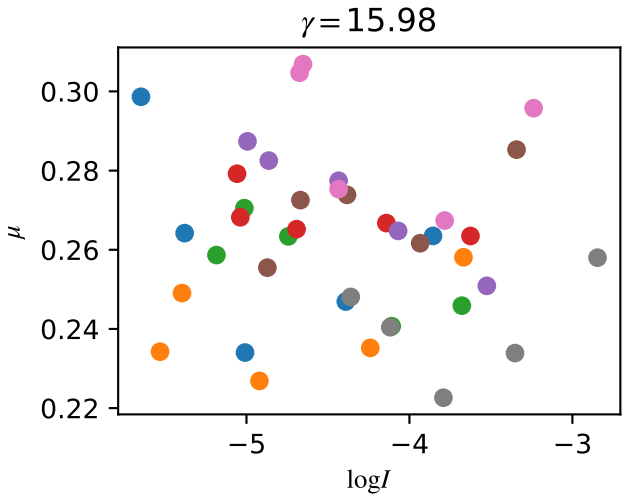

Figure 4.16: μ-I at different location. Each color represents the data in the same height z for different values of y from $2d_p$ to $12d_p$. Blue dots are height $z = 1.5d_p$. Orange dots are height $z = 7.5d_p$. Green dots are height $z = 13.5d_p$. Red dots are height $z = 19.5d_p$. Purple dots are height $z = 25.5d_p$. Brown dots are height $z = 31.5d_p$. Pink dots are height $z = 37.5d_p$. Grey dots are height $z = 43.5d_p$.

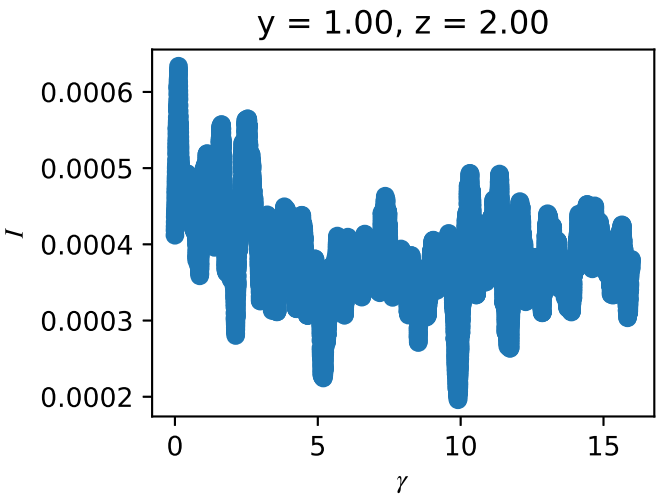

Figure 4.17: Inertia Number near the shearing wall

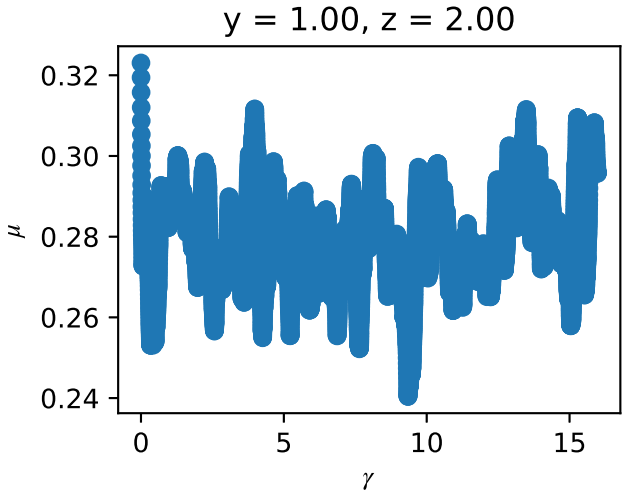

Figure 4.18: Stress ratio near the shearing wall

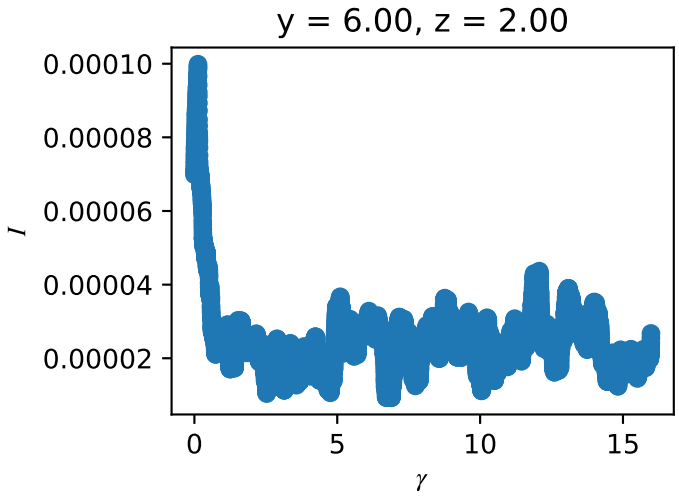

Figure 4.19: Inertia Number in the middle of the box

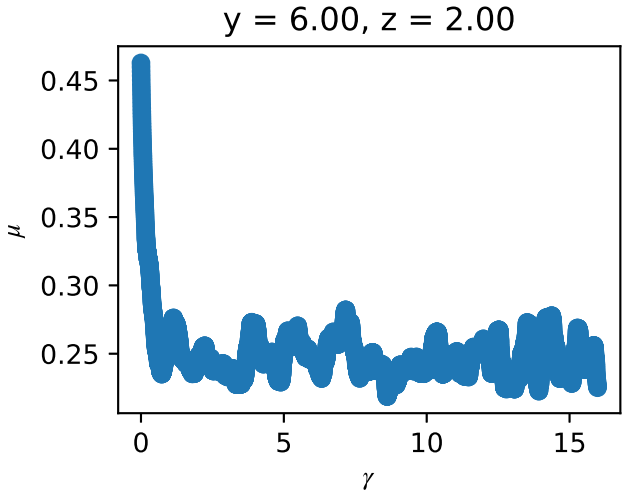

Figure 4.20: Stress ratio in the middle of the box

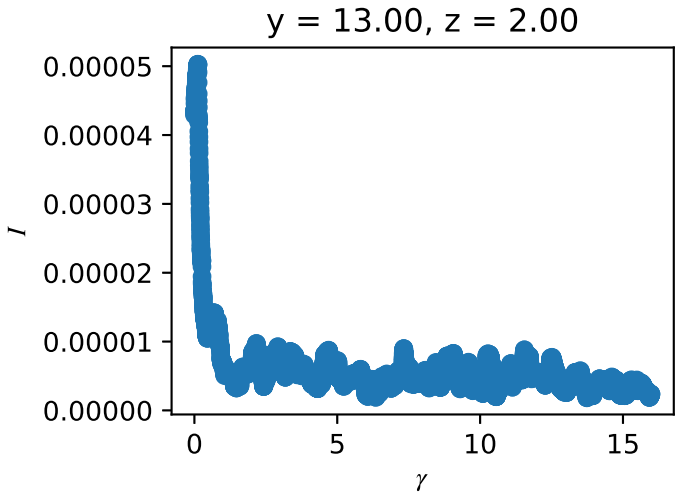

Figure 4.21: Inertia Number near the static wall

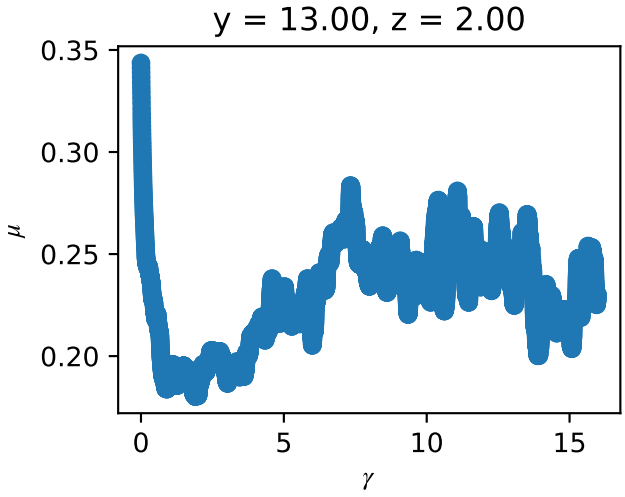

Figure 4.22: Stress ratio near the static wall

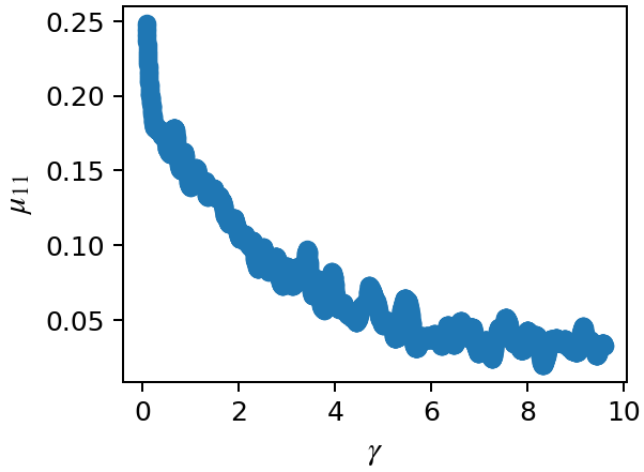

Figure 4.23: σ_{11}/P at middle of the box.

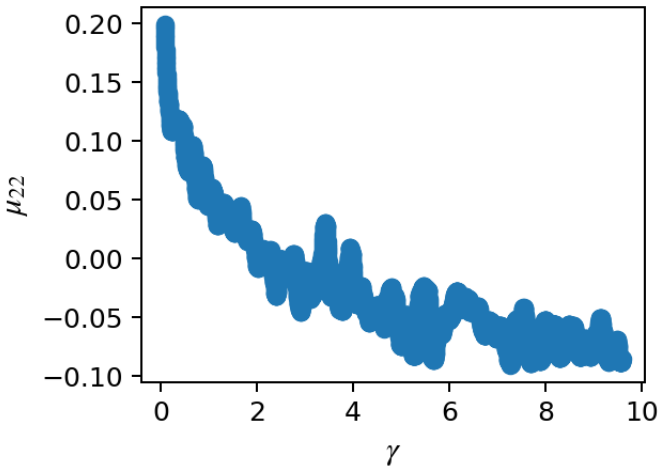

Figure 4.24: σ_{22}/P at middle of the box.

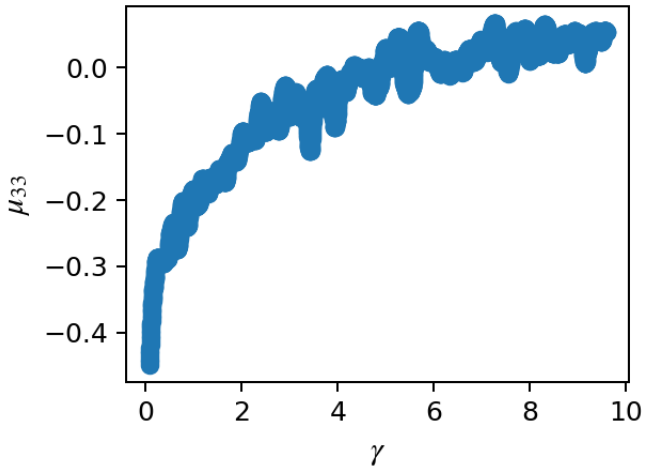

Figure 4.25: σ_{33}/P at middle of the box.

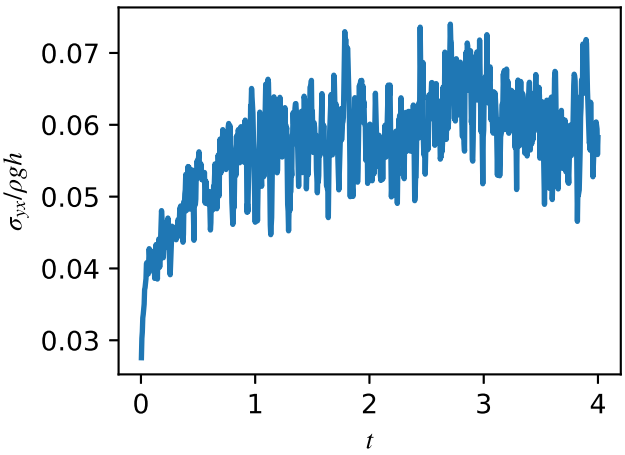

Figure 4.26: Shearing wall stress for $Sa = 2 \times 10^{-5}$

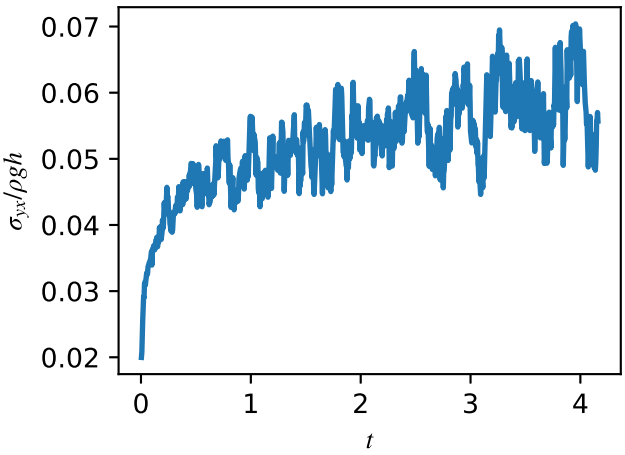

Figure 4.27: Shearing wall stress for $Sa = 2 \times 10^{-6}$

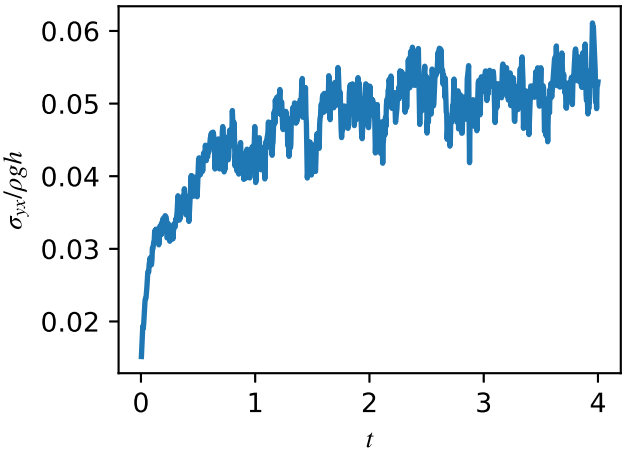

Figure 4.28: Shearing wall stress for $Sa = 2 \times 10^{-7}$

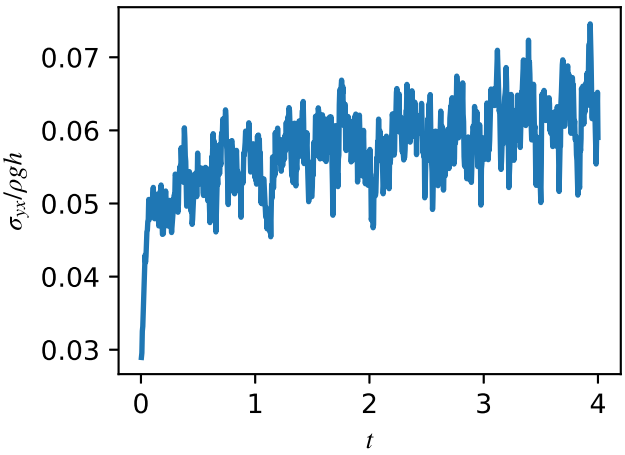

Figure 4.29: Shearing wall stress for $Sa = 2 \times 10^{-6}$ with double width.

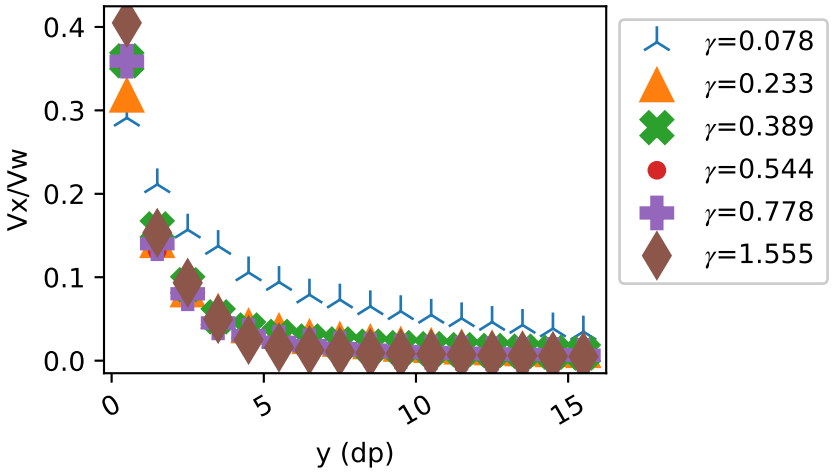

Figure 4.30: Average velocity at different strain for $Sa = 2 \times 10^{-5}$

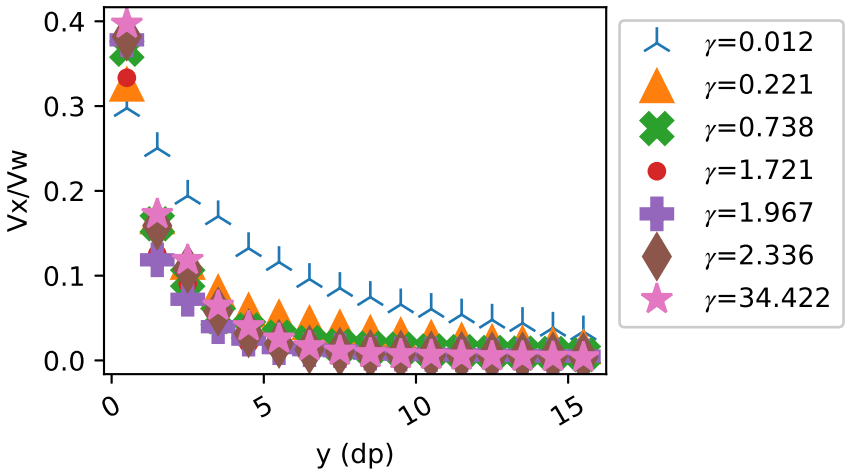

Figure 4.31: Average velocity at different strain for $Sa = 2 \times 10^{-6}$

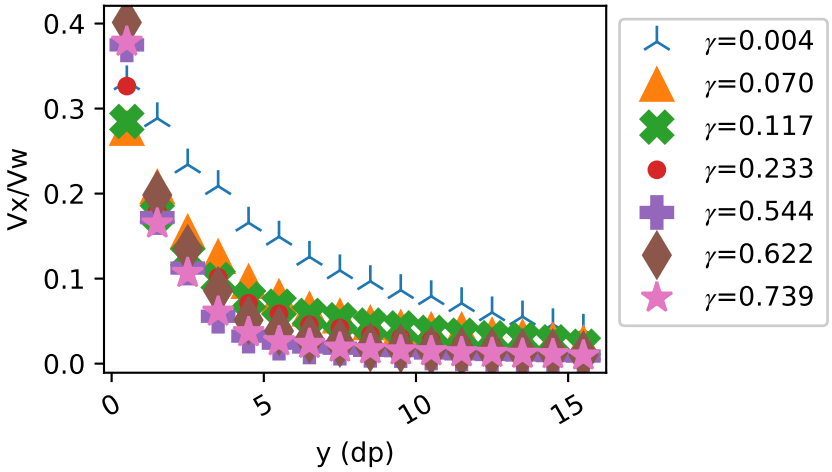

Figure 4.32: Average velocity at different strain for $Sa = 2 \times 10^{-7}$

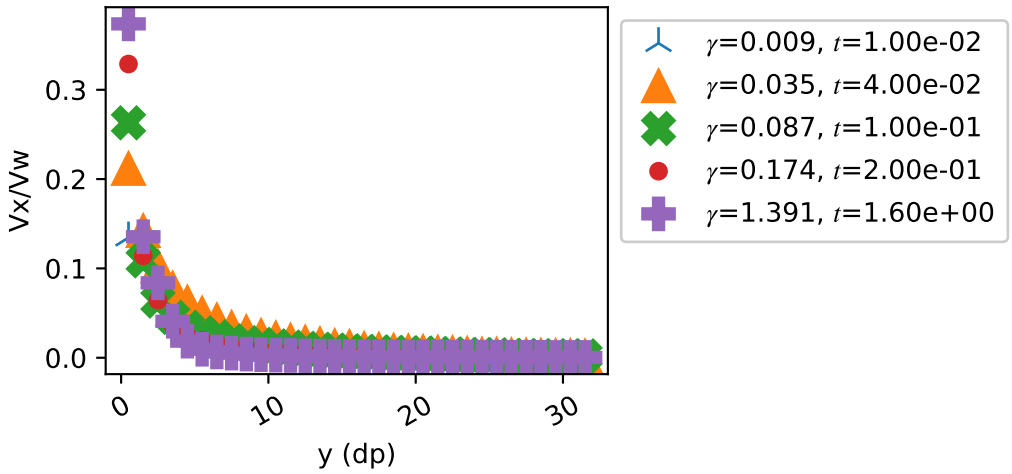

Figure 4.33: Average velocity at different strain for $Sa = 2 \times 10^{-6}$ for double width box.

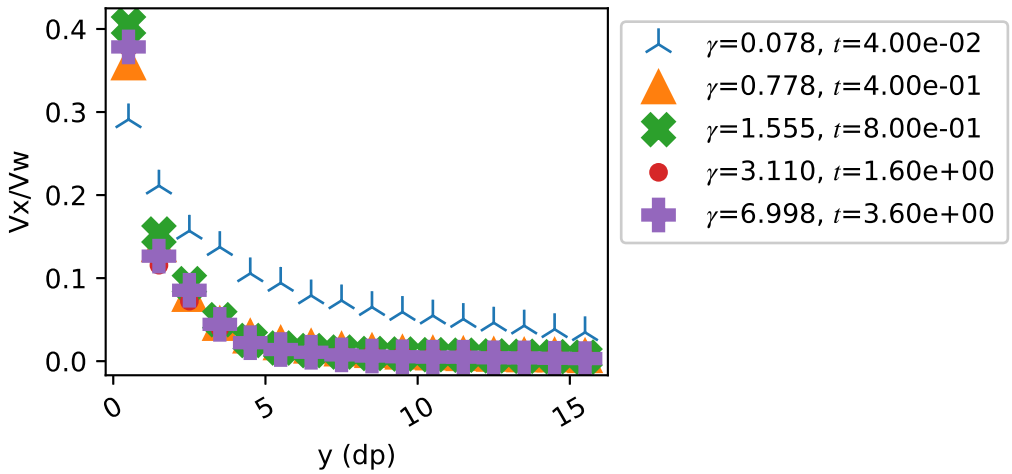

Figure 4.34: Average velocity at different strain for $Sa = 2 \times 10^{-5}$

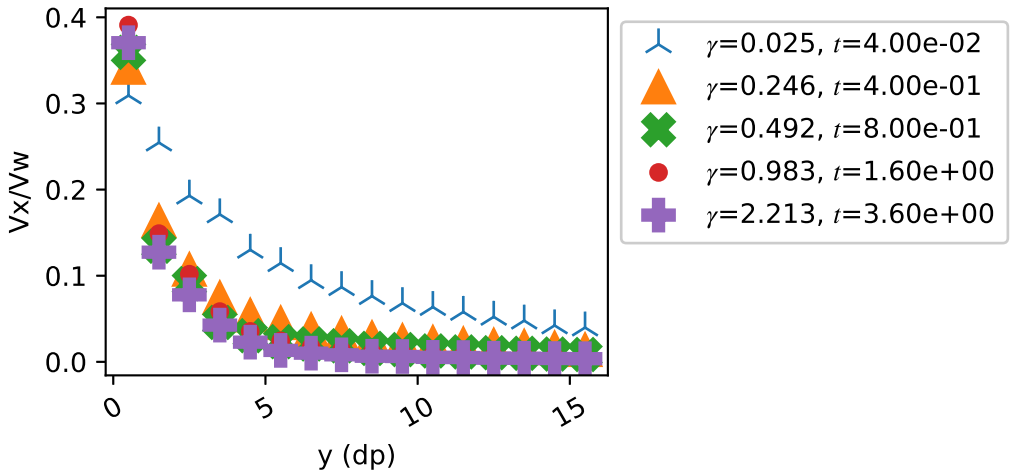

Figure 4.35: Average velocity at different strain for $Sa = 2 \times 10^{-6}$

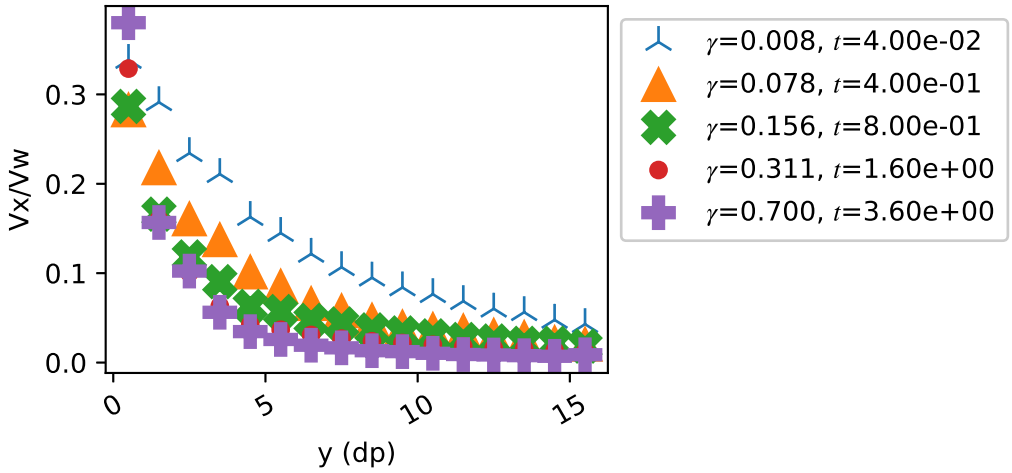

Figure 4.36: Average velocity at different strain for $Sa = 2 \times 10^{-7}$

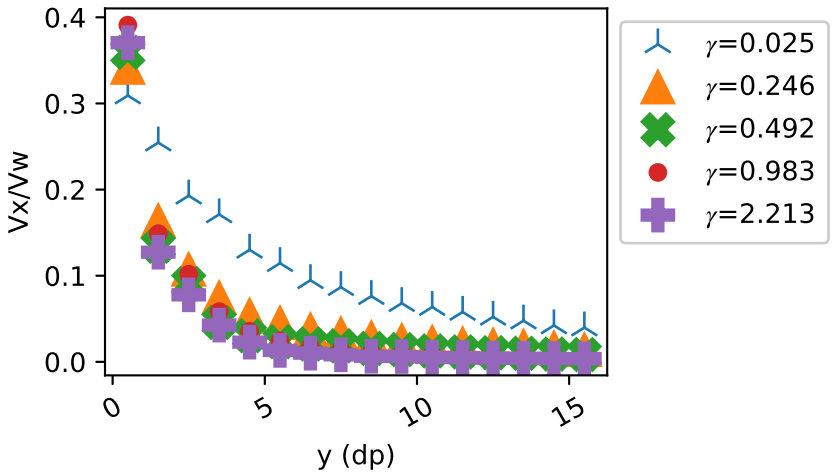

Figure 4.37: Velocity averaged over full depth of the bed at different strain for $H = 30d_p$

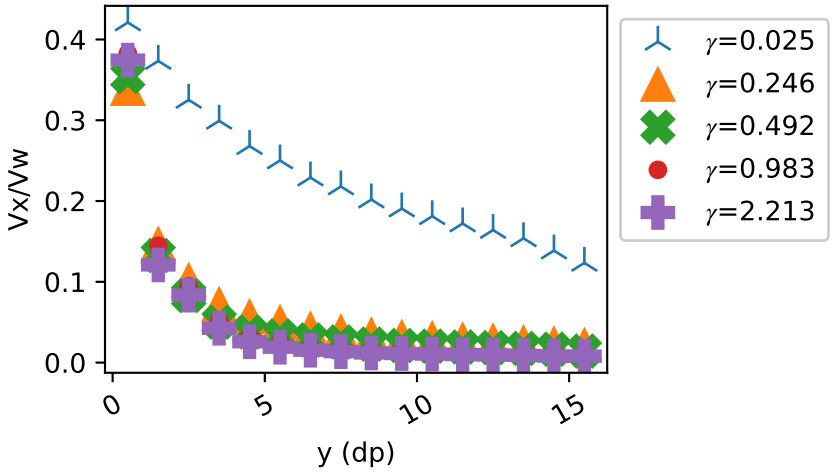

Figure 4.38: Velocity averaged over full depth of the bed at different strain for $H = 60d_p$

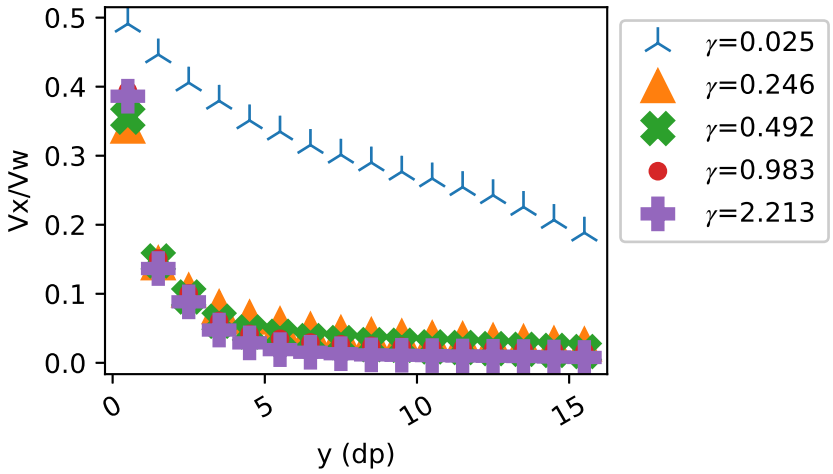

Figure 4.39: Velocity averaged over full depth of the bed at different strain for $H = 90d_p$

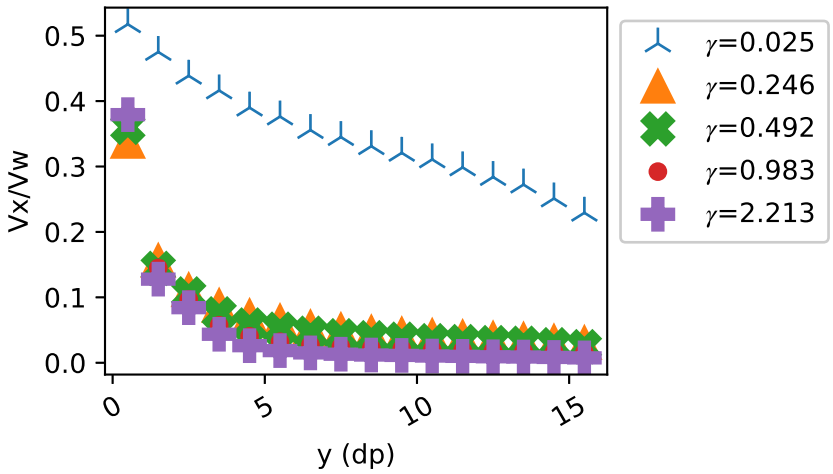

Figure 4.40: Velocity averaged over full depth of the bed at different strain for $H = 120d_p$

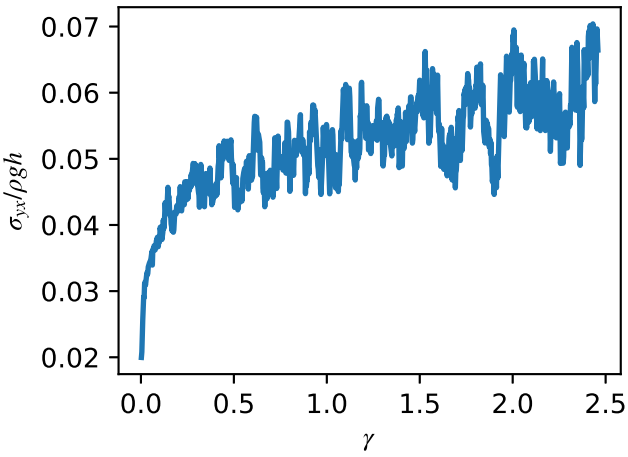

Figure 4.41: Shearing wall stress for $H = 30d_p$

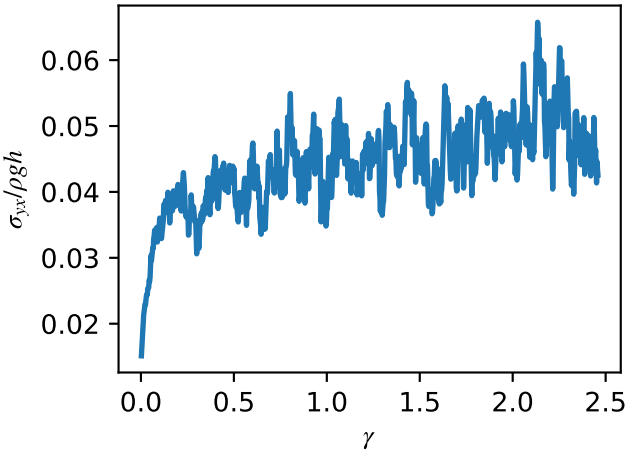

Figure 4.42: Shearing wall stress for $H = 60d_p$

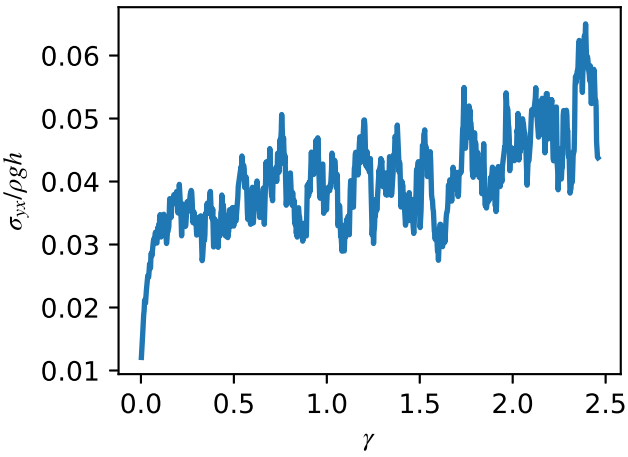

Figure 4.43: Shearing wall stress for $H = 90d_p$

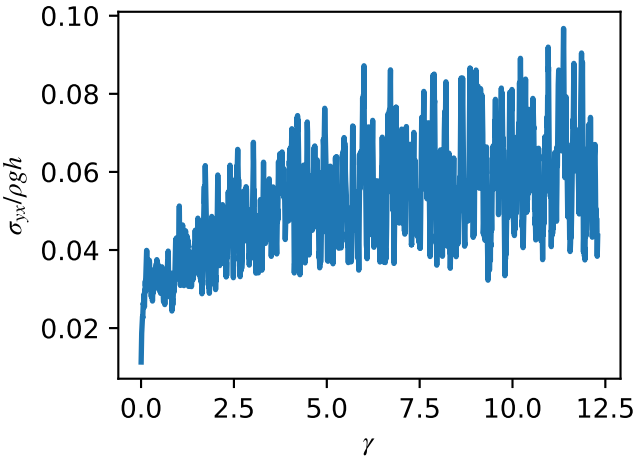

Figure 4.44: Shearing wall stress for $H = 120d_p$

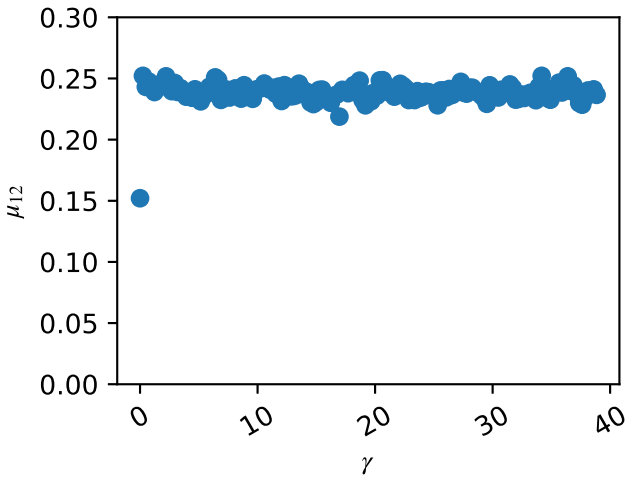

Figure 4.45: Shearing wall stress ratio for $H = 30d_p$

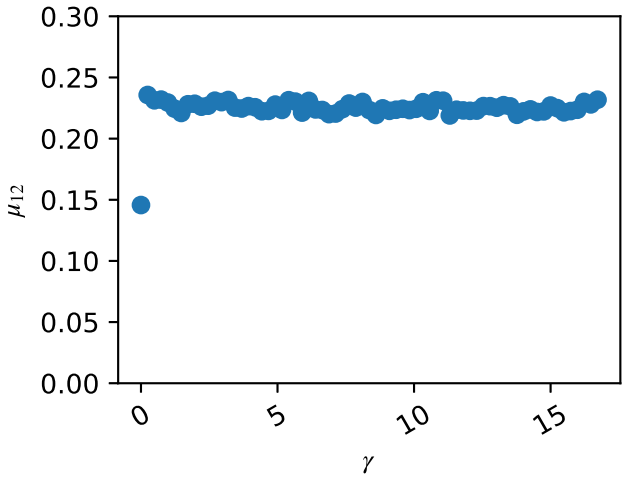

Figure 4.46: Shearing wall stress ratio for $H = 60d_p$

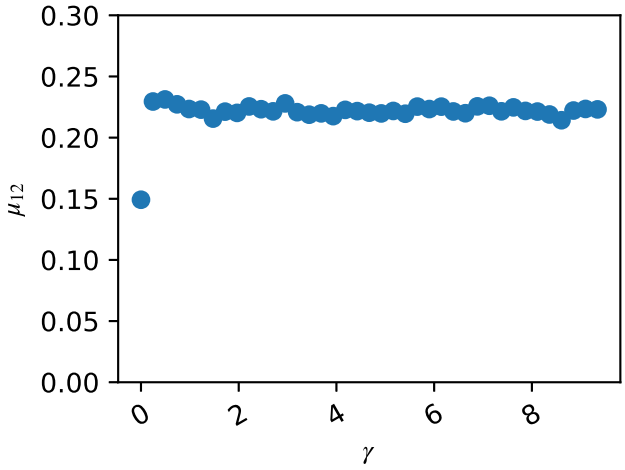

Figure 4.47: Shearing wall stress ratio for $H = 90d_p$

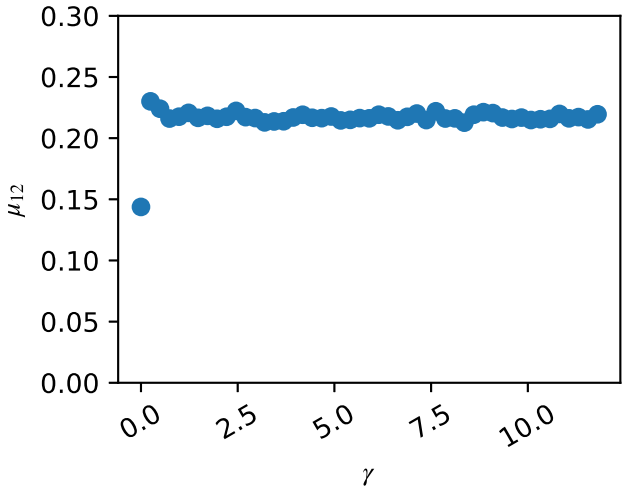

Figure 4.48: Shearing wall stress ratio for $H = 120d_p$

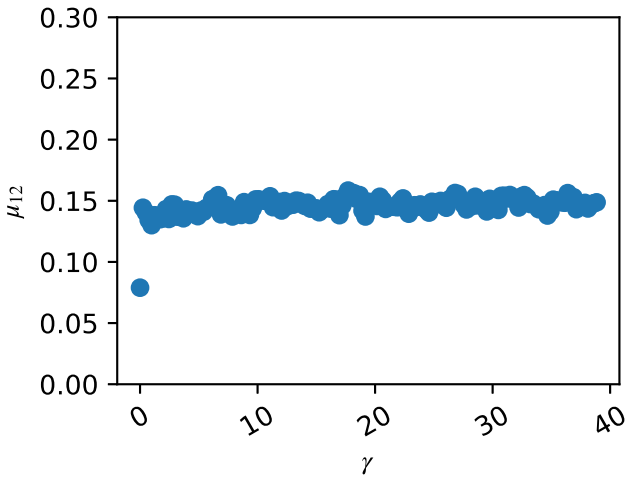

Figure 4.49: Static wall stress ratio for $H = 30d_p$

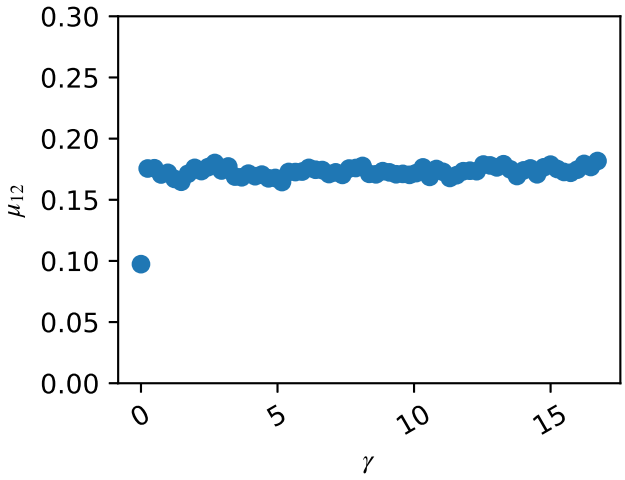

Figure 4.50: Static wall stress ratio for $H = 60d_p$

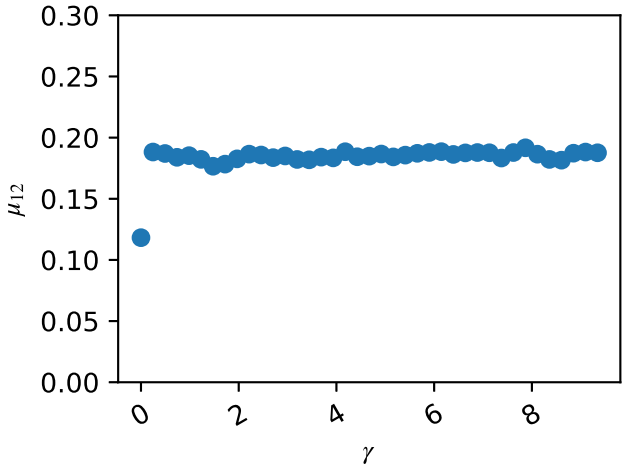

Figure 4.51: Static wall stress ratio for $H = 90d_p$

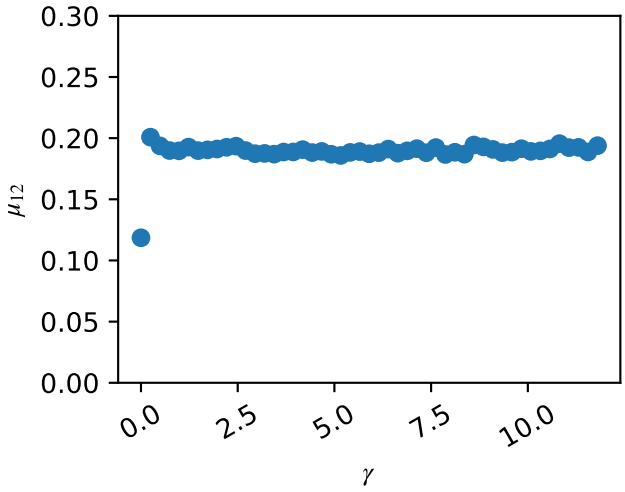

Figure 4.52: Static wall stress ratio for $H = 120d_p$

Chapter 5

THEORETICAL MODEL

5.1 Theoretical Model

In order to explain the abnormal wall stress and the downward velocity that we discovered in simulations, we first consider an infinite box with one shearing vertical wall. We also use the Boussinesq approximation to simplify equations by assuming constant density, except for the buoyancy term. The governing equations of the model are as follows.

The conservation of momentum is the following:

$$\rho \frac{D\vec{u}}{Dt} = \vec{\nabla} \cdot \boldsymbol{\sigma} + \rho \vec{g}, \tag{5.1}$$

where $\vec{u}$ is the velocity vector, $\vec{g} = -g\hat{z}$, ρ is the density, which is the product of volume fraction ϕ and the particle density ρ_p.

The conservation of mass is the following:

$$\frac{\partial \rho}{\partial t} + \vec{\nabla} \cdot (\rho \vec{u}) = 0. \tag{5.2}$$

We use the non-local equations for the stress tensor, $\boldsymbol{\sigma}$, and the pressure, p, as in Dsouza and Nott, 2020:

$$\boldsymbol{\sigma} = -p\boldsymbol{\delta} + \frac{2\mu}{\dot{r}} \left(p_c \boldsymbol{D'} - l^2 \Pi(\phi) \nabla^2 \boldsymbol{D'} \right), \tag{5.3}$$

$$p_c = \Pi(\phi) - l^2 \frac{d\Pi}{d\phi} \nabla^2 \phi, \tag{5.4}$$

$$p = p_c \left(1 - \frac{\mu_b}{\dot{\gamma}} \vec{\nabla} \cdot \vec{u} \right) + l^2 \Pi(\phi) \frac{\mu_b}{\dot{\gamma}} \nabla^2 \vec{\nabla} \cdot \vec{u}, \tag{5.5}$$

where p_c is the pressure at the critical state, l is the non-local length, $\boldsymbol{D'}$ is the deviatoric deformation rate, and the shear rate is $\dot{\gamma} \equiv (2\boldsymbol{D'} : \boldsymbol{D'})^{1/2}$.

We assume x-axis translational symmetry

$$\partial_x = 0, \tag{5.6}$$

and a steady state

$$\partial_t = 0. \tag{5.7}$$

We suppose some components of strain-rate tensor can be ignored near the shearing wall:

$$\partial_y u_x \gg \partial_y u_z \gg \partial_i u_j, (i, j) \neq (y, x) \text{ or } (y, z). \tag{5.8}$$

From equations (5.5) and (5.8), we have

$$p = p_c. \tag{5.9}$$

Looking at the diagonal terms of equation (5.3) and replacing p with p_c, we obtain

$$\sigma_{yy} = \sigma_{zz} = -p_c. \tag{5.10}$$

Using equations (5.3) and (5.8), we have

$$\sigma_{yx} = \frac{2\mu}{|\partial_y u_x|}\left(p_c \partial_y u_x - l^2 \Pi \partial_y^3 u_x\right), \tag{5.11}$$

$$\sigma_{zx} = 0, \tag{5.12}$$

and

$$\sigma_{yz} = \frac{2\mu}{|\partial_y u_x|}\left(p_c \partial_y u_z - l^2 \Pi \partial_y^3 u_z\right). \tag{5.13}$$

For the z component of equation (5.1) and using the approximation of equations (5.6), (5.7), and (5.8), we have

$$\rho_p \phi u_y \partial_y u_z = \partial_y \sigma_{yz} + \partial_z \sigma_{zz} - \rho_p \phi g. \tag{5.14}$$

In the following discussion, we are going to neglect the convective terms since we focus on the case of small Savage number.

We assume when y approach to infinity, all the variables are constant

$$\partial_y \to 0, \text{ as } y \to \infty. \tag{5.15}$$

So equation (5.14) is simplified as

$$\partial_z \sigma_{zz} - \rho_p \phi_\infty g = 0 \tag{5.16}$$

as we consider the location far from the shearing wall.

Taking $\sigma_{zz} = -p_c$ in equation (5.16), the equation becomes

$$\partial_z p_c = -\rho_p \phi_\infty g, \text{ as } y \to \infty. \tag{5.17}$$

From equations (5.10), (5.14), and (5.17), we obtain the relation between stress σ_{yz} and the volume fraction in the region close to the shearing wall,

$$\partial_y \sigma_{yz} - \rho_p \left(\phi - \phi_\infty\right) g = 0. \tag{5.18}$$

Equation 5.18 demonstrates that the variation in the body force term, incorporating the volume fraction, is counterbalanced by the term $\partial_y \sigma_{yz}$, leading to a negative value for $\partial_y \sigma_{yz}$. As a result, if we assume that the value of σ_{yz} is either zero or greater than a small negative value at infinity, σ_{yz} displays a positive value near the shearing wall. Referring to equation 5.13, we can deduce that $p_c \partial_y u_z - l^2 \Pi \partial_{yyy} u_z$ is positive. By disregarding the third-derivative term $l^2 \Pi \partial_{yyy} u_z$ and assuming u_z is zero at infinity, u_z must be negative at finite y, indicating a downward direction. While the actual scenario is more complex than our assumption, this analysis provides an intuitive understanding of the direction of vertical velocity.

Replacing σ_{yz} in equation (5.18) by equation (5.13), we have

$$\partial_y \left[\frac{2\mu}{|\partial_y u_x|} \left(p_c \partial_y u_z - l^2 \Pi \partial_{yyy} u_z \right) \right] - \rho_p g \left(\phi - \phi_\infty\right) = 0. \tag{5.19}$$

To evaluate p_c in equation (5.4), we assume the variation of volume fraction ϕ does influence the body force term of equation (5.18), while the variation of ϕ is not considered in the stress expressions of equations (5.11) and (5.13). This simplification is similar to the Boussinesq approximation used in natural convection studies involving pure fluids in which the density variation is included in the body

force term but not in the variation of properties. This ignores density differences except where they appear in terms multiplied by g. We use the following assumptions that neglect the variation in ϕ in determining p_c to simplify equations (5.11) and (5.13):

$$\partial_{yy}\phi \gg \partial_{zz}\phi, \tag{5.20a}$$

$$\text{or even simpler, } \partial_{yy}\phi = \partial_{zz}\phi = 0. \tag{5.20b}$$

Then the Laplacian in equation (5.4) can be replaced by equations (5.20a) or (5.20b). Now we have

$$p_c = \Pi - l^2 \frac{d\Pi}{d\phi}\partial_{yy}\phi, \tag{5.21a}$$

$$\text{or } p_c = \Pi. \tag{5.21b}$$

Similarly, we can solve for u_x by assuming ϕ does not vary in the shear stress found in equations (5.11) and (5.13). Looking for x component of equation (5.1) and using equation (5.12), we have

$$\partial_y \left[\frac{2\mu}{|\partial_y u_x|} \left(p_c \partial_y u_x - l^2 \Pi \partial_{yyy} u_x \right) \right] = 0. \tag{5.22}$$

To integrate equation (5.22), we need 4 boundary conditions for u_x. We suppose the material adjacent to the shearing wall is in plastic deformation (Rao, Nott, and Sundaresan, 2008),

$$u_x - u_w = n_y K d_p \frac{du_x}{dy} \quad \text{as} \quad y = 0, \tag{5.23}$$

and the ratio of wall stress as a constant,

$$\frac{\sigma_{yx}}{\sigma_{yy}} = \mu_w \quad \text{as} \quad y = 0. \tag{5.24}$$

We also assume the material does not deform as it is far away from the shearing wall,

$$u_x = 0 \quad \text{as } y = \infty, \tag{5.25}$$

and

$$\frac{du_x}{dy} = 0 \quad \text{as} \quad y = \infty. \tag{5.26}$$

Using the boundary conditions and integration results in the following expression for u_x:

$$u_x = u_w \frac{e^{-\xi y}}{\left(1 + K d_p \xi\right)}, \tag{5.27}$$

where $\xi = (1 - \mu_w/\mu)^{1/2}/l$.

To solve for the vertical velocity u_z, we take the solution (5.27) for u_x in equation (5.19) and assume the variation of volume fraction from the wall to infinity has the form,

$$\phi - \phi_\infty = -\Delta\phi e^{-d_1 y}, \tag{5.28}$$

in the body force term in equation (5.19).

If we neglect the second term in equation (5.19), we can integrate to find u_z,

$$u_z/u_w = -f_0 \frac{e^{-\xi y}}{\left(1 + k d_p \xi\right)} \Delta\phi \rho_p g - \frac{\xi}{d_1 + \xi} \frac{1}{2\mu p_c d_1} \frac{e^{-(d_1+\xi)y}}{1 + K d_p \xi} \Delta\phi \rho_p g, \tag{5.29}$$

where f_0 is a constant of integration.

If we assume the stress at infinity is zero,

$$\sigma_{yz} = 0 \quad \text{as} \quad y = \infty, \tag{5.30}$$

we can determine the constant and find $f_0 = 0$. So the equation (5.30) becomes

$$u_z/u_w = \frac{-1}{1 + d_1/\xi} \frac{1}{2\mu p_c d_1} \frac{e^{-(d_1+\xi)y}}{1 + K d_p \xi} \Delta\phi \rho_p g. \tag{5.31}$$

To determine the variation of u_z with y, we use the following values. In the theoretical papers by Dsouza and Nott (2020) and Krishnaraj and Nott (2016), $K = 1.65$, $l = 10 d_p$, $\mu = 0.5$, $\mu_w = 0.33\mu$. In our simulation, $d_p = 0.00083$ m, $\Delta\phi = 0.05$ which is fit by the variation of ϕ from wall to the center of the box, $\rho_p = 2500$ kg m^{-3}, $g = 9.8$ m s^{-2}, $d_1 = 0.3\ d_p^{-1}$, and $p_c = 0.7 \times 17 \rho_p g d_p$ which is

around the pressure at the height 17 particle diameters under the top surface. The coefficient 0.7 is matched by the pressure at the height in the simulation.

In figure 5.1, we show the variation of u_z/u_w as a function of y for $p_c = 0.7\times17\rho_p g d_p$ and $p_c = 0.7 \times 34\rho_p g d_p$ for the model. The vertical velocity u_z is proportional to p_c^{-1}, which is not similar to what we see in the simulations.

Incorporating the second term in equation (5.22) allows us to obtain an analytical solution for u_z. The general form of the solution is given by:

$$u_z(y) = u_z(\infty) + C_1 e^{-\xi y} + A e^{-(\xi+d_1)y} + C_2 e^{-y/l}, \tag{5.32}$$

where the coefficients are defined as follows:

$$C_1 = \frac{u_z(0) + l\frac{du_z}{dy}(0) + A(l(\xi + d_1) - 1)}{1 - (1 - \mu_w/\mu)^{1/2}}, \tag{5.33}$$

$$C_2 = -\frac{u_z(0)(1 - \mu_w/\mu)^{1/2} + l\frac{du_z}{dy}(0) + d_1 l A}{1 - (1 - \mu_w/\mu)^{1/2}}, \tag{5.34}$$

$$\text{and} \quad A = \frac{-\rho g \Delta\phi}{2p_c d_1(1 + K d_p \xi)(1 + d_1/\xi)(\mu_w + (\mu_w - \mu)(2d_1/\xi + d_1^2/\xi^2))}. \tag{5.35}$$

where $u_z(\infty)$, $u_z(0)$ are the vertical velocity at infinity and at wall. $\frac{du_z}{dy}(0)$ is its gradient at wall. The boundary conditions are determined by setting both the vertical velocity u_z and its derivative $\frac{du_z}{dy}$ at the shearing wall and at infinity. As y goes to infinity, we set both to zero. For $y = 0$, we set $u_z(0) = -0.03u_w$, $\frac{du_z(0)}{dy} = -0.9u_z(0)/d_p$, which is similar to what we found in our finite box simulation at the shearing wall. Using these boundary conditions to integrate equation (5.19), we found the vertical velocity u_z changes direction when y increases as shown in figure 5.2 as we set $l = 10d_p$. This result is not physical. If we set $l = 1d_p$, the vertical velocity u_z is negative, which means that the flow will be downward for all y as shown in figure 5.3. If we keep $l = 10d_p$ and set the derivative of vertical velocity smaller at the shearing wall $\frac{du_z(0)}{dy} = -0.1u_z(0)/d_p$, the vertical velocity u_z remains negative for all y as shown in figure 5.4, but the shearing zone for u_z is

much wider than we found in our finite box simulation as shown in 5.5. In fact, u_z is negative for all y when $\frac{du_z(0)}{dy} + \xi u(0) = \frac{du_z(0)}{dy} + (1 - \mu_w/\mu)^{1/2} u(0)/l > 0$.

Several reasons cause the mismatch between the simulation and the model. We assume the width and the height are infinite in our model, and there is no lower boundary to the box. As a result, there is no upward flow in the model. In the simulation, the particles flow upward since the box has a bottom wall. The shearing zone for vertical velocity is wider in the model than in the simulation since the width is infinite.

In figure 5.6, we compare the theoretical models for the case that the non-local term is included with different values of vertical velocity, the slope of vertical velocity at the shearing wall, and different values of the non-local length. For $l = 10d_p$ (red and green line), the vertical velocity changes direction when y is larger than $3d_p$ if we fit the velocity and its slope at the shearing wall (green line). This is non-physical as we consider an infinite box in the model. For $l = 1d_p$ (purple line), the vertical velocity keeps the same direction no matter how y increases and fits the simulation better near the shearing wall. On the other hand, the variation of velocity is tiny when we consider different values of p_c in the model including the non-local term.

In our simplified model, which neglects the non-local terms, the downward velocity is scaled by the velocity of the critical pressure with a decay rate of $d_1 + \xi$. This rate includes d_1, which represents the decay rate of volume fraction from the shearing wall, and ξ, which is the ratio of friction coefficients between the wall and the material. This solution (5.31) does not match the data observed in our simulations, where the downward velocity is not scaled by the pressure. When the non-local term is considered, as shown in equation (5.32), the model fits better with the decay profile of the vertical velocity.

Our model shows that the decay profile of the downward velocity is correlated with the non-local length l. However, additional conditions are necessary to determine the velocity at the wall.

The stress σ_{yz} for $l = 10d_p$, $V_z(0)/V_w = -0.07$, $\frac{dV_z(0)}{dy} = -0.6V_z(0)/d_p$ as shown

in figure 5.7 is negative near the shearing wall, which is not physical as what we observed in the simulation as shown in figure 5.9. Using the stress σ_{yz} for the other two parameter settings as shown in figure 5.8, the stresses are positive and the order of magnitude matches the simulation.

References

Dsouza, Peter Varun and Prabhu R Nott (Apr. 2020). "A non-local constitutive model for slow granular flow that incorporates dilatancy". In: *J. Fluid Mech.* 888.

Krishnaraj, K P and Prabhu R Nott (Feb. 2016). "A dilation-driven vortex flow in sheared granular materials explains a rheometric anomaly". en. In: *Nat. Commun.* 7, p. 10630.

Rao, K K, P R Nott, and S Sundaresan (2008). "An introduction to granular flow". In:

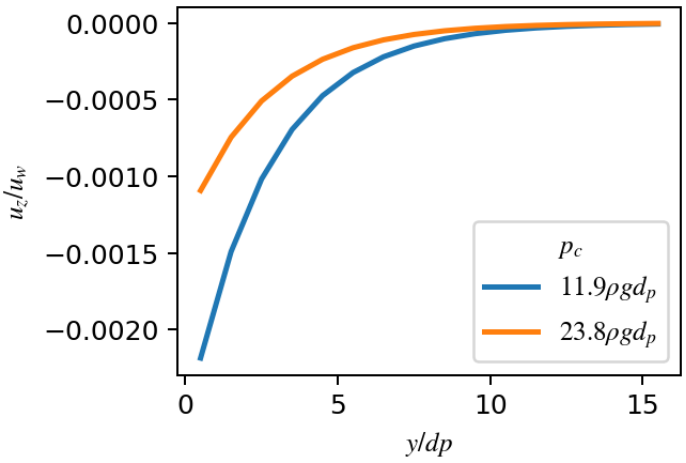

Figure 5.1: Vertical velocity u_z for two different values of p_c.

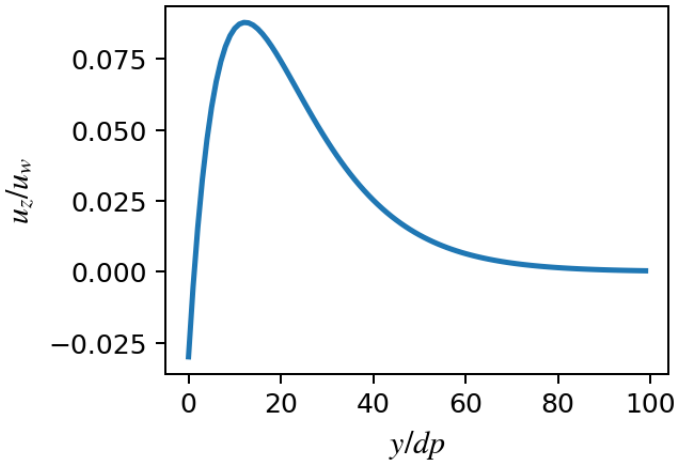

Figure 5.2: Vertical velocity u_z as the term $l^2\Pi\partial_{yyy}u_x$ is included for $l = 10d_p$ and $p_c = 0.7 \times 17\rho_p g d_p$

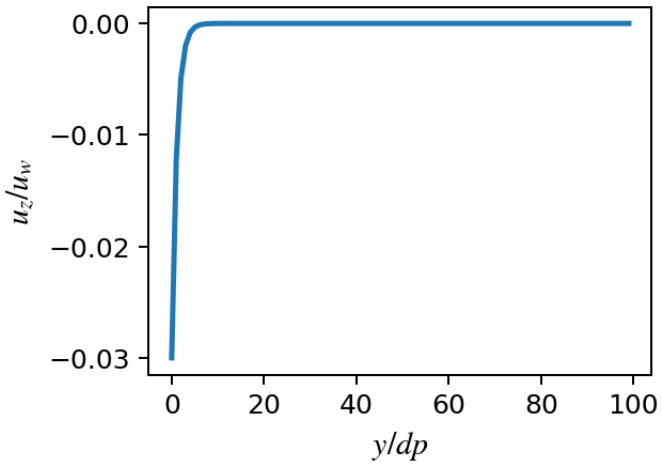

Figure 5.3: Vertical velocity u_z as the term $l^2\Pi\partial_{yyy}u_x$ is included for $l = 1d_p$ and $p_c = 0.7 \times 17\rho_p g d_p$

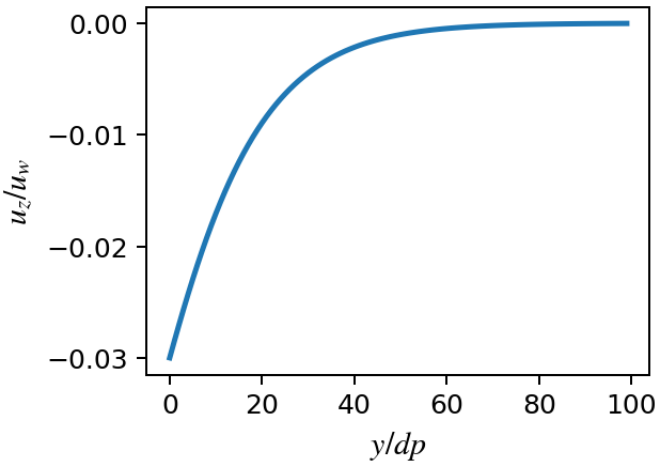

Figure 5.4: Vertical velocity u_z as the term $l^2\Pi\partial_{yyy}u_x$ is included for $l = 10d_p$, $\frac{du_z(0)}{dy} = -0.1u_z(0)/d_p$ and $p_c = 0.7 \times 17\rho_p g d_p$

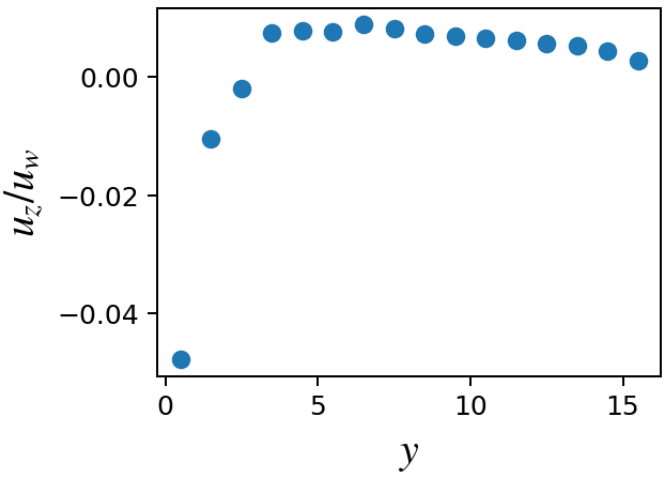

Figure 5.5: Vertical velocity in simulation for box size $50d_p \times 16d_p \times 120d_p$.

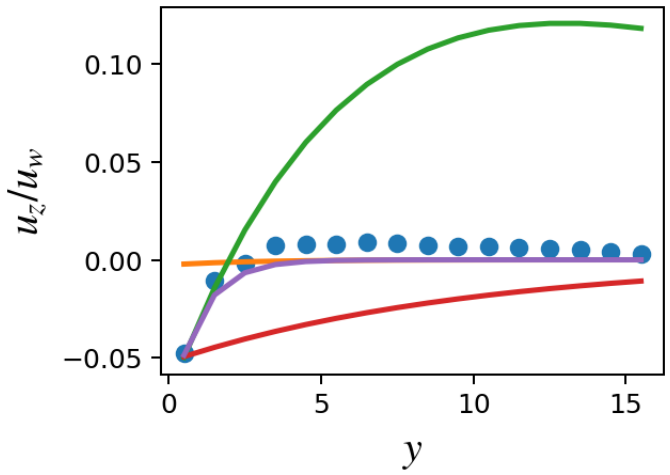

Figure 5.6: The dots comes from simulation for box size $50d_p \times 16d_p \times 120d_p$ at the height $17d_p$ under its surface. The orange line is the model ignoring the non-local term. The red, purple, and green lines come from the model including the non-local term with the same vertical velocity $V_z(0)/V_w = -0.07$ on the shearing wall but different non-local length l and gradient of velocity on the shearing wall. For the green line we set $l = 10d_p$, $V_z(0)/V_w = -0.07$, $\frac{dV_z(0)}{dy} = -0.6V_z(0)/d_p$. For the red line we set $l = 10d_p$, $V_z(0)/V_w = -0.052$, $\frac{dV_z(0)}{dy} = -0.1V_z(0)/d_p$. For the purple line we set $l = 1d_p$, $V_z(0)/V_w = -0.08$, $\frac{dV_z(0)}{dy} = -0.99V_z(0)/d_p$.

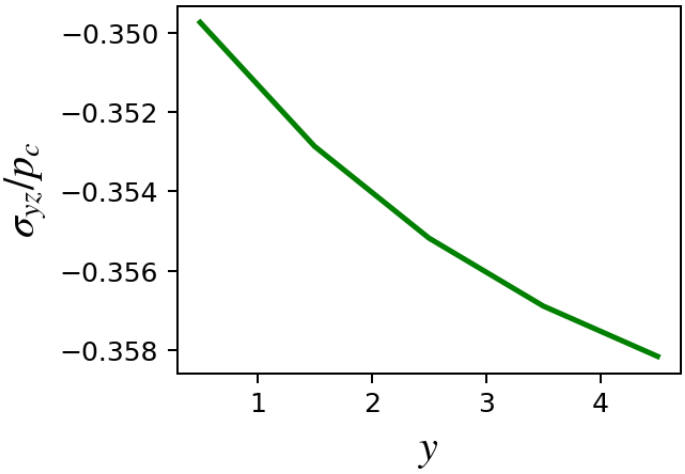

Figure 5.7: Profile of the stress σ_{yz}. We set $l = 10d_p$, $V_z(0)/V_w = -0.07$, $\frac{dV_z(0)}{dy} = -0.6V_z(0)/d_p$. The direction of σ_{yz} is different as in the simulation and its order of magnitude is much larger.

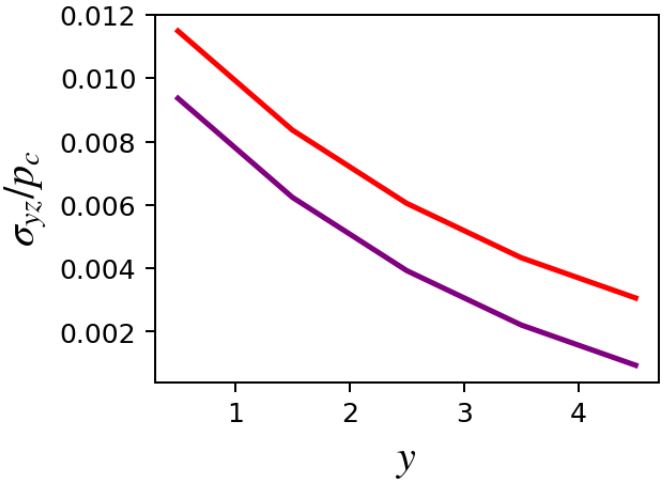

Figure 5.8: Profiles of the stress σ_{yz}. We set $l = 10d_p$, $V_z(0)/V_w = -0.052$, $\frac{dV_z(0)}{dy} = -0.1V_z(0)/d_p$ (red line) and $l = 1d_p$, $V_z(0)/V_w = -0.08$, $\frac{dV_z(0)}{dy} = -0.99V_z(0)/d_p$ (purple line). The direction of σ_{yz} and its order of magnitude are the same as in the simulation.

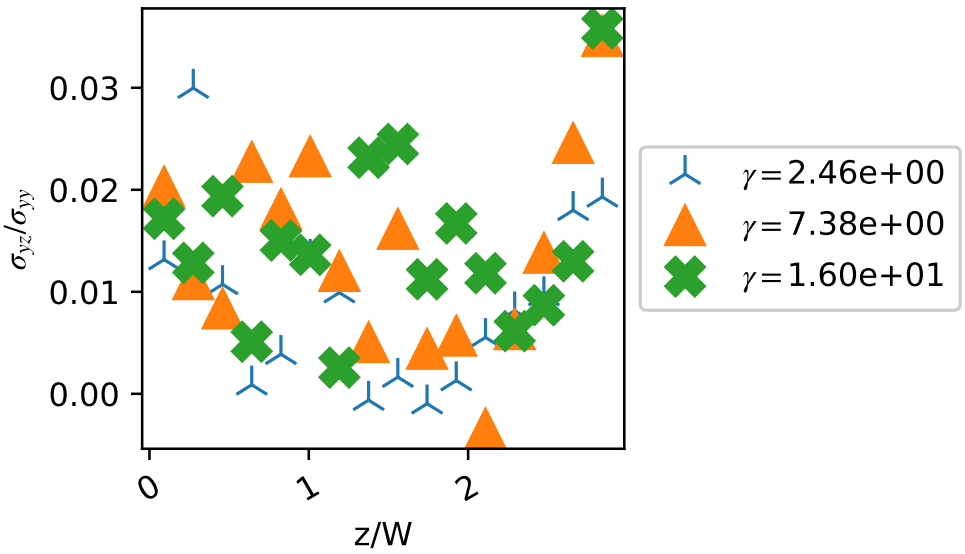

Figure 5.9: Wall stress ratio σ_{yy}/σ_{yz} for the shearing wall in the simulation ($H = 60d_p$).

Chapter 6

CONCLUSION AND FUTURE OUTLOOK

6.1 Conclusion

Our research has shown that the normal stress and shear stress on the shearing wall increase after the initiation of shearing, as observed in both experiments and simulations. The steady values for these stresses are independent of the shearing speed within a certain range in both simulation and experiment. The strain required for the wall stress to reach a steady state is found to be of the same order of magnitude for different wall speeds in the experiments when the speed is low, while in the simulations the strain to the steady state is not completely independent of the shearing speed. Our simulations have also revealed that the height of particles near the shearing wall decreases gradually, with the presence of vortex flow in both simulation and experiment, and the shear rate near the moving wall is high initially and decreases slowly to reach the steady state. Additionally, our simulation results showed an exponential decay in velocity toward the wall on the top surface as shown in figure 4.8, while experiments showed a constant velocity as shown in figure 2.15. This discrepancy may be due to PIV's screening area being far away from the shearing cylinder's wall.

Additionally, we have developed a method for predicting the downward flow near the shearing surface and the decay profile of velocity in an infinitely wide box under steady-state conditions, utilizing the non-local equations proposed by Dsouza and Nott (2020). Our model employs the Boussinesq approximation, where density variations are significant only in the body force term. The resulting decay profile of velocity and the direction of vertical velocity are in agreement with observations from our simulations. Furthermore, the predicted ratio of vertical shear stress to normal stress on the shearing wall in our model is approximately 10^{-2}, which is consistent with the order of magnitude observed in the simulations. Previously there is no model that calculates vertical wall stress correctly. Our model predicts the vertical stress ratio on the moving wall depends on the non-local length, velocity profile, and the variation of volume fraction from the shearing wall. Our model assumes an infinitely large box, lacking a bottom, and thus fails to predict the upward flow observed in experiments and simulations of a finite container that is

positioned away from the shearing wall. To improve the model and make it more accurate, we need to further study the transient behavior and finite box size, which will require solving the PDEs of non-local equations numerically.

Our simulations and experiments indicate that the system is in the quasistatic regime, as the inertial number (which is also the square root of the Savage number) is below 10^{-3} even near the shearing wall. In the Couette cell experiments, the average inertial number is also less than 10^{-3}, although the instantaneous inertial number may be large near the rotating cylinder at the start of the experiment.

In our experiments, it needs 20 revolutions to get to the steady state when shearing with the rough cylinder. While it needs 80 revolutions with the smooth cylinder. The corresponding strains are calculated by $\gamma = 2\theta/(1 - r_i^2/r_o^2)$, where θ is the rotational angle. Hence the strain to steady state is $\gamma \approx 320$ for the rough and $\gamma \approx 1280$ for the smooth cylinder. In our simulations, the changes in velocity and wall stress become slow before the strain exceeds 10^2.

6.2 Compare to other models

Our research highlights the role of dilatancy in causing secondary flow over a large area from the shearing wall to its periphery. Previous models have been able to predict deformation in regions where the yield condition is not satisfied, but they all assume granular media to be incompressible, ignoring the variation of volume fraction (Srinivasa Mohan, Kesava Rao, and Nott, 2002; Pouliquen and Forterre, 2009; Bouzid et al., 2013; Henann and Kamrin, 2013). Our model extends the critical state theory to account for non-local behavior, allowing for a variation of volume fraction with pressure. By incorporating this variation from the shearing wall to the far periphery, we are able to accurately predict both the secondary flow and vertical stress on the wall.

6.3 Future direction

The model assumes the critical pressure function Π and the non-local length l are both independent of the inertial number. To make the model applicable in the

inertial regime, the dependence of the inertial number must be taken into account. Measuring shear rates beneath particle surfaces is still difficult. An effective solution is to utilize the magnetic resonance imaging (MRI) method proposed by Penn et al. (2017), which can measure internal granular velocity, to address this challenge.

References

Bouzid, Mehdi et al. (Dec. 2013). "Nonlocal rheology of granular flows across yield conditions". en. In: *Phys. Rev. Lett.* 111.23, p. 238301.

Dsouza, Peter Varun and Prabhu R Nott (Apr. 2020). "A non-local constitutive model for slow granular flow that incorporates dilatancy". In: *J. Fluid Mech.* 888.

Henann, David L and Ken Kamrin (Apr. 2013). "A predictive, size-dependent continuum model for dense granular flows". en. In: *Proc. Natl. Acad. Sci. U. S. A.* 110.17, pp. 6730–6735.

Penn, Alexander et al. (2017). "Real-time probing of granular dynamics with magnetic resonance". In: *Science Advances* 3.9, e1701879.

Pouliquen, Olivier and Yoel Forterre (Dec. 2009). "A non-local rheology for dense granular flows". en. In: *Philos. Trans. A Math. Phys. Eng. Sci.* 367.1909, pp. 5091–5107.

Srinivasa Mohan, L, K Kesava Rao, and Prabhu R Nott (Apr. 2002). "A frictional Cosserat model for the slow shearing of granular materials". In: *J. Fluid Mech.* 457, pp. 377–409.